

The Tectonic Character of Mercury

PAUL K. BYRNE, CHRISTIAN KLIMCZAK, AND A. M. CELÂL ŞENGÖR

10.1 INTRODUCTION

From its three flybys in 1974–1975, Mariner 10 told us that Mercury is a tectonic world. That is, the planet has experienced a long and complicated history of tectonic deformation, recorded by its preserved landforms. As the study of tectonics naturally intersects with volcanology, chemistry, interior structure, and thermal evolution, understanding the tectonic character of a world – the nature, distribution, and formation histories of its tectonic landforms, and their spatial and temporal relationship to the interior – is a crucial means by which to comprehend more fully the geological history of that body.

In this chapter, then, we seek to tie together the various strands of observational and analytical studies of Mercury’s tectonic character conducted since the first Mercury flyby of the MESSENGER mission. First, we introduce Mercury’s tectonics as understood after the Mariner 10 flybys, and we outline some of the outstanding questions raised by that mission, indeed questions that helped frame the MESSENGER project. In Section 10.2, we begin to discuss Mercury’s tectonic character – the types and distributions of the most widespread record of Mercury’s tectonic deformation: its population of shortening structures. In the subsequent section, we discuss the planet’s spatially limited but important set of extensional structures. In Section 10.4, we briefly review a set of systematic long-wavelength modifications to Mercury’s topography that remain unexplained but that may have been tectonically driven. In Section 10.5, we discuss the extent of our understanding of the structure and mechanical behavior of Mercury’s lithosphere – the mechanically strong outer layer of the planet (Chapter 3). The mechanisms for tectonic deformation, chief among them global contraction but also those that appear to operate solely within volcanically flooded impact features, are then discussed in Section 10.6. Other mechanisms known to drive tectonic activity are briefly visited in Section 10.7.

In Section 10.8, we explore the other major aspect of Mercury’s tectonics – *when* deformation took place – as we attempt to describe at least in broad terms the tectonic history of the planet. The influence that the planet’s tectonic properties and evolution have played on its volcanism is then addressed in Section 10.9. In the final section, we list some major questions regarding Mercury’s tectonics that remain open, and suggest how they might yet be answered.

10.1.1 Observations of Tectonic Features by Mariner 10

Images returned by the Mariner 10 spacecraft of about ~45% of Mercury’s surface show a landscape battered by impact

bombardment, its terrains discriminated largely by the level of cratering. Notably, evidence of tectonic deformation was readily identified across the entire portion of the planet surface imaged by that spacecraft (Murray et al., 1974; Strom et al., 1975).

The greatest degree of structural complexity was observed in Caloris Planitia, an expansive deposit of smooth plains interpreted to be volcanic and situated within the largest well-preserved impact basin on the planet, with an east–west diameter of some 1640 km (Byrne et al., 2013a; Chapter 9). Although little more than a third of the spatial extent of these plains was imaged, they were seen to include lineations and graben-like structures, interpreted to represent extensional strain, as well as a complex pattern of ridges regarded as evidence of crustal shortening (Murray et al., 1974; Strom et al., 1975). Vertical motion was proposed to account for both types of landform, with the graben and ridges within the Caloris basin attributed to uplift from isostatic readjustment and subsidence from volcanic loading, respectively (Strom et al., 1975; Dzurisin, 1978).

A large population of escarpments identified outside the Caloris basin were also inferred to be shortening structures (e.g., Strom et al., 1975). In fact, it was apparent from the outset that, for the entire portion of Mercury viewed by Mariner 10, by far the most widespread form of tectonic deformation accommodated horizontal shortening (e.g., Trask and Guest, 1975). Thrust-fault-related landforms are so abundant that Strom et al. (1975) concluded that their formation mechanism must be global in nature.

The style of crustal tectonics on a planet is intimately tied to the thermal evolution of the planetary interior (Solomon, 1977). The widespread occurrence of shortening structures therefore implies a thermal history characterized by global contraction, in which the planet’s interior cools through time and the body experiences a net reduction in volume (Solomon, 1978) (Section 10.6.1). Global contraction was invoked as a causal mechanism for those shortening structures observed across Mercury outside the smooth plains units (Murray et al., 1974; Strom et al., 1975). On the basis of their length, height (as a measure for vertical displacement), and a range of fault dip angles, Strom et al. (1975) calculated that the scarps observed over about 24% of Mercury’s surface, extrapolated to a global population of shortening structures, represent a reduction in planetary radius of 1–2 km.

This value is a key parameter for thermal evolution models of Mercury, which address, among other aspects, the bulk abundances of heat-producing elements in the planet’s silicate portion, the nature of mantle convection through time, and the

history of cooling and present-day structure of the planet's large metallic core, the source of its internal magnetic field (e.g., Hauck et al., 2004; Grott et al., 2011; Michel et al., 2013; Tosi et al., 2013, 2015; Chapters 4 and 19). Accordingly, much of the study of Mercury's tectonic evolution has focused on the extent to which the planet has contracted, as recorded by its assemblage of shortening structures. Following Strom et al. (1975), studies of planetary radius change from Mariner 10 photogeology consistently reported estimates of ~1–2 km (Watters et al., 1998, 2009a; Watters and Nimmo, 2010) – substantially less than the ~5–10 km predicted by interior thermal history models of the planet (e.g., Solomon, 1977; Schubert et al., 1988; Dombard and Hauck, 2008) (Section 10.6.1). This discrepancy between photogeological observation and model prediction persisted long after the Mariner 10 mission.

10.1.2 Post-Mariner 10 Questions

The findings from Mariner 10 raised far more questions than they answered, strongly whetting the scientific community's appetite for more Mercury science. Indeed, the gaps in our understanding of Mercury's geological history served to frame several of the driving science questions for the MESSENGER mission (Chapter 1). As they pertained to the innermost planet's tectonics, those questions called for a full characterization of the spatial and temporal distribution of tectonic landforms and a determination of their contribution to planetary radius change.

Specifically, did expressions of Mercury's tectonics occur as widely across the hemisphere not viewed by Mariner 10 as across the imaged hemisphere? Relatedly, was the tectonic deformation observed in the eastern portion of the Caloris basin floor representative of these plains as a whole? Aside from the interior of the Caloris basin, where else (if anywhere) was extension preserved on Mercury? When did the planet's tectonic landforms start to develop, when did they cease to be active, and what drove their formation? To what extent do the planet's shortening landforms reflect the effects of global contraction rather than some other process or processes? And by how much did Mercury *actually* contract as a result of secular interior cooling?

A key science objective of MESSENGER's primary mission was to study the geological history of Mercury (Chapter 1). That history encompasses geological, geochemical, and geophysical processes, of which tectonic deformation is an important part. Mercury's tectonics have not only helped shape the planet surface but have likely played a controlling role in its volcanic history (Section 10.9 and Chapter 11) – and have in turn been influenced at least in part by the planet's record of impact bombardment (Section 10.6.4 and Chapter 9). Numerous measurements of the planet's properties have given insight into its tectonics, including its shape, topography, crustal thickness, surface composition, and even its interior structure.

10.1.3 Mercury Tectonics with MESSENGER Data

Absent an ability to visit them in the field, the most effective means of assessing tectonic landforms is with remotely sensed photographic and topographic data. The Mariner 10 mission facilitated early studies of Mercury's tectonics by means of its

Television Photography Experiment (Murray et al., 1974). This instrument returned photographic images of tectonic landforms, from which their morphology and distribution could be determined (Trask and Guest, 1975). Topographic data were obtained from photoclinometry (Strom et al., 1975) and, in some cases, from stereophotogrammetry (Spudis and Guest, 1988).

The MESSENGER spacecraft carried a far more capable instrument payload (Solomon et al., 2008; Chapter 1) and returned global coverage of Mercury's surface at resolutions far higher than those of Mariner 10 data. Many MESSENGer-based tectonic studies have used the global mosaic base maps derived from the Mercury Dual Imaging System (MDIS) (Hawkins et al., 2007). Consisting of image data from the wide- and narrow-angle cameras (WAC and NAC, respectively), and featuring mean resolutions of 250 m/pixel, several global base maps with a variety of solar incidence and illumination azimuths were produced (Chabot et al., 2016), facilitating regional to global tectonic surveys (e.g., Rothery and Massironi, 2010; Di Achille et al., 2012; Byrne et al., 2014). More detailed structural analyses can be accomplished with thousands of high-resolution MDIS NAC images (both targeted and opportunistically acquired), which have typical resolutions of tens of meters per pixel trending to meters per pixel for those acquired toward the end of MESSENGER's low-altitude campaign (Chapter 1).

Although it did not carry a dedicated stereo imaging system, repeated passes by MESSENGER over the surface enabled the production of digital elevation models (DEMs) with stereophotogrammetric techniques. Elevation data for substantial portions of Mercury were calculated at resolutions at or below ~1 km/pixel (e.g., Oberst et al., 2010; Preusker et al., 2011), and DEMs have been created for selected regions at higher resolutions (e.g., Fassett and Crowley, 2016). A global DEM, at a resolution of 665 m/pixel, was also generated from the control network derived from the development of the global image base maps (Becker et al., 2016). Notably, topographic measurements of Mercury's northern hemisphere were also acquired by MESSENGER's Mercury Laser Altimeter (Cavanaugh et al., 2007; Zuber et al., 2012); individual laser altimetric profiles were then combined to form an interpolated DEM of the northern hemisphere, also at a resolution of 665 m/pixel. These regional and global elevation data products in particular have been of considerable use for thrust fault displacement-length scaling analyses (e.g., Byrne et al., 2014; Section 10.6.1), as well for characterizing the relationship between tectonics and topography (Section 10.2.1).

10.2 SHORTENING STRUCTURES ON MERCURY

Perhaps the most prominent product of Mercury's tectonic history is its population of landforms thought to have formed by brittle deformation. Like all planetary surfaces on which tectonic processes other than plate tectonics have acted, these landforms lend themselves to classification as either primarily shortening or lengthening (i.e., extensional) in nature. Consistent with Mariner 10 findings, MESSENGER

observations have shown that lithospheric shortening is the dominant form of tectonic deformation on Mercury and has occurred globally. In this section, we first review the types of shortening structures documented across Mercury, drawing comparisons where possible with cognate structures on Earth. Next, we review the spatial distributions of shortening structures on the innermost planet, before presenting a kinematic analysis of shortening-related deformation on Mercury, once more informed by centuries of exploration of tectonic deformation on our own planet.

10.2.1 Types of Shortening Structures

Throughout the literature regarding Mercury's shortening tectonics, terms such as "wrinkle ridge," "high-relief ridge," and "lobate scarp" have been commonly used (e.g., Strom et al., 1975; Dzurisin, 1978; Melosh and McKinnon, 1988; Watters et al., 1998, 2004, 2009a, 2015; Watters and Nimmo, 2010; Egea-González et al., 2012). [Indeed, Dzurisin (1978) developed a classification scheme consisting of at least six discrete categories into which positive-relief landforms were grouped.] On the basis of Mariner 10 data, Mercury's wrinkle ridges were observed to resemble those in the lunar maria – often manifest as broad, steep-sided but low-relief arches symmetric in cross section, variously with or without crenulated crests (Strom et al., 1975; Dzurisin, 1978); numerous examples appear flat-topped. Qualitatively, wrinkle ridges are shorter, narrower, and possess less relief than other types of shortening-related landforms. A characteristic property of wrinkle ridges is the substantial morphological variation along strike, with changes to width, height, and number of sides often observed (Figure 10.1a). As suggested by their name, high-relief ridges tend to possess greater relief than wrinkle ridges, but they were also noted to be generally symmetric in cross section (Watters et al., 2001). Although considerable along-strike changes in size and shape are less commonly seen for high-relief ridges, some variation in width and height occurs (Figure 10.1b). In contrast to the generally symmetrical cross sections of wrinkle- and high-relief ridges, Strom et al. (1975) described lobate scarps as highly asymmetric in transverse view, with steep slopes on one side and gentle backslopes on the other; in map view they have relatively steep and long escarpments that typically show a broadly lobate outline (Figure 10.1c). Some lobate scarps, such as Beagle Rupes, have strongly arcuate forms, however (Rothery and Massironi, 2010) (Figure 10.1d). Many examples show smaller, subordinate scarps along their leading edges; such accessory scarps are visible, for example, where the larger structures in Figures 10.1c and 10.1d cut through the smooth-floored Duccio and Sveinsdóttir craters, respectively.

Despite differences in morphology between these landform types, in all cases these features have been interpreted as being a manifestation of lithospheric shortening, representing some combination of thrust faulting and/or folding (e.g., Strom et al., 1975; Dzurisin, 1978; Melosh and McKinnon, 1988; Watters et al., 2004; Watters and Nimmo, 2010). Comparable assessments have been made of morphologically similar landforms on other worlds (e.g., Colton et al., 1972; Lucchitta, 1976; Schultz, 1985; Mueller and Golombek, 2004).

Tectonic deformational features on Earth tell us that lobate scarps, as upthrust volumes of rock, are likely the folded portions of hanging walls atop thrust faults (i.e., low-angle faults formed in compression) (Figure 10.2). With the nomenclature developed for tectonics on Earth, then, lobate scarps are fault-propagation- or fault-bend folds, which together may be classed as "fault displacement-gradient folds" (Wickham, 1995). On the basis of shape alone, lobate scarps are asymmetric hanging-wall anticlines or monoclines (arch- or step-like folds, respectively). This interpretation is consistent with observations of narrow graben along the crests of scarps on several worlds (Section 10.3), which likely reflect outer-arc (or extrados) extension along the fold hinge lines (Figure 10.2). Moreover, the East Kaibab monocline in southwestern Utah, United States, matches the geometry of exemplar lobate scarps on Mercury, Mars, and the Moon once its eroded volume is restored (Byrne et al., 2016a). The subordinate lobate scarps along the leading edges of larger counterparts (Strom et al., 1975) may be thrust duplexes – imbricate (overlapping) stacks of smaller fault-bound slices of upthrust rock regularly seen within shortening systems on Earth (e.g., Butler, 1982). The asymmetry of lobate scarps therefore reflects the vergence of the hanging-wall anticlinal fold: the landform can be said to "verge" in the direction the steeper scarp faces – the direction the fold is inclined – which in turn indicates the direction of tectonic transport of the hanging-wall block along the underlying fault (e.g., Byrne et al., 2014) (Figure 10.2).

Landforms proposed as analogs to wrinkle ridges have been described at numerous sites on Earth, including Algeria, Australia, the Solomon Islands, and the United States (e.g., Plescia and Golombek, 1986; Petterson et al., 1997; Last et al., 2012), and in each case they feature the folding of rocks over thrust faults. Although several wrinkle ridge properties, including the orientation and depth of the causative faults and the kinematics of fault-related folding, remain to be fully characterized (e.g., Watters, 1991; Golombek et al., 1991; Plescia, 1991, 1993; Schultz and Tanaka, 1994; Zuber, 1995; Schultz, 2000; Mueller and Golombek, 2004), these landforms have also been considered as forms of fault displacement-gradient folds (Plescia and Golombek, 1986). The steep escarpments that bound wrinkle ridges can themselves be regarded as monoclines (albeit at scales smaller than those characterizing lobate scarps) such that where they occur, two opposite-facing ridge-bounding scarps are essentially paired monoclines, similar to those observed in the Southern Rocky Mountains, United States (Tweto, 1975), Libya (Fodor et al., 2005), and the United Kingdom (Woodcock and Soper, 2006). Accordingly, where wrinkle ridges have steep sides, they, too, can be said to have vergence.

To our knowledge, no examples on Earth of high-relief ridges have yet been documented. This may not be a function of geology, however, but rather may reflect a limitation in the use of morphology as a discriminator for landform classification. High-relief ridges have been suggested to differ from lobate scarps only in that the dip angle of their underlying fault is greater than that of a lobate scarp fault (Watters and Nimmo, 2010), and so these landforms may occupy two points on a single morphological continuum. Under that interpretation, a high-relief ridge is simply a hanging-wall anticline over a

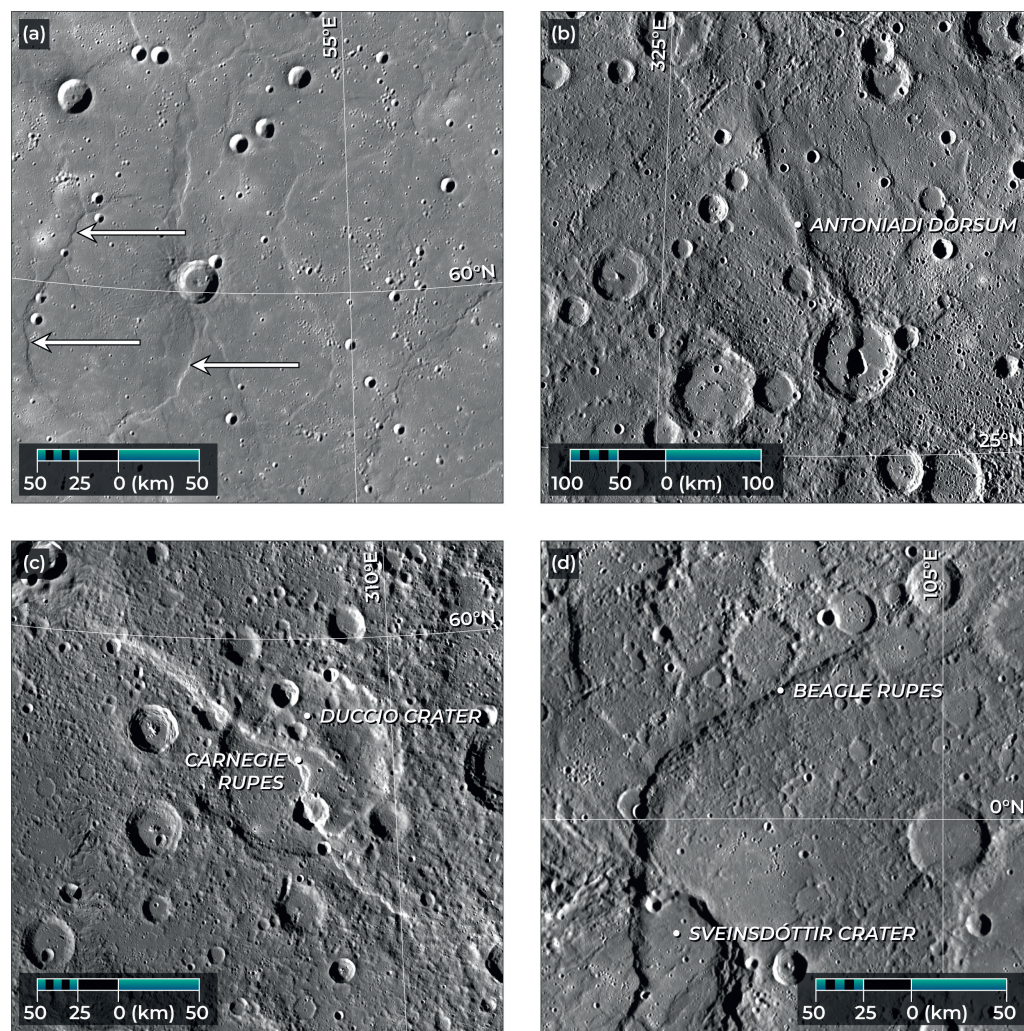


Figure 10.1. Examples of shortening landforms on Mercury. (a) Smooth plains structures in Mercury’s northern plains (the majority of which are “wrinkle ridges”). Note the localization of shortening landforms at the rims of buried craters (shown by white arrows). (b) Antoniadi Dorsum, one of the comparatively rare class of tectonic landform historically termed a “high-relief ridge”; this example is 360 km in length. (c) Carnegie Rupes, an example of a relatively linear monocline (a “lobate scarp”); this feature, almost 270 km long, cuts through the Duccio crater (133 km in diameter). (d) Another monocline, Beagle Rupes, noted for its pronounced arcuate shape in map view. About half of the 630-km-long scarp is shown. Azimuthal equidistant projections, centered as follows: (a) 60.3°N, 52.9°E; (b) 29.0°N, 329.5°E; (c) 58.5°N, 306.7°E; and (d) 2.0°S, 103.0 °E. These and all subsequent images in this chapter are taken from the global morphology base map (Chabot et al., 2016).

relatively steep reverse fault, with the symmetry of the fold precluding a definitive identification of vergence and thus the associated fault’s slip direction.

Despite the published work comparing extraterrestrial shortening landforms with those on Earth, however, the terms lobate scarp, high-relief ridge, and wrinkle ridge – which are *never* used for terran tectonics – persist in the planetary tectonic literature and render it opaque. Yet the variations in shape of these landforms on Mercury is such that these terms of classification fail us in many cases. For example, although lobate scarps can generally be described as having a single steep escarpment with wrinkle ridges possessing two scarp-like sides (Figures 10.1c and 10.1d), this description does not always hold. The portion of Enterprise Rupes located outside the Rembrandt basin (Watters et al., 2009b) and one of Mercury’s largest systems of lobate scarps, has both a front- and a

backscarp, and in that respect resembles an enormous wrinkle ridge. Conversely, many wrinkle ridges on Mercury display only a single scarp, whereas others change along their length from single- to double-sided. These morphological distinctions are further challenged in cases where one landform type transitions into another. Lobate scarps can change to high-relief ridges along strike, for instance, a phenomenon illustrated in Figure 10.1b. As noted above, this change may simply reflect a variation in dip angle of the underlying fault (e.g., Watters and Nimmo, 2010). Additionally, several shortening structures terminate as lobate scarps at the western margin of the Caloris basin, continuing along the same strike as wrinkle ridges within those plains. A similar situation is observed on the Moon, where a lobate scarp transitions to a wrinkle ridge at the northern boundary between Mare Serenitatis and the surrounding lunar highlands (Masursky et al., 1978).

Table 10.1. The number and cumulative length of shortening structures by class on Mercury (after Byrne et al., 2014).

Structure class		% of Number of structures	% of total number	Cumulative length (m)	% of total length
Smooth plains	3751	63.2	2.07×10^8	49.8	
Cratered plains	1831	30.9	1.64×10^8	39.5	
Crater-related	252	4.2	2.01×10^7	4.8	
High-terrain-bounding	100	1.7	2.45×10^7	5.9	
Total	5934	100.0	4.16×10^8	100.0	

Therefore, a classification scheme for shortening structures based on morphology, such as that used historically for Mercury, works only in a general way but cannot capture the broad variation in geometry of these landforms. Geological setting, however, provides a clear and objective means by which to describe Mercury's shortening structures (Byrne et al., 2014) and is the basis on which we present those structures in this chapter (see Figure 10.3a). With this approach, shortening structures are classified by the primary terrain type in which they occur: "smooth plains" (Denevi et al., 2013) or "cratered plains," a term we use here that encompasses both the intercrater plains and heavily cratered terrain units described from Mariner 10 images (Trask and Guest, 1975; Chapter 6). Most such mapped landforms are therefore categorized here as "smooth plains structures" or "cratered plains structures." The remaining landforms are either spatially associated with impact craters and so are termed "crater-related structures" or border broad areas of substantially elevated terrain and are catalogued as "high-terrain-bounding structures." Topographic data, such as the DEM derived by Becker et al. (2016) shown in Figure 10.3b, provide the basis for this last classification. Several statistical measures for these structures, including number and cumulative length as fractions of the entire population of shortening landforms on Mercury, are given in Table 10.1.

Smooth plains structures (light blue lines in Figure 10.3a) are those hosted within Mercury's eponymous plains units. Smooth plains on the innermost planet are sparsely cratered relative to other terrain, are gently rolling to essentially level, and generally have clear boundaries (Trask and Guest, 1975). They occupy some 27% of Mercury's surface and occur at all longitudes, nearly all latitudes, and primarily low elevations (Denevi et al., 2013; Chapter 6). At least two-thirds of these deposits are interpreted as volcanic (Denevi et al., 2013; Chapter 11). The majority of thrust-fault-related landforms within smooth plains would traditionally have been classified as wrinkle ridges, but this class also includes some monoclines and asymmetric hanging-wall anticlines (i.e., lobate scarps) (Byrne et al., 2014). Smooth plains structures represent ~63% of all mapped structures but only ~50% of cumulative structure length (Table 10.1). Over 1500 structures (~40% of this population) are located in the vast Borealis Planitia, the "northern smooth plains" (NSP) of Head et al. (2011); the remaining structures are situated within

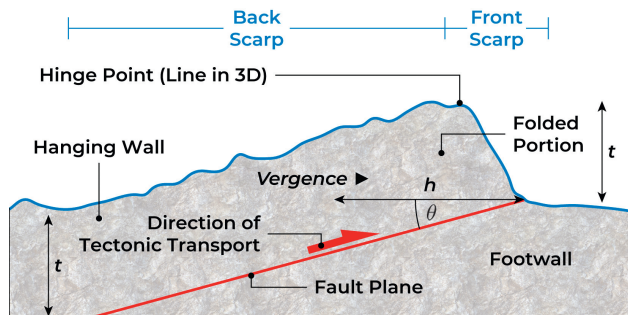


Figure 10.2. A schematic cross section of a lobate scarp, a type of thrust-fault-related landform. A thrust fault (red line) separates the upthrust volume of rock (i.e., the hanging wall) from the volume of rock that does not move (i.e., the footwall). The upper portion of the hanging wall is likely an asymmetric fold, which constitutes the lobate scarp itself. The direction that the steeper front scarp faces is the direction of vergence of the fold, which in turn gives the direction of tectonic transport of the hanging wall (red arrow). The hinge point is located at the crest of the fold; the hinge line extends perpendicular to the plane of view. When making estimates of horizontal shortening accommodated by such a structure, we assume that the heave, h , of the thrust fault is related to its throw, t , by the fault dip angle, θ (Section 10.6.1).

the extensive plains encircling the Caloris basin or in impact-feature-hosted smooth plains within more heavily cratered terrain (Denevi et al., 2013).

Cratered plains structures include those located in both the intercrater plains and heavily cratered terrain units described from images returned by the Mariner 10 spacecraft (Strom et al., 1975; Trask and Guest, 1975) (purple lines in Figure 10.3a). These units are older than the smooth plains and may have formed through voluminous volcanism during or at the end of the late heavy bombardment (LHB) of the solar system (Chapters 9 and 11), though at least some portion may have been emplaced as basin ejecta (Chapter 9). Excluding those landforms within isolated pockets of impact-related smooth plains, shortening structures in intercrater and heavily cratered plains are almost exclusively monoclines and asymmetric anticlines (Byrne et al., 2014). They constitute ~31% of all mapped structures and ~40% of cumulative structure length (Table 10.1).

Byrne et al. (2014) identified 252 arcuate or near-circular basin- and crater-related structures (teal lines in Figure 10.3a), which demarcate volcanically filled or buried impact features (typically marking the presence of a "ghost crater": Section 10.6.4). Although most structures of this class occur within smooth plains, with 62% in the NSP alone, a subset consists of large monoclines within impact basins that follow, and verge toward, the basin perimeter (e.g., Fegan et al., 2017). Indeed, the longest single structure mapped by Byrne et al. (2014) defines part of the third-largest impact feature recognized on Mercury to date, the 950-km-diameter Matisse–Repin basin (Spudis and Guest, 1988). In its entirety this structure class represents ~4% and ~5% of all surveyed shortening landforms and of cumulative structure length, respectively (Table 10.1).

The fourth structure classification described by Byrne et al. (2014) consists of high-terrain-bounding structures, a category that includes 100 monoclines and asymmetric anticlines that,

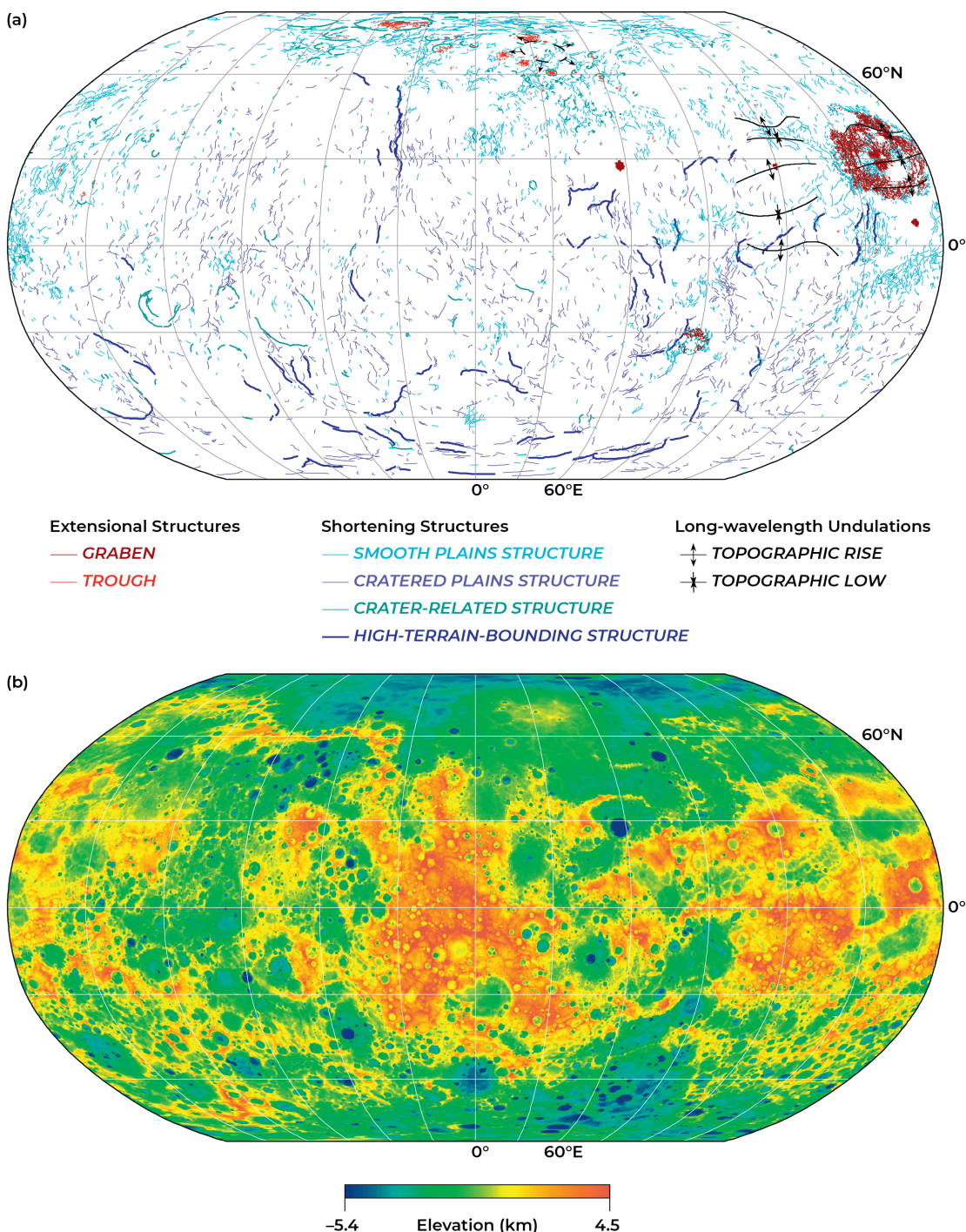


Figure 10.3. The shortening and extensional tectonic landforms of Mercury. (a) Shortening structures are shown in cool colors; extensional landforms are shown in warm colors. Long-wavelength topographic undulations within and proximal to the Caloris basin, as well as in the NSP, are shown with black lines; arrows denote downslope directions. The global population of shortening structures is from Byrne et al. (2014); extensional and shortening landforms in Rembrandt basin are from Ferrari et al. (2015). The troughs mapped in the NSP and the circum-Caloris plains are from Klimczak et al. (2012). (b) The global topography of Mercury, derived from a digital elevation model (Becker et al., 2016). Both maps are in a Robinson projection centered at 0°E; the graticule is in 30° increments in latitude and longitude.

individually or as systems of structures, lie along the margins of and thus partially delineate some portions of high-standing terrain (thick dark blue lines in Figure 10.3a). These landforms have a dominant sense of vergence toward adjacent lows and possess some of the greatest structural relief recorded on

Mercury. For example, parts of Enterprise Rupes rise 3 km above the surrounding plains. These thrust-fault-related landforms together represent ~2% of the total structure count but possess a disproportionately large ~6% of the total cumulative structure length (Table 10.1).

Importantly, there is no evidence for widespread strike-slip deformation on Mercury, as is observed at Earth's conservative plate margins and in escape tectonics settings on Earth and Venus. However, numerous shortening landforms show elements of strike-slip or oblique motion. For example, Rothery and Massironi (2010) investigated in detail the morphology of Beagle Rupes (Figure 10.1d) and interpreted the trapezoidal shape of this landform as a system composed of a frontal monocline and two lateral ramps showing evidence of transpression (i.e., combined orthogonal shortening and strike-slip deformation). (A ramp is a steep and usually short segment of a thrust fault as it climbs to a higher stratigraphic level.) Given the westward vergence of the frontal monocline, Rothery and Massironi (2010) inferred that the fault system must have accommodated oblique slip with right-lateral sense along the northern ramp and left-lateral sense along the southern ramp. These authors further concluded that, on the basis of its very prominent polygonal map pattern shape, the Beagle Rupes system is underlain by listric (curved) thrust faults that root to a basal décollement – a horizontal detachment surface – that extends several hundred kilometers to the east.

Other strike-slip kinematic indicators have been documented on Mercury. Massironi et al. (2015) identified oblique-shear kinematics along monoclines and anticlines in the form of lateral ramps, strike-slip duplexes, and restraining bends, as well as pop-up and pull-apart structures and en échelon (staggered or overlapping) folds. Oblique or lateral ramps associated with major thrust systems were reported, including at the distal ends of Enterprise Rupes, at the southern termination of Blossom Rupes, along Belgica Rupes, at the southern end of La Dauphine Rupes, and at the ends of Paramour Rupes (Galluzzi et al., 2015; Massironi et al., 2015). Additional examples of oblique fault slip were identified on the basis of changes in circularity and topography of faulted impact craters (Galluzzi et al., 2015). More such structures will likely be recognized on Mercury, as studies of the planet's thrust-fault-related landforms have so far focused predominantly only on the pure shortening they accommodate, with little detailed analysis of any components of oblique slip so often observed in intraplate

shortening systems on Earth (e.g., Cunningham et al., 1996; Norris and Cooper, 1997; Liu et al., 2012).

10.2.2 Distribution of Shortening Structures

A fundamental consequence of global contraction is a global stress field that is horizontally isotropic, which in the absence of other sources of stress or heterogeneities in lithospheric strength predicts a global, evenly distributed population of shortening structures with no preferred orientations (e.g., Solomon, 1977). Early observations of Mercury did not show evenly distributed thrust-fault-related landforms, but resurfacing by impact bombardment and volcanism, together with suboptimal illumination conditions and image resolution, hampered efforts to characterize fully the distribution of shortening structures across the hemisphere imaged by Mariner 10 (Strom et al., 1975).

Nonetheless, from Mariner 10 observations, Dzurisin (1978) identified a “tectonic grid” on Mercury, which was investigated further (Melosh and Dzurisin, 1978; Melosh and McKinnon, 1988; Thomas et al., 1988). This grid was attributed to the effects of tidal despinning of Mercury from an original rotation rate substantially higher than that of today (e.g., Melosh and McKinnon, 1988) (Sections 10.6.2 and 10.6.3). However, although mapping with MESSENGER data has shown that thrust faulting is not uniformly distributed on the planet – the NSP, for example, represent just ~6% of the planet's surface but host a disproportionately large number of shortening landforms – there is *no* definitive evidence of a globally coherent lithospheric fracture pattern that survived the LHB (Byrne et al., 2014), such as that predicted to have been influenced by tidal despinning.

Of note, shortening landforms appear concentrated along quasi-longitudinal bands at approximately 0°E, 90°E, 180°E, and 270°E. At these locations, the densities of mapped structures per $10^\circ \times 10^\circ$ bins are greatest (Figure 10.4). These longitudes, however, correspond to portions of the global photomosaic base maps from which the structure map in Figure 10.3a was produced that were obtained with the highest values of incidence angle, i , measured from the surface normal (Byrne et al., 2014). Such images, taken when the Sun was low in the

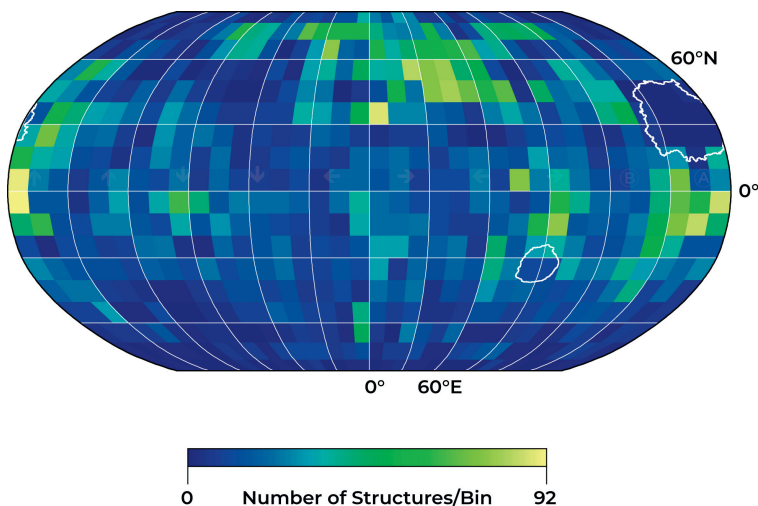


Figure 10.4. The spatial density of the shortening landforms shown in Figure 10.3a, color-coded by the number of discrete structures per $10^\circ \times 10^\circ$ bin. These data are adapted from Byrne et al. (2014) but exclude the structures inside the Caloris and Rembrandt impact basins (outlined in white). The map is in a Robinson projection centered at 0°E; the graticule is in 30° increments in latitude and longitude.

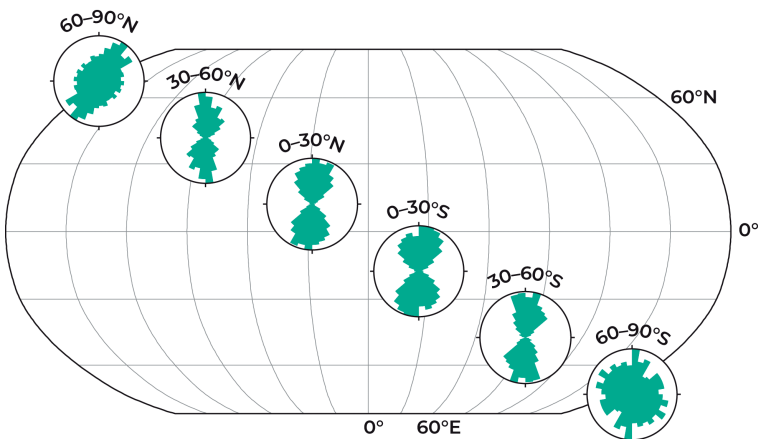


Figure 10.5. The distribution of shortening structures in Figure 10.3a, grouped into 30° latitudinal bands (with northern and southern hemisphere structures shown on the left and right, respectively). These data are adapted from Byrne et al. (2014) (and exclude structures in the Caloris and Rembrandt basins). The map is in a Robinson projection centered at 0°E; the graticule is in 30° increments in latitude and longitude.

sky, feature long shadows and so facilitate the ready identification and mapping of morphologically subtle tectonic landforms; regions imaged at lower incidence angles thus have fewer mapped structures.

Further, the orientations of structures between 60°N and 60°S show a predominance of north-south trends (Figure 10.5), consistent with the illumination of linear landforms from solar azimuth directions (measured clockwise) near ~90° and ~270° due to Mercury's very low obliquity (~2 arcmin). Structures north of 60°N, including a portion of the densely distributed landforms in the NSP, show some clustering at southwest-northeast trends but are not as strongly oriented as those at mid latitudes. South of 60°S, structures display no preferred orientation, but these latitudes host the lowest number of mapped shortening-related landforms per area (Figure 10.5).

Even the earliest workers studying Mercury noted a roughly north-south trend to tectonic structures on Mercury and suggested that lighting conditions might be at least in part responsible (Strom et al., 1975). The sensitivity to solar illumination of the identification of tectonic landforms was also noted by other workers (e.g., Melosh and McKinnon, 1988; Thomas et al., 1988). Although Byrne et al. (2014) demonstrated that shortening landforms visible in the image data are not uniformly distributed across Mercury, as was predicted for global contraction (e.g., Solomon, 1977) and by early models of tidal despinning (Melosh and McKinnon, 1988) (Section 10.6.3), the longitudinal bands of increased structure density shown in Figure 10.4 are likely a function principally of lighting geometry and not geology. The mapping of some basin-related structures is also likely influenced by an illumination bias (Fegan et al., 2017). Moreover, other processes are capable of producing a pattern of shortening strain that deviates from spatial homogeneity. Large impact basins act as zones of weakness in the lithosphere and concentrate shortening strains at their peripheries (e.g., Watters et al., 2001), leading to the class of landforms Byrne et al. (2014) termed crater-related structures (Section 10.2.1). Moreover, large basins and their extensive ejecta deposits are responsible for large areas devoid of thrust-fault-related landforms where illumination conditions are otherwise amenable to tectonic mapping, as is observed at the Vivaldi impact basin, in the planet's western hemisphere.

Yet there is evidence of systematic, regional-scale shortening on Mercury that may be geological in nature. In several places, groups of thrust-fault-related landforms form laterally contiguous, narrow bands of considerable length. One such system extends for some 1700 km (over 40° of arc) across Mercury's northern hemisphere and includes Victoria and Endeavour Rupes and Antoniadi Dorsum (Figure 10.6). Many of its constituent landforms are cratered plains structures, but those that comprise the northernmost third of this system border an area of high-standing terrain to the west and verge eastward onto the adjacent smooth plains. This sense of vergence is echoed by the other high-terrain-bounding structures along its length. An even longer system, 1800 km long, extends from 19°N, 55°E, to 23°S, 61°E, and also has a dominant westward vergence.

These systems have been recognized as fold-and-thrust belts (FTBs) (Byrne et al., 2014), counterparts to fold belts on Earth (e.g., Poblet and Lisle, 2011) and Venus (e.g., Burke et al., 1984). In their simplest terms, FTBs are linear, regionally contiguous sets of thrust faults with associated hanging-wall anticlines that have a single predominant sense of vergence. Many FTBs on Earth feature an extensive décollement at depth (McClay, 1992; Roeder, 2009). Such a structural arrangement may not commonly exist for Mercury's FTBs, but it has been inferred to underlie individual arcuate monoclines on the planet (e.g., Rothery and Massironi, 2010) (Section 10.2.1).

10.2.3 Kinematics of Shortening Structures

The contrast in morphology and density of tectonic structures hosted by Mercury's younger smooth plains and the older cratered plains (compare Figure 10.1a with Figures 10.1b–10.1d) could reflect differences in rheological and structural fabric characteristics between the two terrain types. For example, MESSENGER X-Ray Spectrometer (XRS) and Gamma-Ray Spectrometer (GRS) measurements of elemental abundances indicate that the surface composition of at least some heavily cratered terrain is more magnesian but less feldspathic than the low-iron basalt-like NSP (Weider et al., 2012; Chapter 7). With their internal structure rendered more complex by sustained impacts and volcanic resurfacing (e.g., Denevi et al., 2009; Ernst et al., 2010), the cratered plains material may thus have isotropic textures on the scale of tens to hundreds of kilometers

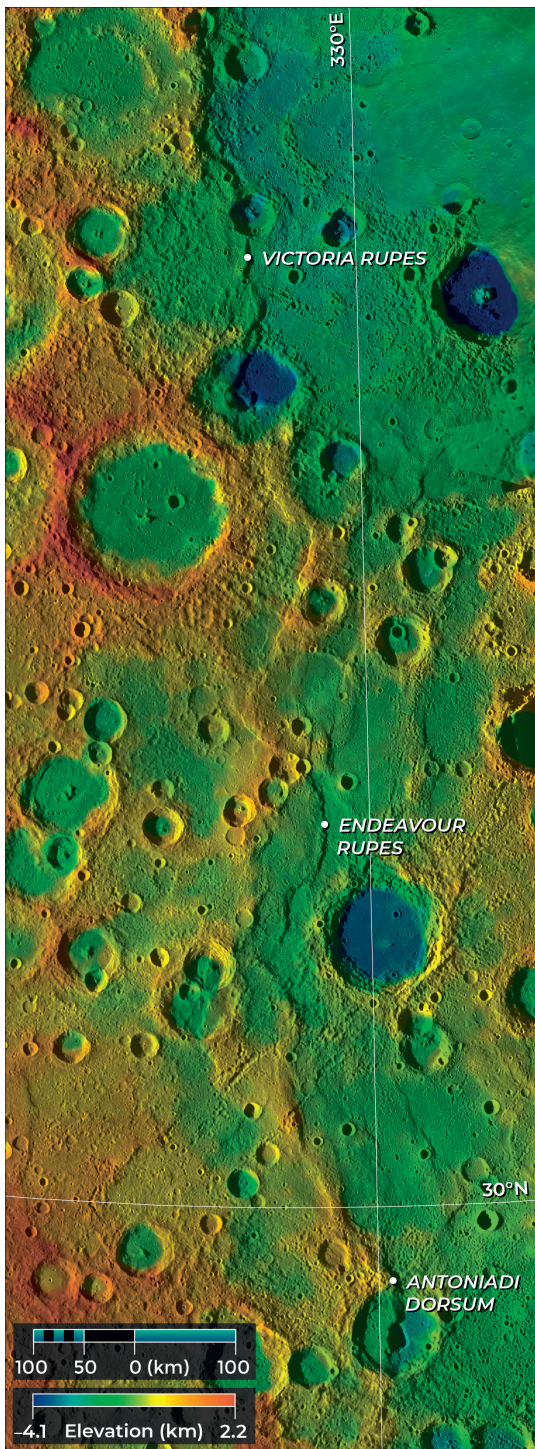


Figure 10.6. A fold-and-thrust belt on Mercury. This example is ~1700 km long and consists of an aligned assemblage of monoclines and asymmetric and symmetric anticlines. Named parts of this system include Victoria and Endeavour Rupes and Antoniadi Dorsum (Figure 10.1b). The colors correspond to elevation, derived here and in subsequent figures from the global DEM of Becker et al. (2016). Azimuthal equidistant projection, centered at 40.0°N, 328.0°E.

that facilitated the development of thick-skinned, large-scale fault and fold systems, which root to (bottom out at) depths of tens of kilometers (and possibly to deep basal décollements)

(Figure 10.7), consistent with the results of forward modeling studies of topographic profiles across several monoclines and anticlines (Watters et al., 1998).

In contrast, the smooth plains likely feature strong vertical variations in mechanical properties inherent to layered volcanic strata (e.g., Jerram and Widdowson, 2005; Section 11.4), which promote detachments and shallow tectonic deformation (Freed et al., 2012). Smooth plains structures occur consistently within stratified units on Mars and, although there is debate as to whether they are thick- or thin-skinned in nature (e.g., Watters, 1991; Zuber, 1995; Mangold et al., 1998; Schultz, 2000; Golombek et al., 2001; Montési and Zuber, 2003; Mueller and Golombek, 2004), fits of topographic profiles from elastic dislocation models to observed profiles indicate that the thrust faults beneath these landforms root to shallow crustal levels (Watters, 2004). Given the similarity in setting and morphology between smooth plains structures on Mars and Mercury, landforms on the latter body are probably thin-skinned, their faults rooting to shallow décollements – likely some mix of the interface between the smooth plains and the underlying regolith-covered basement and interbeds within the plains deposits themselves (e.g., Jerram and Widdowson, 2005) (Figure 10.7). Similar concentric folding of basalt flows above décollements has been described on Earth, with those in the Yakima fold belt that straddles the Washington–Oregon border (Last et al., 2012) and the Malaita anticlines at the Solomon Islands–Ontong Java collisional front (Petterson et al., 1997) among the best-known examples.

Where shortening landforms demarcate buried impact craters in smooth plains (Figure 10.1a), such structures were likely formed by the concentration of compressive stresses above crater rims (Watters et al., 2009a). Conversely, outward-verging monoclines and anticlines within impact basin rims may represent partitioning of shortening strain between the basin and its interior smooth fill, either as a result of a difference in elastic moduli between the fill and basin floor material or, as for the smooth plains structures, by the rooting of thrust faults into a décollement between the two deposits (e.g., Fegan et al., 2017). At some sites where shortening structures and impact craters interact, syntaxis is observed (Figure 10.8). This phenomenon occurs when the hanging wall of a thrust fault encounters an impediment, such as a crater’s central peak, and the continued propagation of the unobstructed portions of the fold form a distinct bend in the strike of the shortening structure, as is famously observed in the Himalaya (Suess, 1883).

Regions of high- and low-standing terrain on Mercury do not appear to correlate spatially with free-air gravity anomalies over the planet’s northern hemisphere, a result indicating that topography is largely isostatically compensated, presumably by variations in crustal thickness (e.g., Smith et al., 2012; James et al., 2015; Chapter 3). Those tectonic structures that border high-standing terrain may therefore have served to isolate thicker crustal blocks from neighboring, thinner portions of the crust, localizing substantial shortening along their length and accumulating considerable strain by penetrating far into the lithosphere. With continued shortening, thicker crustal blocks overthrust adjacent low-lying terrain, as on Earth (Suess, 1909; Sengör, 1993). Moreover, where smooth plains structures are located adjacent to, and share a dominant strike with,

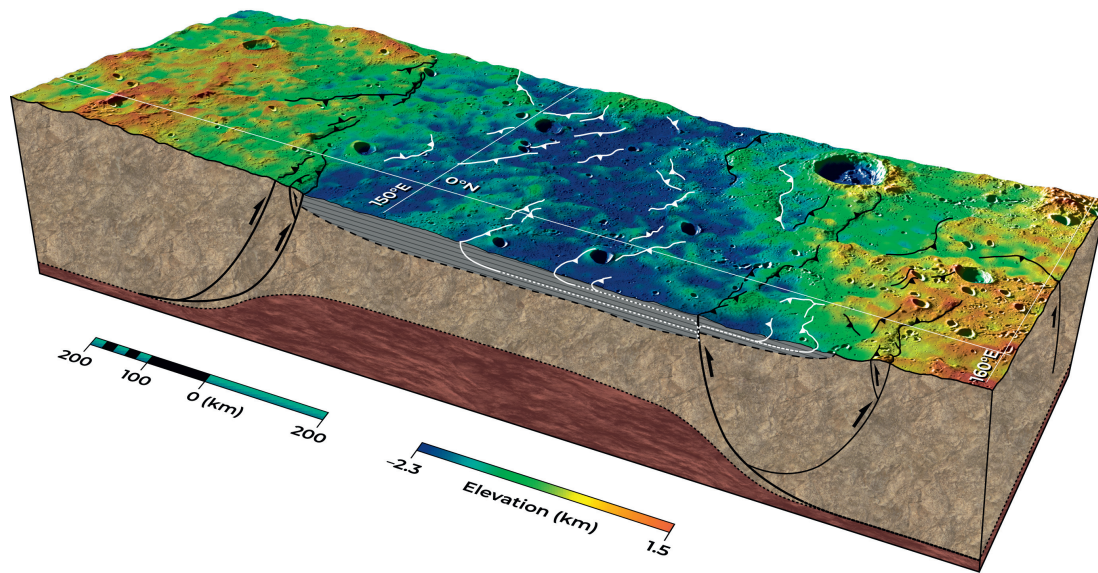


Figure 10.7. A schematic cross section showing the possible kinematic relations of thin- and thick-skinned shortening structures on Mercury. Here, thick crustal blocks are deformed and bounded by deep-seated “germanotype” structures (black lines), whereas low-lying smooth plains (dominantly consisting of ponded lavas) are shortened by thin-skinned “alpinotype” faults (white lines). These shallow structures may root into the deeper, larger faults, as observed widely on Earth. The black arrows indicate the direction of tectonic transport along the larger faults, which are shown here to bottom out at the crust–mantle boundary (dotted line). In cross-section, smooth plains material is shown in grey, older crustal material in light brown, and mantle material in dark brown. Features shown at depth are not to scale.

highland-bounding and cratered plains structures, the smaller “thin-skinned” structures may root into the deeper faults – a structural arrangement seen in the Alps (Trümpy, 1980), the European Hercynides (Bois et al., 1986), the Appalachian–Ouachita orogen (Hatcher, 1989), the Himalaya (McDougall et al., 1993), the U.S. Rocky Mountains (Stille, 1940), and the Andes (Roeder, 1988) (Figure 10.7). (Under this interpretation, the thin-skinned shortening landforms are cognates of Stille’s (1920) “alpinotype” structures, connected mechanically to the larger, deep-seated “germanotype” thrust faults.)

10.3 EXTENSIONAL STRUCTURES

Although thrust-fault-related landforms are by far the most abundant type of tectonic structure on Mercury, extensional deformation was also recognized in images acquired by the Mariner 10 spacecraft, albeit spatially restricted to the Caloris basin. Within these plains, Strom et al. (1975) noted a pattern of deformation unlike any seen elsewhere in the solar system, with a complex system of ridges and “fractures” arrayed throughout the observed portion of the basin floor. Noting their morphological similarity to graben and tension fractures on the Moon, Strom et al. (1975) considered these flat-floored, graben-like features to be extensional structures, an interpretation adopted by subsequent workers (e.g., Dzurisin, 1978; Melosh and McKinnon, 1988). (The term “fracture” to denote extensional landforms alone has since been abandoned, correctly, since shortening structures also fall under this general terminological description (Schultz and Fossen, 2008) but display a reverse sense of slip.)

Further evidence for extensional deformation on Mercury was not forthcoming until the MESSENGER spacecraft returned

images of the planet. Observations of the entirety of the Caloris basin revealed substantially greater structural complexity than had been seen by Mariner 10, including a vast network of radially oriented graben emanating from the basin center named Pantheon Fossae (Murchie et al., 2008; Watters et al., 2009c) (Section 10.6.4). These landforms were interpreted as graben, a structure formed where two parallel normal faults that are antithetic (dipping toward one another) bound a down-dropped block. This interpretation is consistent with their relatively straight walls, flat floors, and in some instances tapered ends, which correspond to slip displacements trending to zero at the fault tips. Moreover, there are numerous examples of normal fault segmentation and linkage, as evinced by ramps in overlapping stepover regions (relay structures) and by abrupt bends (jogs) in the fault traces (Klimczak et al., 2012, 2013a) (Figure 10.9a).

Perhaps more importantly, MESSENGER observations revealed evidence for extension at numerous other sites across the planet. For example, sets of basin-radial and -concentric graben have been documented in the volcanic plains interior to the Rembrandt basin (Watters et al., 2009b; Ferrari et al., 2015); smaller assemblages of graben have been noted in several mid-sized basins, including the Mozart, Rachmaninoff, and Raditladi basins (Prockter et al., 2009, 2010, 2011; Blair et al., 2013); and sets of graben multiple orientations have been described within numerous volcanically infilled craters (Freed et al., 2012; Klimczak et al., 2012; Watters et al., 2012) (Figure 10.9b). We describe these structures further in Section 10.6.4.

As a consequence of the progressive lowering of its periapsis altitude between orbit-correction maneuvers during its second extended mission (Chapter 1), the MESSENGER spacecraft was able to image the surface of Mercury at higher resolution than earlier in the mission. In consequence, MESSENGER

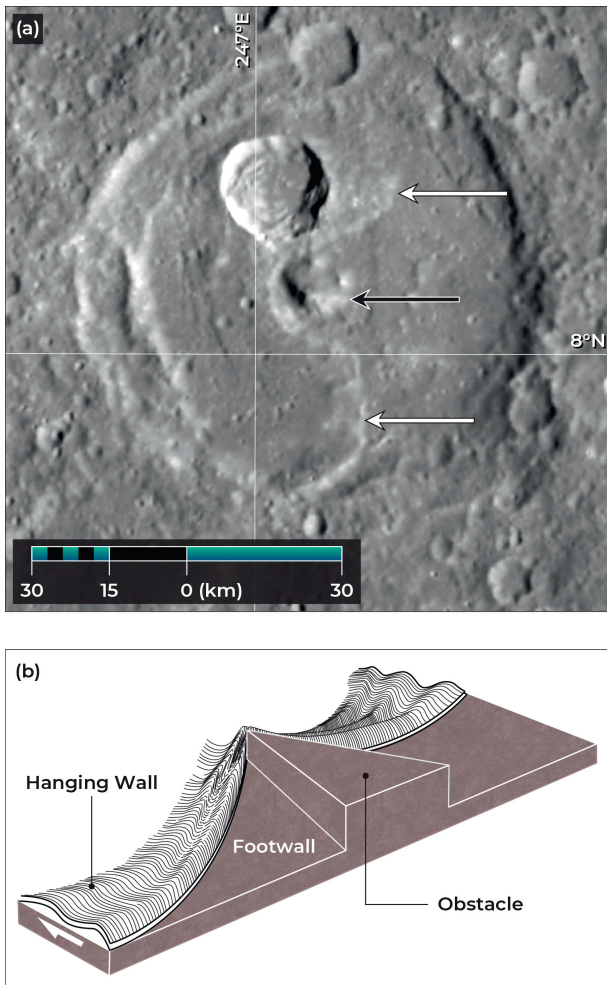


Figure 10.8. An example of syntaxis on Mercury. (a) A large shortening structure crosses an unnamed 80-km-diameter impact crater; where the fold meets the crater's central peak (shown by a black arrow) it is impeded, such that the entire shortening structure develops a pronounced bend in its leading edge (white arrows). Azimuthal equidistant projection, centered at 8.3°N, 247.3°E. (b) A schematic sketch of this phenomenon, showing the sharp bend in the hanging wall of a detachment fault upon encountering an obstacle.

imaged a set of narrow, trough-like landforms in the smooth plains units of relatively well-preserved craters, including Degas crater (Figure 10.9c). These troughs likely correspond to opening-mode fractures (also termed “joints”) and small graben, formed in the same manner as discussed below for larger graben, in thermally contracting impact melt and volcanic deposits (Freed et al., 2012; Klimczak et al., 2012; Watters et al., 2012) (Section 10.6.4).

Notably, extensional strains have been seen in only one structural setting other than within smooth plains units: as narrow graben sets along the crests of large shortening landforms (Banks et al., 2015). Similar structures have been recorded in comparable settings on other worlds (e.g., Plescia and Golombek, 1986; Mueller and Golombek, 2004). These narrow extensional landforms are strain-compatible with, and provide insight into the kinematics of, thrust faulting on Mercury (Section 10.2.1 and Figure 10.18). Another situation where extensional deformation is associated with shortening

structures is opposite large syntaxes of arcs (Wilson, 1954; Jacobs, 1959). No such deformation has yet been observed on Mercury, but whether this is because such extension does not exist there, or because it has yet to be resolved with image data, remains unclear.

10.4 LONG-WAVELENGTH TOPOGRAPHIC CHANGES

The record of brittle tectonic activity on Mercury was apparent from the earliest photographs returned to Earth by the Mariner 10 mission, and the study of these landforms has naturally tended to dominate investigations of the innermost planet’s tectonic history. Interestingly, however, there is another class of landform on Mercury that has been recognized only with MESSENGER data, and then only with topographic measurements: long-wavelength “warps” in the planet’s topography that have virtually no other surficial signature. We include a brief description and discussion of those landforms here, but the tectonic process through which they originated is by no means certain. Nonetheless, these warps are spatially collocated with tectonic landforms, and so their presence, geometry, and likely timing are worth briefly discussing here.

DEMs derived from stereophotogrammetric processing of MDIS flyby images showed long-wavelength variations in topography along the floor of the Caloris basin (Oberst et al., 2010). Orbital observations from the Mercury Laser Altimeter confirmed these topographic variations within the basin to be real and not artifacts of the DEM, and, further, revealed several similar long-wavelength undulations elsewhere across Mercury’s northern hemisphere (Zuber et al., 2012), including exterior to the basin (Klimczak et al., 2013a) (Figure 10.3b). These variations are apparent as east–west-oriented, elongate topographic highs and lows, far greater in length than in amplitude, and can be described as nearly sinusoidal in cross section (Klimczak et al., 2013a) (Figure 10.10). Within the Caloris basin, the wavelengths of these topographic undulations range from 850 km to up to 1120 km, with amplitudes of up to 2.5–3 km (corresponding to values of horizontal shortening strain, ε , of only $\sim 10^{-5}$) (Klimczak et al., 2013a). Surprisingly, some areas of the basin floor have even been vertically displaced to now lie above the basin rim (Zuber et al., 2012; Figure 10.10). In addition, the flat portions of the floors of many impact craters, including craters that are volcanically infilled and host floors that presumably once followed a gravitational equipotential surface, are tilted in the same direction as the downslope trend of the long-wavelength topography (Balcerzki et al., 2012; Zuber et al., 2012; see also the Atget crater in Figure 10.10).

Tilted crater floors and their relationships with long-wavelength topography can be observed at numerous other sites across Mercury’s northern hemisphere (Balcerzki et al., 2012), perhaps most prominently in association with a broad rise in the NSP some 1000 km across that stands ~ 1.5 km above the surrounding terrain (Zuber et al., 2012; Klimczak et al., 2012)

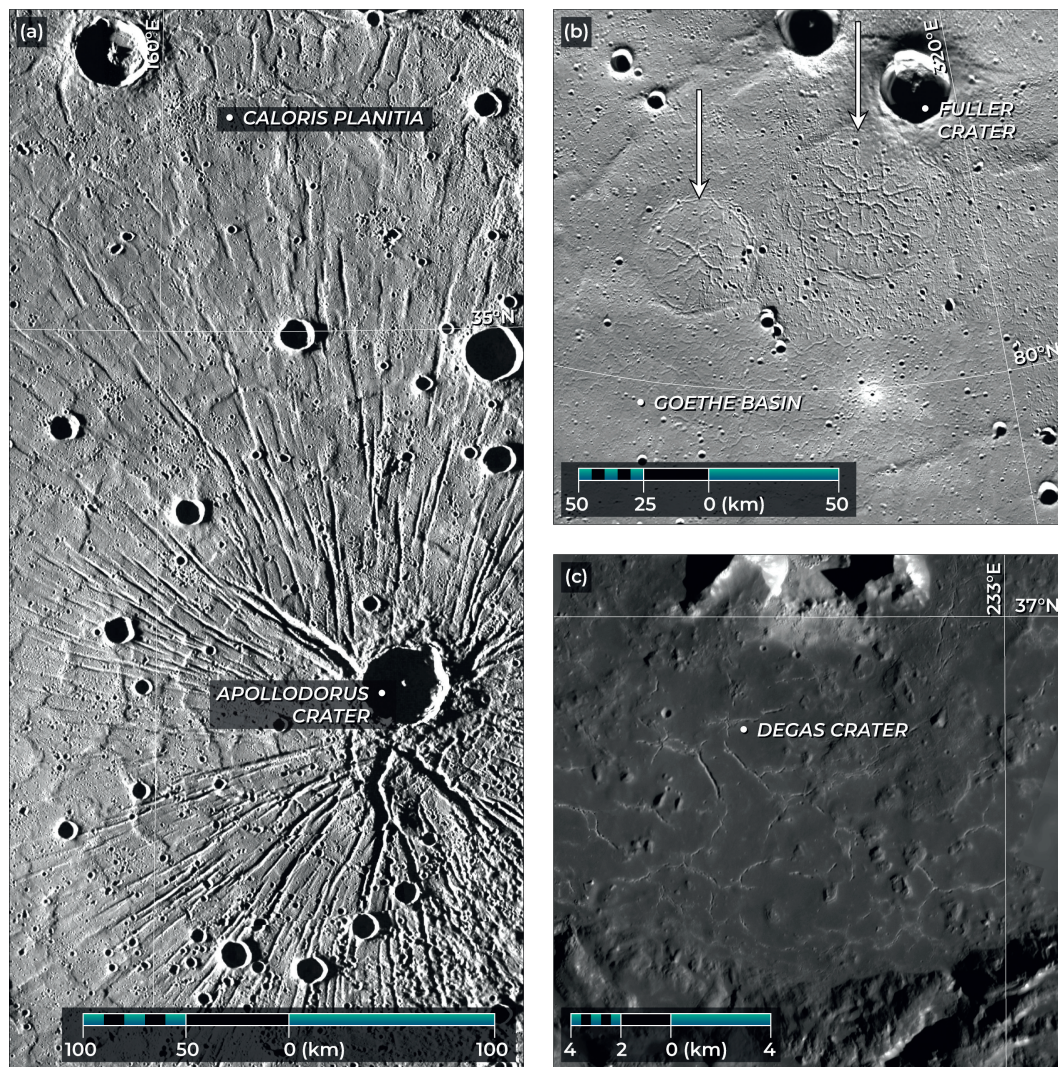


Figure 10.9. Examples of extensional landforms on Mercury. (a) A portion of Pantheon Fossae, the radial population of graben within the Caloris basin. (b) Graben with multiple orientations inside two ghost craters (white arrows), themselves situated within the 317-km-diameter Goethe basin. Note several additional graben immediately south of the larger of the two ghost craters. (c) Structures interpreted to be large joints and very small graben that formed within the impact melt deposit of the 55-km-diameter Degas crater. The crater's central peak and wall terraces are visible at the top and bottom of the image, respectively. Azimuthal equidistant projections, centered as follows: (a) 30.0°N , 161.0°E ; (b) 81.0°N , 309.0°E ; and (c) 60.3°N , 52.9°E . Images from the global morphology base map (Chabot et al., 2016).

(Figure 10.3b). On its flanks, the floors of both fresh and infilled craters tilt away from the center of that rise at angles similar to those of the flank slopes themselves (Klimczak et al., 2012). Undulations to the west of the Caloris basin have wavelengths and amplitudes of approximately 1300 km and 3 km, respectively (Klimczak et al., 2013a). Further, several of Mercury's small population of valles (impact-sculpted troughs shaped into flat-floored channels by lava: Section 11.2.1), situated at the periphery of the NSP, also show broad rises orthogonal to their long axes (Byrne et al., 2013b). These portions of elevated topography have wavelengths of several hundred kilometers and amplitudes of ~ 1 km; these changes in relief far exceed the local downhill gradient (Byrne et al., 2013b). Notably, the undulations that cross the valles strike approximately parallel to their larger counterparts near and within the Caloris basin, and all of these linear

crests and troughs are approximately circumferential to the northern rise (Figure 10.3a).

10.5 MERCURY'S LITHOSPHERE

Collating observations of tectonic landforms with measurements of Mercury's topography and gravity field provides information on the planet's interior structure. The structure, properties, and evolution of the interior of Mercury are examined at length elsewhere in this volume (Chapters 3, 4, and 19), but here we discuss the insights afforded by tectonic landforms into the planet's brittle and ductile lithospheric regimes (Sections 10.5.1 and 10.5.2, respectively), followed by a discussion of the likely structure of the lithosphere (Section 10.5.3).



Figure 10.10. A Mercury Laser Altimeter profile (shown in teal) across the central portion of the Caloris basin. The basin floor shows sinusoidal topographic undulations approximated with a wavelength of 850 km and an amplitude of 2.5 km (shown in pink). The profile, which has a vertical exaggeration of ~100:1, shows both the tilted floor of the Atget crater and where the highest elevations of the basin floor exceed those of the northern basin rim.

For a general overview of planetary lithospheres, including that of Mercury, see Chapter 3.

10.5.1 Mercury's Brittle Regime

As for any solid-surface body in the solar system, Mercury's lithosphere makes up its strong, deformable outer shell, as defined by its mechanical properties (Chapter 3). The lithosphere consists of brittle and ductile regimes, under which deformation is accommodated by localized fracturing processes and by distributed plastic flow, respectively (e.g., Kohlstedt and Mackwell, 2010). The brittle regime occupies the relatively cold, upper part of the lithosphere. Deformation here is manifest as fractures, with two major fracture modes observed across the surface of the planet: mode-I or tensile fractures (joints: Section 10.3 and Figure 10.9a) and mode-II and -III or shear fractures (faults: Figures 10.1, 10.9b, and 10.9c). Tensile and shear fractures form only when tectonic stresses meet the respective strengths of the volume of rock that is subject to these stresses. Therefore, a characterization of the magnitude, direction, and orientation of stresses is crucial for understanding brittle rock behavior in Mercury's lithosphere.

Several geophysical processes have been invoked to produce regional-to-global fracture patterns under Mercury's brittle regime. Stress models for these processes have been derived for global contraction (e.g., Melosh and McKinnon, 1988), tidal despinning (e.g., Melosh, 1977), thermal expansion or contraction (e.g., Turcotte, 1983), polar wander (e.g., Melosh, 1980), and mantle convection (e.g., Solomatov and Moresi, 2000), and then compared with the observed pattern of tectonic landforms.

In addition, a variety of non-tectonic processes introduce discontinuities and tensile fractures into Mercury's lithosphere, such as the cooling of emplaced volcanic units and impact melts (e.g., Freed et al., 2012; Klimczak et al., 2012; Watters et al., 2012; Figure 10.9a), impact damage (Melosh, 1984; Ahrens and Rubin, 1993; Xia and Ahrens, 2001; Collins et al., 2004), and igneous intrusion. The depth and degree of fracturing of Mercury's lithosphere is poorly determined, but first-order estimates inferred from deep mines (Bieniawski, 1989) and boreholes (Emmermann and Lauterjung, 1997) on Earth, as well as from seismic (Dainty et al., 1974; Toksöz et al., 1974) and

gravity data analyses for the Moon (Wieczorek et al., 2013), suggest that Mercury's lithosphere may be moderately to heavily fractured to depths of ~15 km (Klimczak, 2015). Brittle deformation within Earth's lithosphere can extend to depths of tens of kilometers and so, accounting for the effect of gravitational acceleration on the penetration depth of fractures (e.g., Klimczak, 2015; Heap et al., 2017), quakes on Mercury at depths considerably greater than 15 km are likely.

Most stress models considered to date for the processes listed above have been purely elastic, and so the stress magnitudes derived from these models depend on the elastic rock properties, e.g., Poisson's ratio (ν) and Young's modulus (E) (or the closely related shear modulus, G). Poisson's ratio, a measure of the shortening in the direction of an applied load relative to the lengthening in the direction perpendicular to that load, is often taken to be 0.25 ± 0.05 in basalts (Schultz, 1995). Young's modulus describes the resistance of a material to elastic deformation (essentially its longitudinal "stiffness") and, for intact basaltic rock samples, laboratory measurements yield values of $E \approx 70\text{--}100$ GPa (Schultz, 1993).

The use of Young's modulus in elastic stress models, however, is appropriate only for rock samples intact at the hand-sample scale (Walsh, 1965; Kulhawy, 1975; Segall, 1984; Kachanov, 1992; Schultz, 1996). At larger scales, no rock volume is intact, and so stresses in Mercury's lithosphere are more appropriately modeled by incorporating some degree of lithospheric fracturing (e.g., Klimczak, 2015; Klimczak et al., 2015). The resistance to elastic deformation of a fractured volume of rock, termed the *in situ* modulus of deformation (E^* , Bieniawski, 1989), is relatively insensitive to rock type, with several empirical studies establishing some relationship to the degree of fracturing (see the summary by Hoek and Diederichs (2006) for more information). For low degrees of fracturing within Mercury's lithosphere, the deformation modulus $E^* \approx 40\text{--}70$ GPa and, for moderate degrees of fracturing, a deformation modulus of $E^* \approx 5\text{--}15$ GPa is appropriate (e.g., Klimczak et al., 2015).

Faults are, by far, the most prominent and largest fractures in Mercury's lithosphere (Section 10.2) (Figures 10.1, 10.3, and 10.9). The formation and growth of a given fault population is dependent on the brittle strength of the lithosphere, which is a

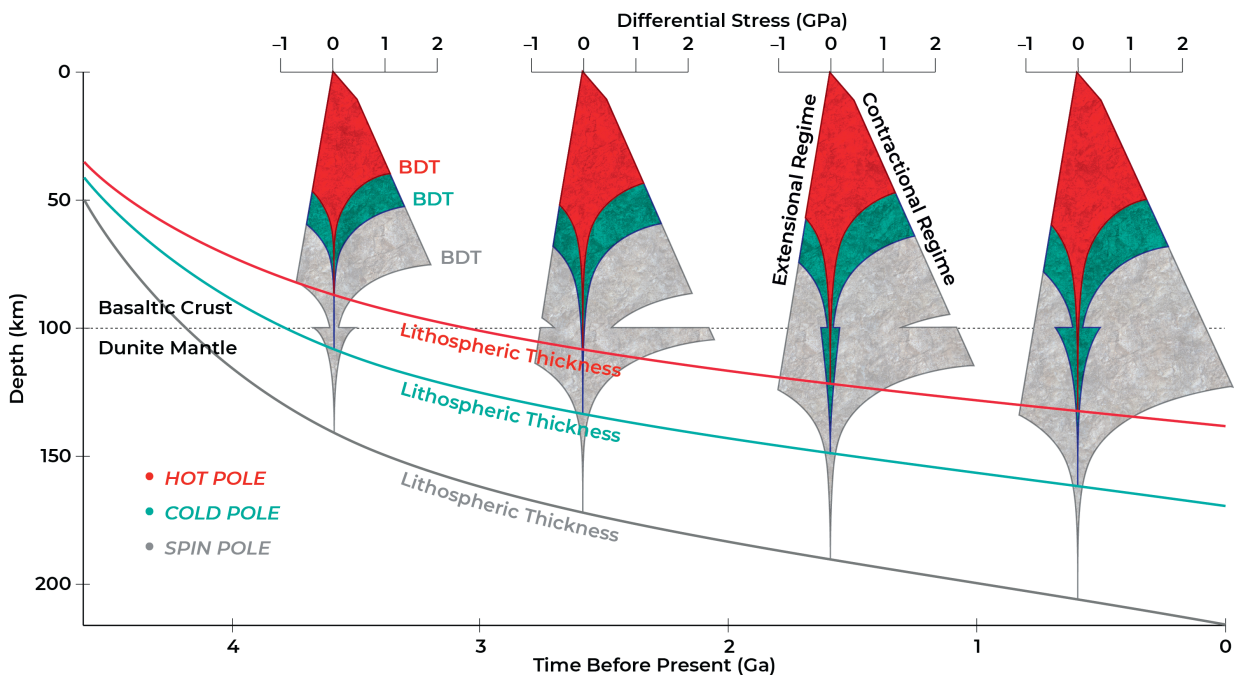


Figure 10.11. One possible scenario for the evolution of lithospheric strength and thickness for Mercury’s different thermal environments, shown for the equatorial hot (red) and cold (teal) poles as well as the spin poles (gray) for both extensional and contractional tectonic regimes. The brittle regime is represented with Byerlee’s law (after Klimczak, 2015); the lithospheric thickness and ductile regime are modified after the models of Williams et al. (2011). Lithospheric strength envelopes are shown in 1 Ga increments after Mercury’s formation, for a horizontal strain rate of 10^{-19} s^{-1} and for ductile flow laws appropriate to a dry basaltic crust and a dry dunite mantle (with their interface shown here for an exemplar depth of 100 km). Note that brittle strength is independent of rock type, but the ductile portions of the strength envelopes vary with the flow law of the mineral that limits the rate of deformation. The brittle–ductile transition (BDT) is defined as the depth at which the brittle and ductile portions of the strength envelopes intersect.

measure of the amount of stress that can be withheld by the lithosphere without permanent deformation; this value is dominated by the frictional properties of the rock volume. Under the assumption that Mercury’s lithosphere contains fractures of all orientations, stresses within the lithosphere must overcome the frictional resistance to sliding for rock failure to occur along a fracture plane optimally oriented for such sliding (e.g., Byerlee, 1978). Friction between fracture planes has been shown to be independent of rock type, fracture surface roughness, and slip rates (e.g., Byerlee, 1968, 1978; Barton, 1976). The coefficient of friction, μ , for Mercury’s lithosphere is likely therefore to be consistent with the narrow range of values of $0.6 < \mu < 1.0$ observed for faults on Earth.

Importantly, we must have an understanding of how a rock will respond to an applied stress, for which we use failure criteria: if the stress applied to a given rock volume meets such a criterion, we assume that failure occurs. Failure criteria previously used to characterize the brittle strength of Mercury’s lithosphere include Byerlee’s law (e.g., Zuber et al., 2010; Williams et al., 2011; Klimczak, 2015), the Coulomb criterion (Klimczak, 2015), and the Hoek–Brown criterion (Klimczak, 2015; Klimczak et al., 2015). These criteria allow for the assessment of the resistance of fractures to frictional sliding for an increasingly complex set of boundary conditions, such as the incorporation of rock cohesion (the Coulomb and Hoek–Brown criteria) and accounting for

various degrees of pre-existing fracturing in the lithosphere (the Hoek–Brown criterion).

In their simplest form, lithospheric strength envelopes (the change of strength with depth) calculated with Byerlee’s law in the brittle regime describe a linear dependence on depth of the maximum stresses permissible in the lithosphere for both intermediate- and high-pressure conditions (Brace and Kohlstedt, 1980; Kohlstedt and Mackwell, 2010) (Figure 10.11). Differential stresses demarcate the limits of stable conditions and so indicate when faulting – frictional sliding on pre-existing zones of weakness – will be triggered (Figure 10.11). These stresses are defined as the difference between the lithospheric strength and the reference state of stress, which is usually taken as the overburden pressure, or “lithospheric state of stress”: the weight of the rock column at a given depth below the surface. Note that, in Figure 10.11, conditions for frictional sliding are given for entirely compressive stress states; tensile stresses instead trigger opening-mode deformation and thus the formation of joints [for details see Klimczak et al. (2015)].

A horizontal, tectonically governed stress component in a lithosphere, σ_H , that is greater than the stress component acting vertically, σ_V (where $\sigma_H > \sigma_V > 0$, with compressive stress taken to be positive), yields positive stress differences. These stresses, in turn, define a contractional tectonic regime under which thrust faults form (e.g., Anderson, 1951; Engelder, 1992) if

the stress differences in the lithosphere reach their maximum permissible values (Figure 10.11). The planet-wide presence of thrust-fault-related landforms on Mercury (Figure 10.3a) indicates that stresses reached the compressive strength of the lithosphere, and thus that such a stress state was globally dominant. This conclusion supports the early inferences from Mariner 10 data that Mercury experienced lithospheric shortening on a global scale (e.g., Strom et al., 1975).

Negative stress differences (i.e., $\sigma_H < \sigma_V$, where $\sigma_V > \sigma_H > 0$) define an extensional tectonic regime (Figure 10.11) that allows for the formation of normal faults and graben (e.g., Anderson, 1951; Engelder, 1992) and facilitates volcanism by providing favorable conditions for the vertical ascent of magma and the formation of rift zones and dikes (Section 11.7.2). The asymmetry between the two sides of the brittle portion of a strength envelope (Figure 10.11) illustrates that a lithosphere under extension is much weaker than one under a contractional regime, and so it is easier to overcome the resistance to frictional sliding to form normal faults. However, joints, normal faults, and graben on Mercury are spatially restricted to relatively late effusive volcanic deposits (Figure 10.3a; Section 10.3), indicating that any extensional stress states within Mercury's lithosphere for which evidence remains today have been present only regionally.

10.5.2 Mercury's Ductile Regime

At depths where temperatures are sufficiently high to activate plastic microdeformation mechanisms, such as dislocation glide or diffusion creep (e.g., Passchier and Trouw, 2006), rocks behave in a ductile manner via plastic flow (e.g., Kohlstedt and Mackwell, 2010). Ductile strength is strongly dependent on temperature, viscosity (and thus mineralogy), and strain rate (e.g., Kohlstedt et al., 1995); the respective strength envelope is typically assumed to follow a decrease with depth governed by a non-linear (e.g., power-law) relation between stress and strain rate (Figure 10.11). Ductile-strength models are sensitive to geothermal gradient and most often are constructed for a constant strain rate, a uniform lateral distribution of deformation, and the premise that the strength of the entire lithosphere under the ductile regime is governed by a single mineralogy (usually that which displays the weakest rheology). Mercury's ductile strength has typically been modeled with the rheology of a dry (anhydrous) basalt (Zuber et al., 2010; Williams et al., 2011; Egea-González et al., 2012) or of dry anorthosite in the crust (Nimmo and Watters, 2004; Williams et al., 2011) and dry dunite in the mantle (Nimmo and Watters, 2004; Zuber et al., 2010; Williams et al., 2011). The depth to the crust–mantle interface within Mercury has variously been taken to be less than 140 km (Nimmo and Watters, 2004), or about 50 km (Zuber et al., 2010), or around 100 km (Zuber et al., 2010; Williams et al., 2011). Analysis of MESSENGER topography and gravity measurements place the crust–mantle boundary in Mercury's northern hemisphere at ~35 km depth (Padovan et al., 2015).

Different assumptions for flow laws and crust–mantle boundary depths can lead either to a small strength contrast between the crust and mantle or to a lower crustal weak zone that serves to mechanically decouple the crust and mantle (e.g., Williams et al., 2011). For a scenario under which the crust and mantle are

coupled and have a modest difference in strength, tectonic deformation at the surface will likely also be coupled to strain throughout the entire lithosphere and so may directly reflect mantle processes (e.g., Kohlstedt and Mackwell, 2010). In turn, brittle deformation initiated at the surface might root into broader shear zones when reaching the ductile regime (e.g., Cowie et al., 2013). It may be that strain localization by plastic microdeformation mechanisms in Mercury's ductile regime leads to dynamic recrystallization (whereby new mineral grains grow in response to stress rather than chemical potential) and thus a heterogeneous lateral distribution of deformation in Mercury's lower crust and upper mantle. Excavation of this portion of Mercury's lithosphere (e.g., by impact) could, under this scenario, reveal a range of structural rock types (e.g., Şengör and Sakinç, 2001) characterized by their deformation history (rather than lithology), including mylonites, cataclasites, and pseudotachylites.

10.5.3 Lithospheric Structure

With increasing depth and temperature, rock behavior transitions from brittle to semi-brittle to ductile. This transition is commonly termed the brittle–ductile transition (BDT). The depth of the BDT is generally taken to be the depth at which the brittle and ductile strengths of the lithosphere are equal and thus by the locus of where the brittle and ductile strength envelopes intersect (Figure 10.11). In such strength models, the BDT is manifest as an abrupt change between the two regimes. In reality, though, the transition from fully brittle to fully ductile behavior probably occurs more gradually with depth across a semi-brittle or plastic zone in which microdeformation mechanisms that allow for some relaxation of stress become activated at points of stress concentrations (e.g., Kohlstedt et al., 1995). Moreover, given that the depth of the BDT on Earth varies spatially as a function of rock type, geothermal gradient, and other factors (e.g., Gettings, 1988), similar spatial variations are likely to occur in Mercury's lithosphere.

The topography of a fault-related landform can be used to infer the geometry of the underlying fault itself (Klimczak, 2014; Byrne et al., 2015), which in turn can place estimates on the depth of the seismogenic layer, the surface heat flow, and the depth of the BDT at the time of faulting. Analysis of topographic profiles across several thrust-fault-related landforms, including Discovery Rupes (Watters et al., 2002; Nimmo and Watters, 2004), a group of three unnamed monoclines in the equatorial region (Ritter et al., 2010), and a set of four structures including Santa Maria Rupes (Egea-González et al., 2012), provided preliminary estimates of such parameters for Mercury. In each case, the maximum depths to which these faults were found to have propagated were between 30 and 40 km (Watters et al., 2002; Ritter et al., 2010; Egea-González et al., 2012), giving a candidate depth to the BDT in that range (e.g., Nimmo and Watters, 2004; Williams et al., 2011). It is important to note, however, that faults may root into zones of mechanical weakness in the lithosphere that do not correspond to the BDT itself, and also that the BDT has likely grown deeper since those faults developed (Figure 10.11) – and so this depth range is but a minimum for present-day conditions.

Models for the evolution of Mercury's lithosphere that include the effect of latitudinal and longitudinal variations in surface temperature (Vasavada et al., 1999) on lithospheric strength and thickness over time (Figure 10.11) indicate that substantial differences in lithospheric strength arise when lateral variations in Mercury's thermal structure are considered (Williams et al., 2011). After the end of the LHB, when most thrust-fault-related landforms observed today are believed to have formed (Banks et al., 2015) (Section 10.8), differences of up to 15 km in lithospheric thickness developed in Mercury's equatorial region between hot- and cold-pole latitudes, and even greater lithospheric thicknesses developed at the spin poles (Figure 10.11). Williams and co-workers (2011) suggested that the differences in lithospheric strength and thickness may be expressed in the localization, orientation, and depth of deformation of Mercury's tectonic structures.

10.6 TECTONIC PROCESSES

The tectonics of Mercury have been dominated by the process of global contraction from secular interior cooling, but other tectonic mechanisms have shaped the planet as well. Although extensional structures are rare, where they occur they are abundant, and their origin must be explained against a backdrop of planetary contraction. Further, not all of the shortening structures on Mercury necessarily trace their formation to global contraction. And other, planetary-scale processes may have operated throughout Mercury's history, perhaps not in a dominating role like global contraction but to an extent sufficient to shape at least in part the distribution and character of tectonic deformation we see today.

In Section 10.6.1, we first discuss the causes, effects, and means to estimate the amount of global contraction. We then review the process of tidal despinning (Section 10.6.2), before appraising the effects of both processes acting together (Section 10.6.3). Finally, in Section 10.6.4, we discuss in detail the processes that drove extensional deformation within myriad volcanically flooded impact craters and basins on Mercury.

10.6.1 Global Contraction

As we noted in Section 10.1.1, Strom et al. (1975) invoked global contraction [possibly arising from phase changes in the core (Murray et al., 1974)] to account for the widespread distribution of shortening structures they observed. Secular cooling of a planetary body will lead to a reduction in volume of the interior relative to the lithosphere, causing an increase in horizontal compressive stresses and a consequent failure mode favoring large-scale thrust faulting of that lithosphere (Élie de Beaumont, 1829, 1852; Solomon, 1978). In contrast to other global-scale processes (Sections 10.6.2 and 10.7), global contraction is not predicted to produce a distinctive pattern of faulting, *per se*. Instead, absent the superposition of other sources of stress or a pre-existing structural fabric, the resultant compressive stresses are horizontally isotropic, and so the ensuing shortening structures should be distributed evenly across the surface without preferred orientations (e.g.,

Solomon, 1977) – much like on the surface of a shrinking apple, an analogy first proposed for Earth by Ægidius Romanus in the thirteenth century (Dana, 1863).

Both Mariner 10- and MESSENGER-based observations indicated that Mercury's shortening tectonics are not homogeneously distributed across its surface (e.g., Strom et al., 1975; Melosh and McKinnon, 1988; Byrne et al., 2014) (Figure 10.3a). The degree to which the distribution of crustal shortening deviates from that predicted solely from global contraction simply as a result of lighting bias (Section 10.2.2) rather than because of other contributory processes (Section 10.7) has yet to be determined. Even so, global contraction remains the most plausible mechanism with which to account for the planet-wide population of shortening structures mapped on Mercury (e.g., Byrne et al., 2014), and those structures can in turn provide bounds on the amount by which the planet has decreased in volume.

For example, from their assessment of Mercury's population of shortening structures visible with Mariner 10 data, Strom et al. (1975) estimated that the planet has experienced a reduction in radius of 1–2 km since a time near the end of the LHB (Section 10.1.1). Later studies of Mercury's tectonics from Mariner 10 and early MESSENGER observations offered similar estimates (Watters et al., 1998, 2009a; Watters and Nimmo, 2010), bracketed by values from as low as ~0.8 km (Watters et al., 2015) to as much as 3.6 km (Di Achille et al., 2012). Of course, all of these values were derived from the observed thrust-fault-related landforms alone and did not account for lithospheric strength, nor that some portion of the compressive stresses imposed on a lithosphere by global contraction can be accommodated before the frictional resistance to sliding on lithospheric faults is overcome (Section 10.5.1). Importantly, this additional component of radius change amounts to ~0.4–2.1 km, is preserved in the lithosphere even after thrust faulting is initiated (Klimczak, 2015), and so must be added to any radius change estimates made from mapped shortening structures alone (Section 10.8.1).

In any case, such mapping-based estimates were consistently below those predicted from thermal history models of Mercury, which generally returned radius change values of ~5–10 km (Solomon, 1977; Schubert et al., 1988; Hauck et al., 2004; Dombard and Hauck, 2008). Only when considering a restricted set of model parameters (including “extraordinary compositions”), or invoking hidden shortening strain on Mercury, could the constraint of 1–2 km of radius reduction since the LHB be even approximately satisfied (e.g., Dombard and Hauck, 2008).

With their global survey of mapped structures, Byrne et al. (2014) produced revised estimates for the accumulated decrease in Mercury's radius using fault displacement and length data. Several earlier studies employed this technique (e.g., Watters et al., 1998, 2009a; Watters and Nimmo, 2010; Di Achille et al., 2012), whereby a linear scaling relation (set by a proportionality constant γ) between maximum fault displacement (D_{\max}) and fault length (L) is established for a subset of a total fault population; this scaling ratio is then extrapolated to calculate the strain accommodated by the entire fault population from their mapped lengths alone (Scholz and Cowie, 1990; Cowie et al., 1993). Byrne et al. (2014) determined, for 216 monoclines

Table 10.2. *The decrease in radius of Mercury since the LHB, inferred from mapped shortening structures and calculated with the displacement-length scaling method (after Byrne et al., 2014).*

Fault plane dip angle	25°	30°	35°
Derived value of γ	9.6×10^{-3}	8.1×10^{-3}	7.1×10^{-3}
Radius change (km) from all (5934) structures			
Surface area of Mercury ($7.48 \times 10^{13} \text{ m}^2$)	6.9	5.6	4.6
Surface area excluding the Caloris and Rembrandt interior plains ($7.27 \times$ 10^{13} m^2)	7.1	5.7	4.7
Radius change (km) from all (2183) structures in areas outside of smooth plains			
Surface area of Mercury ($7.48 \times 10^{13} \text{ m}^2$)	4.6	3.7	3.1
Surface area excluding smooth plains and the Caloris and Rembrandt interior plains ($5.46 \times$ 10^{13} m^2)	6.3	5.1	4.2

and anticlines across Mercury for which the lengths had already been measured, the maximum relief of those landforms. This value is assumed to correspond, in the absence of subaerial erosion, to the vertical component (i.e., the throw, t) of the underlying fault (Figure 10.2). These workers then calculated D_{\max}/L ratios (i.e., γ) by finding the best-fit linear regression scaling statistic γ (Clark and Cox, 1996) for values of fault dip angle, θ , of 25° , 30° , and 35° , values used in previous such analyses (e.g., Watters and Nimmo, 2010; Di Achille et al., 2012). By computing the surface lengths of all mapped thrust faults (i.e., Figure 10.3a), Byrne et al. (2014) found their representative displacements with the appropriate scaling relation for an assumed dip angle. Cumulative shortening strains and corresponding changes to Mercury's radius were then obtained for the entire surface area of the planet, for that portion of the surface that excludes the Caloris and Rembrandt interior plains, and for that portion that excludes all smooth plains units (Byrne et al., 2014); these results are given in Table 10.2.

The areas of the Caloris and Rembrandt interior plains were omitted as part of this analysis because, although the plains host substantial structural complexity (Section 10.6.4), the extent to which those structures can be attributed to global contraction rather than basin-related processes is not well understood (Byrne et al., 2014). The areal shortening strain accommodated by all mapped structures outside those plains corresponds to a change in planetary radius of 7.1 km, 5.7 km, and 4.7 km for $\theta = 25^\circ$, 30° , and 35° , respectively (Byrne et al., 2014) (Table 10.2). Although smooth plains structures have been attributed to global contraction in some studies (e.g., Freed et al., 2012), they have also at least partially been ascribed to load-induced flexure and subsidence (e.g., Melosh and McKinnon, 1988; Watters et al., 2005) (Section 10.6.4), and so have been left out of other estimates of global contraction (e.g., Watters et al.,

2013). Byrne et al. (2014) therefore also calculated values of radial contraction from areal shortening strains excluding any contributions from smooth plains units. Such an analysis requires that no smooth plains units on Mercury experienced the effects of global contraction, which is geologically implausible since there are no large structures at the peripheries of these units into which shortening strains have obviously been partitioned. Moreover, there is evidence for the formation of a relatively young population of monoclines on Mercury (Section 10.8.1), and thrust fault reactivation has been observed in the Caloris basin (Section 10.8.2); both types of observation are consistent with sustained global contraction into the geologically recent. Nonetheless, when the corresponding surface area of smooth plains [$\sim 27\%$ of the total planetary surface: Denevi et al. (2013)] was disregarded, together with that of the Caloris and Rembrandt interior plains, the change in planetary radius since the LHB for $\theta = 25^\circ$, 30° , and 35° is 6.3 km, 5.1 km, and 4.2 km, respectively (Byrne et al., 2014) (Table 10.2).

Even accounting for various combinations of smooth and cratered plains structures, these values are all substantially greater than those from earlier photogeological studies. Previous reports of 0.8–2 km of radial shortening (Strom et al., 1975; Watters et al., 1998; Watters and Nimmo, 2010) were derived from analyses of the 45% of Mercury's surface imaged by Mariner 10. Yet the arrival of MESSENGER at Mercury did not herald the end of underreported radial shortening: a displacement-length scaling analysis with MDIS data considered only a subset of the monoclines and symmetric anticlines on Mercury and returned a value of ~ 1.0 km for $\theta = 30^\circ$ (Watters et al., 2015). Even the highest previously reported value for radius change (3 km for $\theta = 30^\circ$) was based on an analysis of but one-fifth of Mercury's surface imaged by MESSENGER that was then extrapolated to the entire planet (Di Achille et al., 2012), and that study adopted a D_{\max}/L ratio derived by Watters and Nimmo (2010) from only eight monoclines imaged by Mariner 10.

In comparison, the $D_{\max}-L$ analysis of Byrne et al. (2014), obtained with a scaling relation derived from 27 times as many structures as previous analyses and applied to the entire population of shortening structures on Mercury, gives a value for radial contraction of 5.7 km (5.1 km if smooth plains structures are excluded) for $\theta = 30^\circ$ (Table 10.2). Even these estimates of radius change accommodated by shortening landforms are likely to underestimate the actual extent of Mercury's global contraction since the LHB, in part because of limitations on illumination geometry in many areas of the base map used in that study (Byrne et al., 2014). Further, the history of Mercury's global contraction as recorded in its shortening structures is incomplete, since the planet experienced an initial reduction in radius without concomitant brittle deformation (see the discussion above, as well as Section 10.8.1).

As an independent check on this analysis, Byrne et al. (2014) also summed, along eight great circles, individual estimates of horizontal shortening across the 216 structures described above. Again, under the assumption that the relief of a given landform corresponds to the vertical component or throw, t , of the offset of the underlying fault, the horizontal component (the heave, h) of the fault offset along the great circle was calculated from the relation $h = t \tan^{-1} \theta$ (Figure 10.2). (For structures for which the

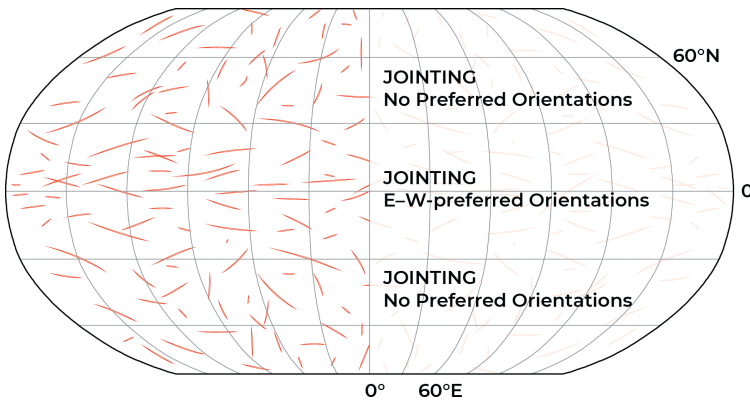


Figure 10.12. The global pattern of joints predicted to result from tidal despinning alone (after Klimczak et al., 2015). In the equatorial regions, east–west-oriented jointing is expected to form, in contrast to randomly oriented joints near the poles. The map is in a Robinson projection centered at 0°E; the graticule is in 30° increments of latitude and longitude.

strike direction was not orthogonal to a great circle, apparent dip, θ_a , was determined from θ with the relation $\theta_a = \tan^{-1}(\tan\theta \sin\psi)$, where ψ is the angle between the structure's strike direction and the great circle.) The change in planetary radius, ΔR , accommodated along each great circle was then calculated by $\Delta R = h_{\text{CUMULATIVE}}(2\pi)^{-1}$. For assumed dip angles once more of 25°, 30°, and 35° for the thrust faults underlying each shortening landform, this method returned a change in planetary radius averaged over the eight great circles of 5.5 km, 4.4 km, and 3.7 km, respectively (Byrne et al., 2014).

These results provide an important constraint for understanding the thermal history of Mercury's interior (Chapter 19). MESSENGER orbital measurements of the relative surface abundances of K, U, and Th (the major heat-producing elements in planetary interiors) indicate larger fractions of K and U and their comparatively shorter-lived isotopes (Peplowski et al., 2011; Chapter 2) than had been used in earlier thermal evolution studies (e.g., Hauck et al., 2004). It is therefore likely that Mercury experienced a greater change in heat production since the LHB (and so has cooled more) than earlier models had suggested (Chapter 19), further exacerbating the mismatch between theoretical findings and previous photogeological observations. Moreover, the finding of changes in Mercury's radius of up to a factor of 7 greater than previous results resolved a nearly four-decades-old paradox – which arose in the first place because of incomplete mapping – by making consistent the history of heat production and loss and the accumulated global contraction of Mercury (Solomon, 1977; Schubert et al., 1988; Dombard et al., 2008; Byrne et al., 2014).

10.6.2 Tidal Despinning

Mercury is locked in a 3:2 spin–orbit resonance, in which it rotates in a prograde manner precisely three times about its spin axis for every two orbits about the Sun. Mercury's current rotational period is approximately 59 Earth days, but its initial rotational period may have been as short as 20 Earth hours, as its spin angular momentum would then have compared well with those of most other planets (Kaula, 1968; Burns, 1975). Importantly, a decrease in spin rate by tidal torques would have been accompanied by the relaxation of an equatorial bulge (Burns, 1976; Melosh, 1977; Melosh and McKinnon, 1988). The stresses resulting from the relaxation of such a tidal bulge

were predicted to have been sufficiently large to have pervasively fractured the planet's lithosphere, producing a distinctive “despinning” pattern (Melosh, 1977; Melosh and Dzurisin, 1978; Melosh and McKinnon, 1988). This pattern was interpreted to include an equatorial province of north–south-oriented thrust faults, a zone of strike-slip faults in the mid latitudes, and a region of east–west-oriented normal faulting in the polar regions. More recent modeling that incorporated variations in lithospheric thickness resolved a despinning stress distribution that was interpreted to produce an equatorial set of strike-slip faults and a population of east–west-oriented normal faults at the poles (Beuthe, 2010).

Stress magnitudes and orientations arising from tidal spin-down alone were later assessed with failure criteria (Section 10.5.1) and were found to result in a fracture pattern composed only of a set of surficial joints (Klimczak et al., 2015) (Figure 10.12). This work showed that, regardless of the degree of pre-existing fracturing and corresponding strength of the lithosphere, the presence of tensile stresses at all latitudes predicts jointing across Mercury's surface. Moreover, for low to moderate degrees of lithospheric fracturing, the stress magnitudes were found to be insufficient to promote frictional sliding at depth, and so despinning alone would have produced no global faulting pattern at all (Klimczak et al., 2015).

10.6.3 Global Contraction with Tidal Despinning

Although Mariner 10 observations of the distribution and orientation of thrust-fault-related landforms on Mercury suggested that tidal despinning had played at least some role in their formation, early studies determined that despinning alone was not sufficient to explain all such observations (Dzurisin, 1978; Melosh and Dzurisin, 1978). MESSENGER observations of a global set of thrust faults but a general lack of normal and strike-slip faults (Byrne et al., 2014; Figure 10.3a), in contrast, indicate that a tectonic pattern from tidal despinning was either not preserved, was overprinted, or was strongly affected by global contraction, depending on whether the despinning process pre-dated or overlapped (at least in part) with global contraction (Klimczak et al., 2015).

Indeed, global stress distributions were modeled for a scenario under which despinning and contraction acted in concert (Pechmann and Melosh, 1979; Dombard and Hauck, 2008;

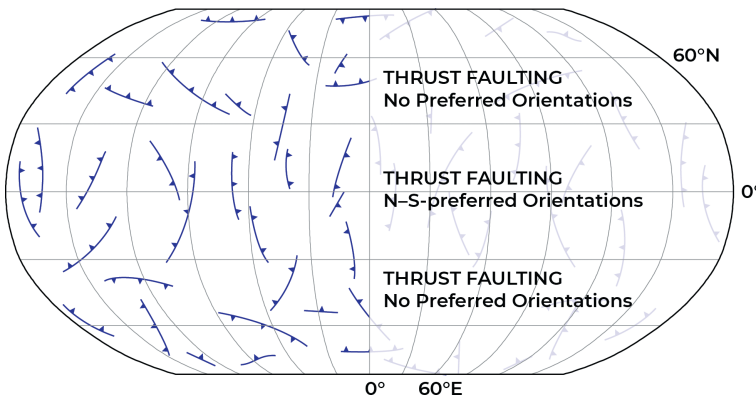


Figure 10.13. The global pattern of thrust faults on Mercury predicted to result from the overlapping of tidal despinning and global contraction. North–south-oriented thrust faults are predicted to develop at low latitudes, with randomly oriented thrust faults forming at the poles. The map is in a Robinson projection centered at 0°E; the graticule is in 30° increments in latitude and longitude. After Klimczak et al. (2015).

Beuthe, 2010). In all cases, fault patterns resulting from combinations of stresses from global contraction and tidal despinning were predicted to produce a global population of thrust faults with preferred north–south orientations at low to mid latitudes, although differences in the interpretation of the stress pattern led to variations in the predicted faulting style and/or orientation at higher latitudes (e.g., Pechmann and Melosh, 1979; Beuthe, 2010; Klimczak et al., 2015).

The tectonic maps of Mercury derived from MESSENGER orbital data (e.g., Byrne et al., 2014; Figure 10.3a) enable model predictions for various despinning and radius change scenarios to be comprehensively compared with tectonic observations from across the entire planet (Klimczak et al., 2015). For example, both Byrne et al. (2014) and Watters et al. (2015) reported a preponderance of north–south thrust fault orientations at equatorial and mid latitudes on the planet. At higher latitudes, however, a range of thrust fault orientations was found by Byrne et al. (2014), whereas Watters et al. (2015) reported a predominantly east–west-oriented set of thrust faults. This difference in interpretation of the tectonic fabric on Mercury likely results again from the use of different mapping criteria: Watters et al. (2015) chose to record only those thrust-fault-related landforms with several hundred meters of relief and more than 50 km in length, whereas Byrne et al. (2014) mapped all classes of shortening landforms on all terrains at individual feature lengths as short as ~10 km.

Nonetheless, both sets of observations agree with the predicted roughly north–south orientation of thrust faults at low to mid latitudes predicted by stress models for a combination of tidal despinning and global contraction. Of note, Watters et al. (2015) suggested that the east–west thrust fault pattern they recognized at higher latitudes is consistent with the interpreted fault pattern of an equal contribution of stresses from despinning and contraction by Beuthe (2010). In contrast, the more complete assessment of stresses with failure criteria (Klimczak et al., 2015) revealed that the small variation in horizontal stresses at and near the poles arising from despinning permits the formation of a wide variety of thrust fault orientations at the polar regions (Figure 10.13), in agreement with the mapping by Byrne et al. (2014).

Neither the onset nor the duration of despinning has been well characterized to date (Chapter 4), and it may be that despinning was a sufficiently early and short-lived process either to have had no substantive effect on Mercury’s tectonic fabric or to have

overlapped not with global contraction but with a potential earlier phase of global expansion instead (Solomon and Chaiken, 1976; Chapter 19). Under such a scenario, the pattern of jointing predicted to have formed from despinning alone (Figure 10.12) would have further developed into graben and ultimately rift zones with those same orientations. Conversely, if tidal despinning did influence the development of global contraction-induced faults on Mercury, then either the despinning process began later and/or operated for longer than has been assumed before (e.g., Peale, 1988) or an early tectonic pattern generated long before global contraction-induced thrust faulting began somehow survived intense later volcanic resurfacing and impact bombardment (Section 10.8.1).

Importantly, this discussion is based on studies of the effect on Mercury’s tectonics of the deceleration by tidal forces of an initially faster rate of prograde rotation. However, a planetary body’s rotation rate can be altered by variations in orbital eccentricity (Correia and Laskar, 2004) as well as by momentum imparted by large impacts (e.g., Melosh, 1975; Lissauer, 1985; Wieczorek and Le Feuvre, 2009), such that the rate can either decrease or increase. On the basis of Mercury’s cratering record, Correia and Laskar (2012) and Wieczorek et al. (2012) found evidence that the planet may once have been in synchronous rotation before transitioning to its current 3:2 spin–orbit resonance as a result of spin-up by a large impact event. Moreover, if its spin rate following such an impact was greater than that of the 3:2 resonance, tidal forces may have decelerated the planet, whereas a lower post-impact spin rate could have been tidally accelerated to the 3:2 resonance during times of high orbital eccentricities (Wieczorek et al., 2012). And the Caloris impact event, which likely occurred at about the same time as the onset of global contraction (Section 10.8.1), probably increased Mercury’s rate of rotation (Wieczorek and Zuber, 2001) even to those of resonances higher than 4:1 (Wieczorek et al., 2012).

Conversely, Noyelles et al. (2014) argued that Mercury acquired its 3:2 spin–orbit resonance very early, over a time-scale of as short as 20 Myr and possibly as a homogeneous body that had yet to undergo core–mantle segregation (i.e., differentiation). Noyelles et al. (2014) also disputed the possibility that Mercury was ever in a synchronous rotation rate. Later, Knibbe and van Westrenen (2016) concluded that Mercury may have had one or more higher-order resonances prior to acquiring its present spin rate, with the secular evolution of its spin–orbit

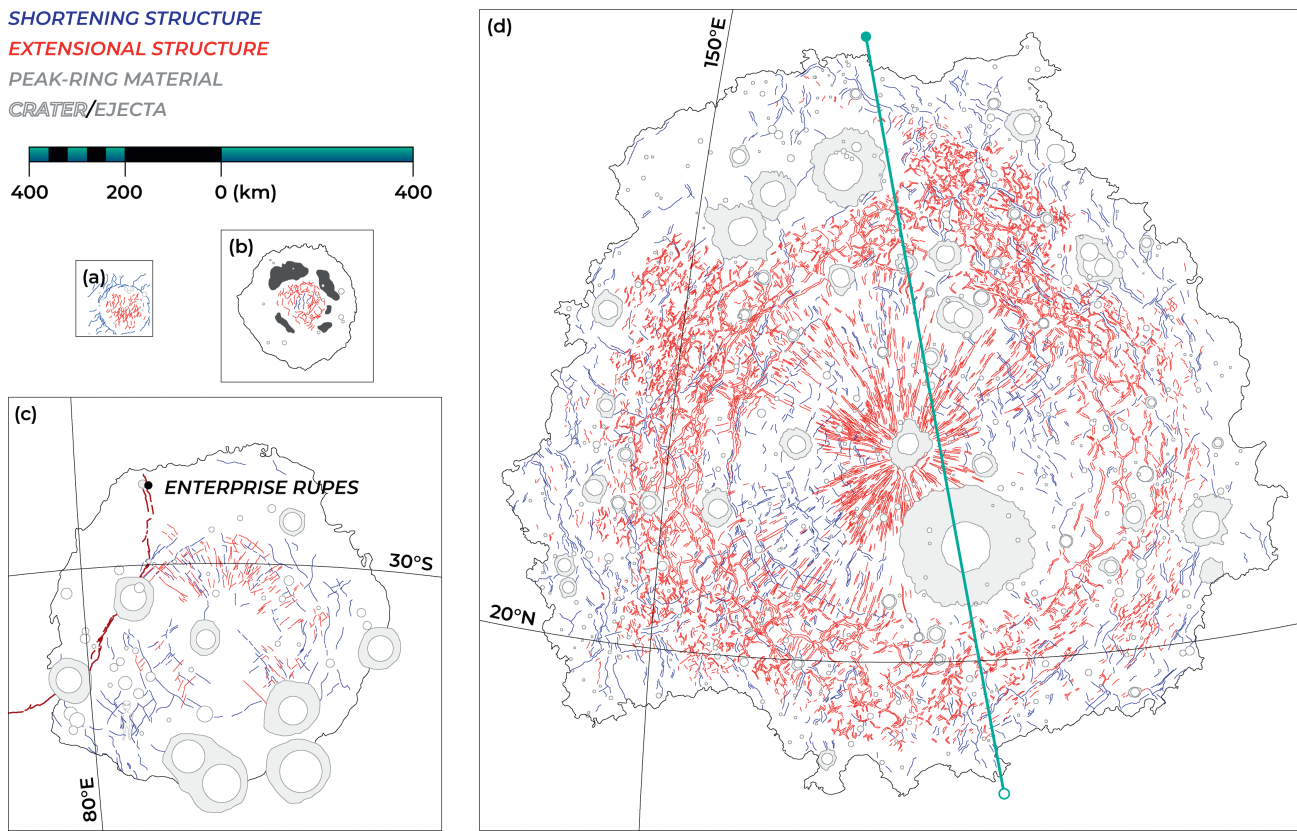


Figure 10.14. Extensional and shortening structures within flooded impact features. (a) An unnamed ghost crater in the NSP. (b) The Mozart basin. (c) The Rembrandt basin, the second-largest well-preserved impact structure on Mercury. (d) The Caloris basin, the largest well-preserved impact structure on the planet and host to one of the largest smooth plains deposits on Mercury. Extensional landforms are shown in red; shortening landforms are shown in blue. The teal line through the basin corresponds to the location of the topographic profile shown in Figure 10.9. Each impact structure is shown at the same scale. Azimuthal equidistant projections centered at: (a) 60.3°N, 36.7°E; (b) 7.8°N, 169.6°E; (c) 33.5°S, 88°E; and (d) 30°N, 161°E.

resonance a function of both its impact history and its chaotic orbital eccentricity (Correia and Laskar, 2009). Whatever the evolution of Mercury's spin rate, then, the possibility exists that the planet has been subject to accelerations in spin rate both positive and negative and more than once – and so models in which its shortening structures develop against a backdrop of simple tidal spindown have probably not explored sufficiently the complex interaction between tectonics and celestial mechanics. This interaction remains one of the outstanding questions in the temporal development of Mercury's tectonic structures (Section 10.10.1).

10.6.4 Basin Tectonics

As we have shown, the dominant form of tectonic deformation on Mercury involves shortening, and extensional tectonic features are almost entirely restricted to impact craters and basins that host volcanic smooth plains (Murchie et al., 2008; Watters et al., 2009a; Blair et al., 2013). However, extensional and shortening tectonic landforms within those impact features vary enormously in structural complexity – from sets of graben that describe polygonal patterns in craters tens of kilometers in diameter to collocated basin-radial, basin-circumferential, and

basin-oblique graben and shortening structures within the Caloris basin, which could reflect a combination of local- and global-scale processes.

To illustrate this increase in complexity with increasing crater diameter, we show in Figure 10.14 the *tectonic* map patterns of four exemplar volcanically infilled impact features on Mercury: a 100-km-diameter ghost crater (Figure 10.14a), the 240-km-diameter Mozart basin (Figure 10.14b), the Rembrandt basin, some 720 km in diameter (Figure 10.14c), and the titanic Caloris basin (Figure 10.14d).

Ghost craters are impact features that have been partially to entirely covered by lavas (Chapter 11). Where such burial is incomplete, these craters can still be recognized by their rims. Where burial is total, however, ghost craters are nearly always identified by tectonic landforms localized by the buried rim. For the example shown in Figure 10.14a, situated in the NSP, the buried crater rim is delineated by a ring of shortening structures ~100 km across (individual segments of this ring are several to tens of kilometers in length and hundreds of meters to kilometers in width, respectively). The interior of the crater has been deformed by a number of graben with no strongly preferred orientations; these structures are several kilometers long and hundreds of meters in rim-to-rim width. Notably, the

intersections of these graben render the interior crater fill as a set of polygonal blocks (Figure 10.9b). The graben extend from the crater center to ~80% of its radius. Shortening structures in the surrounding plains terminate at the crater's periphery and do not penetrate its interior. This structural arrangement is characteristic of graben-hosting ghost craters in general, which primarily occur in the NSP and circum-Caloris smooth plains (e.g., Klimeczak et al., 2012). Some variations can occur: in several instances, graben superpose the shortening structures that ring ghost craters, and in others it is only graben that delineate buried craters, with shortening structures entirely absent.

At a larger scale, several of Mercury's mid-sized basins feature both shortening and extensional landforms within their volcanic infill. For example, the Mozart basin contains both graben and shortening structures, although both types of tectonic deformation occur only in the area bounded by its peak ring (Blair et al., 2013) (Figure 10.14b). Basin-circumferential graben form an annulus spanning a distance of ~20–40% of the basin's radius from and concentric to its center; individually these structures measure kilometers to tens of kilometers in length and several hundred meters to about a kilometer in rim-to-rim width (Blair et al., 2013). From this annulus to the peak ring, located radially at about 50% of the basin's radius, graben are found in a mix of basin-radial, -circumferential, and -oblique orientations; these structures are kilometers long and hundreds of meters wide. Thrust-fault-related landforms, kilometers wide and tens of kilometers long, occur within the annular graben and show no preferred orientations. Tectonic structures of any kind are fewer in number in the southwestern sector of basin infill within Mozart's peak ring. Notably, this general pattern of deformation is also observed in the smooth plains units situated within the peak rings of the similarly sized Raditladi and Rachmaninoff basins (Blair et al., 2013).

The largest well-preserved impact feature in Mercury's southern hemisphere, Rembrandt basin, is riven along its northwestern interior by the northeast–southwest-trending, 820-km-long fault array termed Enterprise Rupes (Figure 10.14c). Apart from this enormous structure, however, the basin floor is heavily deformed by extensional and shortening structures (Watters et al., 2009b; Ferrari et al., 2015). Collocated basin-radial sets of graben and shortening structures form a fan-like pattern centered on the basin outward from around 20% of its radius, such that the radial graben in Rembrandt resemble a less-developed version of Pantheon Fossae in the center of the Caloris basin (Section 10.3). Both sets of radial structures in Rembrandt basin have similar dimensions, from tens of to about one hundred kilometers in length, and hundreds of meters in width. At a radial distance from the basin center of ~50% of the basin radius, these structures are spatially bound by circumferential thrust faults and graben of similar widths but shorter segment lengths. Local clusters of thrust-fault-related landforms without preferred orientations lie in the southwestern and eastern portions of the basin interior beyond about half the basin radius from its center (Ferrari et al., 2015); these structures are tens of kilometers long and ~1–2 km across.

The Caloris basin also hosts the greatest structural complexity on the planet (Figures 10.3a and 10.14d). The pronounced, basin-radial set of graben, Pantheon Fossae (Murchie et al., 2008), is the dominant tectonic assemblage in the basin,

originates from a point near the center, and extends to ~55% of the basin's radius. These graben range in length from ~5 km to 110 km and vary from ~1 km to 8 km in rim-to-rim width (Murchie et al., 2008). Pantheon Fossae is bound by circumferential graben that form a near-complete annulus from ~45% to 55% of the basin radius; this annulus is tens of kilometers across, but its constituent graben are hundreds of meters to a few kilometers wide. Its outward extension is manifest by basin-oblique graben that define a complex polygonal map pattern and steadily decrease in width, depth, and length toward the basin margin; near the basin periphery, these structures are but a few kilometers in length and several hundred meters wide. The most abundant types of shortening structures are basin-circumferential, and extend from close to the basin center to about 70% of its radius. Radially oriented thrust faults also occur within this zone but are less common than their basin-concentric counterparts. Beyond ~70% of the basin radius, thrust-fault-related landforms show no strongly preferred orientations and so also form a polygonal pattern that becomes less prominent toward the basin rim. There is less variation in size of the shortening structures in the Caloris basin, with most segments tens of kilometers long and up to several kilometers across.

Almost every tectonically deformed impact structure on Mercury is characterized by a scarcity of definitive crosscutting relations, challenging recognition of a developmental sequence for attendant structures (Section 10.8). Where shortening and extensional landforms spatially coincide within ghost craters, their superposition relations are often unclear (Watters et al., 2012); they do not coincide in Mozart at all (Blair et al., 2013). Graben appear to superpose, and thus postdate, thrust-fault-related structures in the Caloris and Rembrandt interior plains (e.g., Murchie et al., 2008; Ferrari et al., 2015; Cunje and Ghent, 2016), but no clear dip- or strike-slip offsets are observed in either basin.

However, finite-element modeling results for ghost craters (Freed et al., 2012) and mid-sized basins such as Mozart (Blair et al., 2013) provide some insight into the complex tectonic deformation recorded in Mercury's large, volcanically filled impact basins. For example, the thermal contraction of thick, rapidly emplaced lava flows (Chapter 11) produces horizontal tensile stresses that favor the formation of mixed-orientation joints which, if allowed to grow sufficiently, can develop into graben. This mechanism also plausibly accounts for the myriad graben and joints observed within both volcanic and impact melt deposits across Mercury (Section 10.3 and Figure 10.3a). Moreover, models of thermally contracting lavas show that a buried crater rim or ring serves to strongly concentrate radial tensile stresses in the overlying unit, thus facilitating the formation of circumferential graben (Blair et al., 2013). In contrast, some combination of shortening in response to cooling and contraction of the planet's interior and flexure due to vertical loading – as has been proposed for lavas inside the summit caldera complex of Mars' Olympus Mons volcano, for example (Zuber and Mousginis-Mark, 1992) – is likely responsible for the formation of thrust-fault-related landforms at a variety of scales on Mercury, including the shortening structures in volcanically infilled impact features (Watters et al., 2009b; Freed et al., 2012; Blair et al., 2013). The truncation of shortening landforms in the

NSP at the peripheries of thrust-bound ghost craters may reflect partitioning of shortening strain into existing structures, in effect shielding the (ghost) crater interior from a compressive stress state and so permitting the formation of joints and graben therein.

Earlier workers suggested that the prominent fossae within the Caloris basin may have formed as the surface expression of dike propagation (Head et al., 2008, 2009) – and indeed, this system of extension bears a resemblance to radial graben sets on Venus interpreted to be the result of upward flexure of magma chambers within mechanically layered lithospheres (Le Corvec et al., 2015). The strain associated with Pantheon Fossae, however, does not compare well with measured strains of radial dike systems on Earth (Klimczak et al., 2010). Other studies explored the idea that Pantheon Fossae may be the result of a bolide impact to the center of a flexurally uplifted basin center (Freed et al., 2009), with either the volcanic emplacement of the smooth plains exterior to the basin (Melosh and McKinnon, 1988; Kennedy et al., 2008) or the inward flow of the lower crust (Watters et al., 2005) responsible for that uplift. Of note, the radial graben of the Rembrandt interior plains are similar to those of the Caloris basin, but there are no extensive plains exterior to Rembrandt (Denevi et al., 2013), and the prospect of lower crustal or mantle flow operating within Mercury, particularly at scales below those of the diameter of the Caloris basin, is unlikely given the planet’s relatively thin silicate shell (Chapter 19). However, the strains represented by Pantheon Fossae correspond to an uplift on the order of 10 km (Klimczak et al., 2010), which is not observed for the Caloris basin, and so the means by which those fossae formed remains unknown.

In a manner similar to those within flooded craters and smaller basins, graben of mixed orientation in the Caloris and Rembrandt plains may reflect near-isotropic horizontal extension of rapidly emplaced lavas (Blair et al., 2013). Under this scenario, the shoaling of graben floors, and overall reduction in graben size, with increasing distance from basin center likely indicates corresponding reductions in plains thickness, and thus original basin depth, toward the rim (Freed et al., 2012; Klimczak et al., 2013a). Further, if the pronounced circumferential graben within both of these plains units reflect extension above a buried basin ring, then the impact structures in which they are hosted may be multi-ring basins – a class of impact feature not yet clearly documented for Mercury (Fassett et al., 2012).

Finally, although the shortening structures within these basins may reflect some amount of subsidence (e.g., Melosh and McKinnon, 1988), the extent to which this mechanism has operated is likely not substantial. Moreover, it may be difficult to differentiate crustal shortening as a result of volcanic loading from that caused by global contraction, especially given the pervasiveness and longevity of the latter process (Section 10.8.1). Indeed, there is evidence that shortening continued within the Caloris basin for some amount of geological time after its network of extensional structures formed (Section 10.8.2). Nonetheless, the differences in orientation of thrust faults in the Caloris and Rembrandt interior plains from basin-circumferential or -radial to -oblique could reflect a transition of the responsible stress field from strongly basin-shape-influenced to horizontally isotropic with increasing distance from the basin center.

10.7 OTHER DEFORMATIONAL PROCESSES

Although Mercury’s tectonic character has been dominated by global contraction, with a possible contribution from tidal despinning, studies of Mercury’s tectonic history have also considered other processes to help account for observations made first by Mariner 10 and later by MESSENGER. Such candidate processes include mantle convection (Section 10.7.1), lithospheric folding (Section 10.7.2), planetary reorientation by processes internal and/or external to Mercury (Section 10.7.3), and some combination thereof. Several of these mechanisms were suggested before MESSENGER observations of the innermost planet, however, and as a result are less tractable today than when first proposed. Nonetheless, some of the processes discussed below may have contributed at least in part to the present-day tectonic character of Mercury.

10.7.1 Mantle Convection

Convective motion within Mercury’s silicate shell has been suggested as a means to control or at least influence tectonic deformation. For example, Watters et al. (2004) proposed that mantle downwelling might thicken Mercury’s crust and so localize compression in a manner similar to intraplate downwelling on Earth (Neil and Houseman, 1999). In addition, from three-dimensional numerical simulations of mantle convection within Mercury, King (2008) had suggested that the linear roll structures in his models might concentrate the roughly north-south-oriented shortening strains at low latitudes mapped with Mariner 10 data (Watters et al., 2004) (Section 10.2.2).

Mantle downwelling as a mechanism for developing elongate zones of crustal shortening, however, must be reconciled with indications from MESSENGER that the thickness of Mercury’s silicate shell is substantially less than values accepted earlier. The simulations of King (2008), for instance, incorporated a mantle thickness of 600 km, whereas MESSENGER measurements of Mercury’s gravity field, together with determinations of the planet’s obliquity and libration amplitude, place the core–mantle boundary at a depth of about 420 km (Hauck et al., 2013). Although recent thermal evolution models with a core–mantle boundary at this depth are permissive of convection in Mercury’s mantle (Michel et al., 2013; Tosi et al., 2013), and convection continues to the present for a subset of these models, this process would likely occur as discrete cells of up- and downwelling having horizontal dimensions comparable with the thickness of the mantle rather than as long rolls (Chapter 19).

Therefore, although it is possible that mantle downwelling has played some role in the localization of shortening strains on Mercury’s surface, this process was likely not responsible for the apparent roughly north-south fabric identified in the mapping of the planet’s thrust-fault-related landforms (Byrne et al., 2014; Watters et al., 2015) – if indeed this pattern is real in the first place and not a function of a lighting bias. On the other hand, mantle up- and downwelling may have contributed to regional variations in crustal thickness, which in turn could influence the surface manifestation of shortening strains on

Mercury. Yet because the vigor and longevity of the convection of Mercury's mantle is sensitive to a range of parameters and conditions (e.g., the possibility of compositional stratification or lateral heterogeneity) that are not yet fully characterized (Chapter 19), the contribution of mantle convection to near-surface compressive stresses, and so to the formation, distribution, and orientation of Mercury's shortening structures, is uncertain.

10.7.2 Lithospheric Folding

The process or set of processes that has substantially modified Mercury's topography at large length scales has yet to be determined, although the origin of these undulations is addressed in more detail in Chapter 3. Nonetheless, where they are collated, tectonics may provide some insight into the nature and origin of Mercury's anomalous topographic lows and highs.

For example, high values of admittance (i.e., the ratio of gravity to topography in the wavenumber domain) at low spherical harmonic degree and order indicate that the topographic rise within the NSP is either supported by buoyancy near the base of the mantle or elastically supported by lithospheric strength (James et al., 2014). This latter scenario predicts compression centered at the rise and extension at its periphery. Yet the areal density of mapped shortening structures (Byrne et al., 2014) (Figure 10.3a), if a proxy for horizontal strain across the NSP, shows no greater density of structures on the long-wavelength northern rise than in the surrounding plains (James et al., 2014). For the lithosphere to have supported the rise, it would have to have a thickness of more than 100 km since the time that the rise was formed (James et al., 2014).

It has also been proposed that mantle dynamic processes might result in long-wavelength modification to Mercury's topography (King, 2008). To first order, the linear undulations within and adjacent to the Caloris basin, for example, are consistent with the long roll-like convection patterns predicted by some three-dimensional models of convection within Mercury's mantle (King, 2008). As noted above, however, convection cells within Mercury are not likely to follow such a pattern (Chapter 19), and the amplitude of dynamic topography predicted by convection models that display these patterns is one to two orders of magnitude (King, 2008) below that of the observed undulations (Klimczak et al., 2013a) (Section 10.4).

The long-wavelength warps may be a manifestation of Mercury's global contraction that formed as a result of lithospheric buckling or folding (Dombard et al., 2001; Hauck et al., 2004; Solomon et al., 2012). Although calculated elastic buckling stresses far exceed the strength of the lithosphere, models simulating elastic-plastic behavior of the lithosphere allow for folding much below the expected threshold of elastic buckling stresses (McAdoo and Sandwell, 1985). In an effort to reconcile estimates of planetary radius change from earlier, incomplete mapping studies with those predicted from thermal evolution models (Section 10.6.1), Dombard et al. (2001) explored the possibility that hidden shortening strain was manifest on Mercury in the form of long-wavelength, low-amplitude folding.

When Dombard et al. (2001) conducted their study there was no evidence that such folding existed on Mercury. The dimensions of

the long-wavelength undulations that were ultimately discovered on the planet yield shortening strains ϵ of only $\sim 10^{-5}$ (Section 10.4), far less than those of brittle structures and so representing an extremely small contribution to Mercury's decrease in radius. Even so, Dombard et al. (2001) found that in a model of unstable deformation of a strong surface layer (Fletcher and Hallet, 1983), adjusted for folding, long-wavelength changes in topography did develop in response to global contraction-induced crustal shortening at wavelengths comparable with those measured on Mercury. If related to global contraction, these undulations may correspond to the long-abandoned geosyncline and geanticline hypothesis for Earth, developed when the tectonics of our own world was thought to be dominated by vertical crustal motion driven by global contraction (Élie de Beaumont, 1852; Dana, 1873).

10.7.3 Planetary Reorientation

A body in which mass is unequally distributed may undergo reorientation so that its axis of greatest moment of inertia aligns with its spin axis. This reorientation can yield stresses sufficient to fracture the body's outer rigid shell, with the resultant strain recorded as tectonic landforms (e.g., Melosh, 1977), both extensional and shortening in nature. Polar wander on Earth can be driven by changes in mass distribution from plate motions (e.g., Duncan and Richards, 1991), but on one-plate planetary bodies polar wander may arise from surface loading (as with the Tharsis Rise on Mars: Melosh, 1980; Zuber and Smith, 1997; Zhong, 2009) as well as from variations in interior density (Nimmo and Pappalardo, 2006) or thermal structure (Roberts and Nimmo, 2008).

Beyond inducing changes in spin rate (Section 10.6.3), large impacts can also drive changes in mass distribution (Nimmo and Matsuyama, 2007; Karimi and Dombard, 2014; Matsuyama et al., 2014) and thus may also force the reorientation of one-plate bodies. This mechanism has been proposed for numerous bodies in the solar system: for example, the Moon (Wieczorek and Le Feuvre, 2009), Mars (Kuang et al., 2014), and Uranus (Morbidelli et al., 2012) may all have experienced substantial reorientation from large hypervelocity impacts. At the greatest scales, such collisions have been invoked to account for the formation of the Moon (e.g., Asphaug, 2014) and the large mass fraction of Mercury's core (e.g., Benz et al., 1988; Chapter 18).

The prospect of planetary reorientation influenced by the gravity anomaly associated with the Caloris basin was investigated by Matsuyama and Nimmo (2009). These authors suggested that a combination of despinning, reorientation, and global contraction generated a stress field consistent with Mariner 10 observations of Mercury's tectonics. However, this predicted stress field does not compare as well with MESSENGER-derived mapping observations, and the relative timing of despinning, contraction, and reorientation (should it have occurred) is as yet poorly characterized (Section 10.6.3).

Interestingly, the NSP on Mercury occupy a broad region of low gravitational potential and thin crust and are so termed because these plains occur at and near the planet's present north pole. Although there is no morphological evidence that

points to a single, giant basin in which these plains lie (Head et al., 2011), polar flattening is about the same at both poles (Chapter 3), and there is no southern counterpart to the ~1–2-km-thick NSP. If the northern gravity low and corresponding thin crust correspond to an ancient basin for which surficial evidence no longer survives, then this basin may have caused Mercury to reorient early in its history. Nonetheless, at present the largest impact basin recognized on Mercury is Caloris, and the effects of any early global-scale tectonic process may well have been overprinted by the global contraction that followed (Section 10.6.3).

10.8 TIMING OF DEFORMATION

A full characterization of Mercury’s tectonics cannot be complete without an understanding of the planet’s history of deformation. Chief among the means we can use to establish this history is the law of superposition, by which the uppermost unit of a geological sequence is interpreted as the youngest, and vice versa. This approach has been refined for Earth over the past several centuries and generally works well in the mapping of geological units on other worlds. However, unlike temporally discrete events such as bolide strikes or volcanic eruptions, faults can be reactivated or can accommodate sustained slip over time, making it far more difficult to place the initiation or cessation of faulting into a stratigraphic column. To that end, remotely sensed observations of a fault superposing a given geological unit indicate that the *most recent* tectonic activity occurred after the unit was emplaced, but tell us nothing of when the fault first formed. Nonetheless, superposition relations between faults and their related landforms and Mercury’s geological units, together with crater areal density measurements (Chapter 9), give us a first-order insight into the tectonic evolution of the innermost planet.

Here, we review first the evidence for when shortening deformation occurred on Mercury (Section 10.8.1). In Section 10.8.2, we do the same for extensional deformation. In Section 10.8.3, we discuss the likely timing of the long-wavelength modifications of Mercury’s topography. We finish with an assessment of the implications of these findings for understanding the planet’s thermal history (Section 10.8.4).

10.8.1 Shortening Deformation

Observations from MESSENGER data indicate that thrust-fault-related landforms interpreted to have formed from global contraction deform all major surface units present on Mercury, which broadly places the relative timing of deformation by these landforms as having continued at least until after the emplacement of the units they superpose. Thrust-fault-related landforms are abundant in Mercury’s older intercrater terrain (e.g., Byrne et al., 2014; Chapter 6), but they also deform the younger smooth plains units (e.g., Watters et al., 2009b; Byrne et al., 2014; Ferrari et al., 2015) (Figure 10.3a). With the exception of a single, ambiguous superposition relationship (Watters et al., 2009a), the lack of embayment relations between thrust faults and plains units has been taken as evidence that the bulk of global contraction-induced deformation did not occur until the

youngest major plains units were in place (e.g., Strom et al., 1975; Melosh and McKinnon, 1988; Spudis and Guest, 1988; Solomon et al., 2008; Banks et al., 2015). Absolute model ages derived from crater size–frequency distribution (SFD) measurements indicate that the emplacement of the youngest expanses of smooth plains units was largely complete by about 3.5 Ga (Strom et al., 2008, 2011; Fassett et al., 2009; Head et al., 2011; Denevi et al., 2013; Marchi et al., 2013; Ferrari et al., 2015; Ostrach et al., 2015; Byrne et al., 2016b; see also Chapters 6, 9, and 11), which therefore indirectly signifies the point after which the majority of shortening strain was accommodated on Mercury.

This finding is borne out by the results of several regional studies. For example, through mapping shortening structures and other lineations in Apārangi Planitia, situated at low latitudes in Mercury’s eastern hemisphere, López et al. (2015) identified two stages of deformation. These authors interpreted low-relief thrust-fault-related landforms to have formed prior to the emplacement of the smooth plains units in the region; these smooth plains were emplaced at around 3.7 Ga (Byrne et al., 2016b). In contrast, a set of topographically more pronounced thrust-fault-related landforms was inferred by López et al. (2015) to have formed entirely after the emplacement of the units they deform. The orientation of this set was also found to be strain incompatible with, and so must have formed at a different time than, the low-relief landforms. Crosscutting relations and crater SFD measurements of the Rembrandt impact basin, its interior fill, and the Enterprise Rupes thrust fault system (Figure 10.14c) gave model ages for major tectonic activity along the system of between 3.8 and 3.6 Ga (Ferrari et al., 2015). And Giacomini et al. (2015) found, with SFD-derived model ages, that activity along Blossom Rupes occurred at around 3.7–3.5 Ga.

Although crater statistics can provide a general overview of the timing of shortening in a given region affected by thrust faulting, superposition relationships of thrust-fault-related landforms with individual impact craters can contribute toward a planet-wide understanding of the onset and duration of global contraction-induced thrust faulting (Banks et al., 2015). The state of degradation of a crater can be linked to one of Mercury’s time–stratigraphic periods (e.g., Pohn and Offield, 1970; Trask, 1971, 1975; Moore et al., 1980) that, from oldest to youngest, include pre-Tolstojan, Tolstojan, Calorian, Mansurian, and Kuiperian (Chapter 6). Although qualitative, some age information can be gleaned regarding the relative timing of thrust faulting at a given location if a crater for which degradation state can be determined superposes, or is superposed by, a shortening structure.

For example, Banks et al. (2015) found that of a number of craters with degradation states consistent with the pre-Tolstojan and Tolstojan periods are all crosscut by shortening landforms, indicating that the thrust faulting visible today postdates the formation of these craters. Of the craters with degradation states consistent with the Calorian period that these authors investigated, the majority had been deformed by thrust faults. However, a few of the craters determined to be of this period do not appear to be deformed by the thrusts they superpose (Figure 10.15). Under the assumption that these shortening landforms are the result of global contraction, this process was



Figure 10.15. A 200-km-long unnamed thrust-fault-related landform (white arrows) superposed by a heavily degraded 130-km-diameter Calorian crater (black arrow). Note that the crater's ejecta superposes and mutes the surface expression of the proximal portion of the thrust fault. The image is a mosaic composed of MESSENGER images EN0220316553, EN0220319665, EN0220321873, EN0220404657, EN0220407308, EN0220490886, and EN0220493578. Azimuthal equidistant projection, centered at 42.0°S, 19.0°E.



Figure 10.16. The 51-km-diameter Mansurian crater Martial, which is crosscut by an unnamed thrust-fault-related landform (white arrows). The image is a portion of MESSENGER image EW0213416030G. Azimuthal equidistant projection, centered at 68.0°N, 182.0°E.

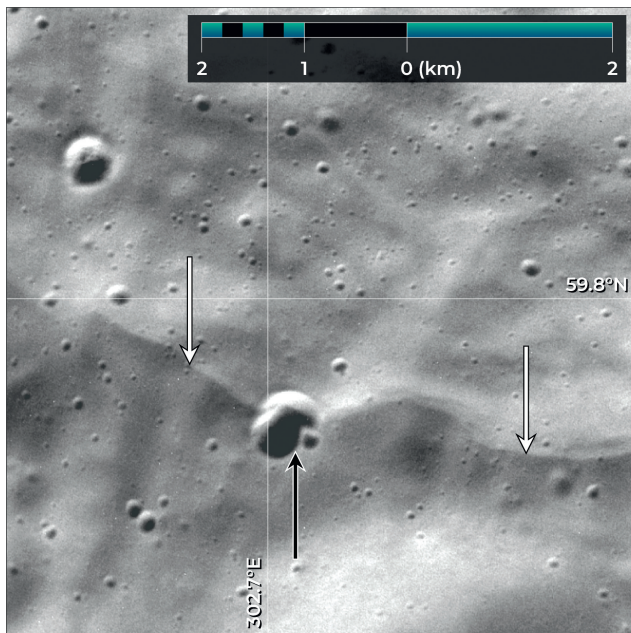


Figure 10.17. A small thrust-fault-related landform (white arrows) appearing to crosscut a relatively fresh 500-m-diameter crater (black arrow). This thrust is adjacent to, and has the same strike as, Carnegie Rupes (Figure 10.1c). The image is a portion of MESSENGER image EN1036136378M. Azimuthal equidistant projection, centered at 59.8°N, 302.7°E.

underway during or even prior to the Calorian – which, in turn, implies at least some overlap between the waning phase of flood basalt emplacement and global contraction.

Banks et al. (2015) also assessed superposition relations between thrust faults and craters for which degradation states correspond to the Mansurian period, and they found that a majority of these craters are undeformed. Yet a few such craters *are* deformed (Figure 10.16), indicating that global contraction continued to drive thrust faulting during this period. Of note, none of the Kuiperian craters investigated by Banks et al. (2015) was found to be unequivocally deformed by thrusts – although these authors identified other evidence that crustal shortening continued into the Kuiperian.

This evidence is manifest in part as a population of small monoclines, at least an order of magnitude smaller than those previously recognized, some of which crosscut craters only 1–2 km in diameter for which the state of degradation (or lack thereof) implies that they correspond to the Kuiperian period (Figure 10.17). These small shortening landforms are typically only tens of meters in relief and but a few kilometers in length (Watters et al., 2016). Although several of these small structures superpose craters, the rarity of this type of crosscutting relationship is likely a function of monocline size and the relatively low cratering rate in the Kuiperian. In addition, narrow graben have been identified along the crests of larger shortening structures (Section 10.2.1) (Figure 10.18); these extensional landforms are consistent with the interpretation of Mercury's thrust-fault-related landforms as fault displacement-gradient folds (Wickham, 1995), with the graben corresponding to outer-arc extension along the fold hinge axes

(Section 10.2.1). In any case, given assumed cratering rates on Mercury (Le Feuvre and Wieczorek, 2011; Marchi et al., 2013), landform degradation even in the Kuiperian is expected to be geologically rapid, such that small shortening and extensional structures are not likely to survive for extended periods of time (Watters et al., 2016). That these landforms are visible today therefore indicates that thrust faulting has operated on Mercury into the geologically recent. To date, there is no evident explanation for why new structures should form from global contraction when a worldwide network of faults was already present. Nonetheless, that global contraction

continues today is not surprising, since the presence of a magnetic field at Mercury and the amplitude of the planet's forced libration (Chapter 4) indicate that its outer core is still molten and so the planet must continue to experience secular cooling.

Taken together, these observations show that globally distributed thrust faulting was underway during or at the end of the Calorian period and continued into the Kuiperian. Importantly, we cannot ascertain with certainty whether thrust faulting commenced in the Calorian or instead craters formed in this period were deformed by thrusts that were already there and simply experienced slip events subsequent to impact. Given that the oldest surface units on Mercury date to ~ 4.1 Ga (Marchi et al., 2013; Chapter 9), it may be that earlier volcanism and impact bombardment removed entirely any pre-Tolstoian or Tolstoian shortening structures. If so, then those superposed by Calorian craters are representative of the oldest population of preserved thrust-fault-related landforms on the planet.

Even so, a rock-mechanical assessment of the brittle strength of Mercury's lithosphere suggests that an appreciable amount of radial decrease – between 400 m and 2.1 km – is necessary before stresses become sufficiently large to overcome frictional resistance to sliding along pre-existing discontinuities in the lithosphere (Klimczak, 2015) (Section 10.6.1 and Figure 10.19). This finding requires that some considerable time must have passed between the start of secular cooling and the formation of shortening landforms, indicating that even the earliest reliable evidence of thrust faulting in the Calorian must postdate the onset of global contraction. Moreover, the calculated reduction in Mercury's radius of up to 2.1 km necessary to trigger slip along thrust faults also implies that the rate of global contraction was likely greater early in the planet's geological history (Klimczak, 2015) and, for a radius change of 3.1–7.1 km since the Calorian (Table 10.1), must have continued at a very slow average rate of radius reduction of $(1.1\text{--}2.5) \times 10^{-20} \text{ s}^{-1}$ ($1.1\text{--}2.5 \mu\text{m}$ per Earth year) after thrust faulting began (Figure 10.19).



Figure 10.18. A set of small, sub-parallel graben along the crest of Calypso Rupes (white arrows). The image is a mosaic composed of MESSENGER images EN0249987811M and EN0250016605M. Azimuthal equidistant projection, centered at 19.6°N , 45.7°E .

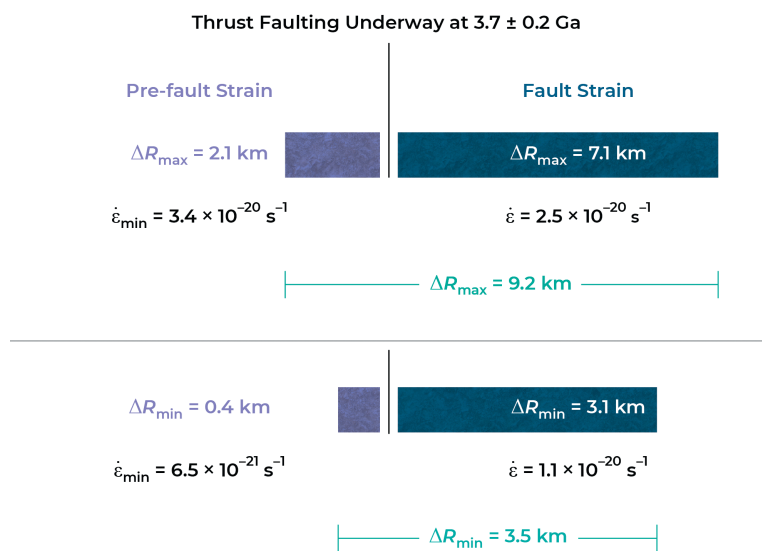


Figure 10.19. Maximum and minimum amounts of total radius change ΔR from the different components of global contraction. Mercury's lithosphere accommodated a change in radius prior to, as well as after, the onset of thrust faulting. The resultant rates of contractional strain, $\dot{\varepsilon}$, are given for a scenario under which brittle failure was underway by 3.7 ± 0.2 Ga.

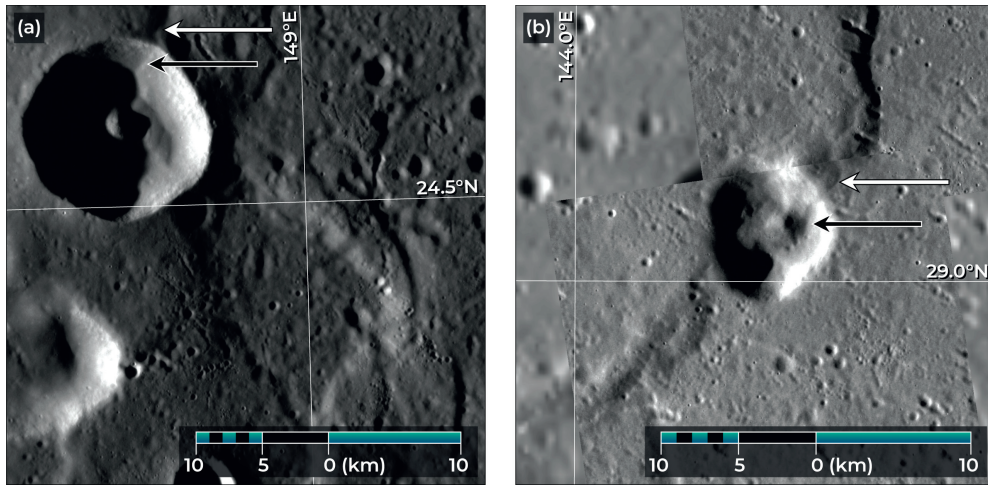


Figure 10.20. Examples of craters within the Caloris basin that have been modified by thrust faulting. (a) An unnamed crater 14 km in diameter, the northeastern portion of which is crosscut (black arrow) by a thrust-fault-related landform (white arrow). The image is a portion of MESSENGER image EN1015368165M. (b) Another unnamed crater, 8 km in diameter, cut (black arrow) by a northeast–southwest-trending shortening structure (white arrow). The image is a mosaic composed of MESSENGER images EN0250998103M and EN0251055707M. Azimuthal equidistant projections, centered at 24.5°N, 145.0°E and 29.0°N, 144.5°E, respectively.

10.8.2 Extensional Deformation

Where they are observed, joints and graben on Mercury are thought to represent the effects of cooling and thermal contraction of the units in which they are found (e.g., Freed et al., 2012; Klimczak et al., 2012; Watters et al., 2012; Blair et al., 2013) (Section 10.6.4). Given that the timescales over which these lavas (and impact melt) would likely have cooled (Freed et al., 2012), these fractures must therefore have formed soon after the emplacement of their host rocks. If so, then the joints that have so far been recognized in impact melt deposits on the floors of relatively well-preserved impact features, such as Hokusai, Abedin, or Degas craters (Figure 10.9c), must themselves be relatively young.

Crosscutting relations between extensional tectonic features and impact craters support this interpretation. For example, the graben identified in the NSP, which are located exclusively within ghost craters (e.g., Klimczak et al., 2012; Figures 10.3a and 10.9b), do not appear to modify any superposing craters, consistent with the inference that these structures formed soon after their host rocks were emplaced. Absolute model ages for the NSP are ~3.7–3.9 Gyr (Head et al., 2011; Denevi et al., 2013; Marchi et al., 2013; Ostrach et al., 2015), a range of ages that must therefore also correspond to the formation times of these graben. Likewise, the graben in the Caloris basin do not superpose any of the craters on those plains (Klimczak et al., 2013a), and so they must be approximately the same age as those ~3.7–3.9-Gyr-old basalts (Strom et al., 2008, 2011; Fassett et al., 2009; Denevi et al., 2013; Marchi et al., 2013). The graben mapped within the Rachmaninoff, Raditladi, and Mozart basins (e.g., Figure 10.14b) are therefore also about the same age as their volcanic host rocks (e.g., Blair et al., 2013). Interestingly, the lavas within the inner peak ring of the Raditladi basin may be as young as about 1 Gyr (Prockter et al., 2010); if so, so too are the graben therein.

The Rembrandt and Caloris interior plains units boast a complex history of deformation (Figures 10.14c, 10.14d, and Section 10.6.4), and in numerous instances, even where tectonic structures crosscut one another, timing relations are ambiguous. Nevertheless, Cunje and Ghent (2016) compiled a series of relative timing relationships for several examples of graben-shortening-landform intersections in the Caloris basin. These authors found that tectonic deformation of these plains began with the formation of shortening structures, which then partially overlapped with the development of basin-radial graben (i.e., Pantheon Fossae) (Sections 10.3 and 10.6.4). Some time thereafter, when thrust faulting within the plains ceased but the radial graben were still forming, basin-concentric graben developed.

However, although neither basin-concentric nor basin-radial graben modify any craters (e.g., Klimczak et al., 2013a), several craters have been deformed by thrust-fault-related landforms (Figure 10.20). This observation does not necessarily require that shortening entirely postdated extension in the Caloris basin; instead, whatever mechanism was responsible for initiating thrust faulting may have been superseded by global contraction after basin-scale processes were complete. If so, then the uncertainty regarding the sequence of deformation within the Caloris basin illustrates once more that fault reactivation can frustrate efforts to determine a definitive geological history for a heavily deformed region.

10.8.3 Long-Wavelength Deformation

One of the key arguments against Mercury's long-wavelength undulations being constructional (i.e., volcanic) in origin is the presence of superposed craters with once-level floors that are now tilted in direction and slope comparable with the local topography of the undulations (Section 10.4). This observation also provides some insight into the timing of this enigmatic modification to Mercury's topography. For example, in the

Caloris basin there are many tilted craters that superpose but are not crosscut either by extensional or shortening tectonic landforms (Klimczak et al., 2013a). Given the density of structures within the plains (Figure 10.14d), and therefore the likelihood of one type of landform crossing another, it follows then that the modification to topography here occurred after plains emplacement and the formation of most, if not all, brittle tectonic structures.

This inference is supported by the pattern of tectonic deformation in the Caloris basin (Section 10.6.4 and Figure 10.14), which is profoundly influenced by the near-circularity of the basin shape. Even though the northern portion of the Caloris basin interior rises more than 1000 m above the northern basin rim, the circular arrangement of ridges and graben neither there nor in the southern portion shows any influence from this elevated topography. In contrast, for example, there is a systematic pattern of radial and concentric faults centered on (and that characterize) domical rises associated with magma chamber tumescence (Marti et al., 1994; Walter and Troll, 2001). This apparent lack of influence of the elevated topography on the orientations of graben and ridges is consistent with the inference that the brittle tectonic deformation in this area occurred prior to the establishment of the regional (warped) topography.

Moreover, the degradation states of those craters that are tilted within the Caloris basin suggest that they were formed well after the Calorian period; accordingly, the long-wavelength undulations developed relatively late in Mercury's geological history (Balcerski et al., 2013). For example, the floor of the Atget crater, a morphologically fresh impact structure within the basin, shows substantial deviation from horizontal (Figure 10.10). Craters with such degradation states are thought to correspond to the Mansurian period, which requires that the long-wavelength modification to the Caloris basin occurred in (or after) that same period.

Similarly, the northern rise hosts ghost craters with floors that tilt systematically away from the topographic high (Section 10.4), but craters superposing the rise that are not volcanically filled show less or no correlation in floor tilt with the long-wavelength topography (Klimczak et al., 2012; Balcerski et al., 2012). Modification of the region's topography thus began after plains emplacement and continued for some time thereafter, slowing and then ceasing as fresh craters continued to accumulate (Balcerski et al., 2013). Notably, some of the tilted but unfilled craters superpose, but are not modified by, tectonic landforms (both shortening and extensional), indicating that the growth of the undulation continued to times later than the periods of crustal shortening and thermal contraction of the NSP lavas. And since the amplitudes of the rises within Mercury's valles far exceed the local downhill gradient, the modification in these locations of long-wavelength topography must have occurred after the valles were formed and so, again, were not constructional in origin (Byrne et al., 2013b).

10.8.4 Implications for Mercury's Thermal History

The thermal history and evolution of Mercury must satisfy a number of geological constraints that are informed by the observations described in this chapter (and summarized in

Figure 10.19) and elsewhere in this volume (Chapter 19). For example, the total decrease in the radius of Mercury from secular cooling since the LHB amounts to 3.5–9.2 km and consists of two components. The first includes a 3.1–7.1 km radius change accommodated by thrust faulting (Byrne et al., 2014), and the second component accounts for 0.4–2.1 km of radius change (Klimczak, 2015) (Section 10.6.1) accommodated elastically and occurring sometime during or before the Calorian period, generally before the onset of thrust faulting (Banks et al., 2015).

A change in planetary radius of 3.1 to 7.1 km since the onset of widespread thrust faulting requires an average rate of radius reduction of $(1.1\text{--}2.5) \times 10^{-20} \text{ s}^{-1}$ throughout Mercury's geological past. The radius change calculated to have occurred prior to the start of thrust faulting (averaged over the entire geological history of Mercury prior to the Calorian period) yields a minimum contraction rate of $6.5 \times 10^{-21} \text{ s}^{-1}$ to $3.4 \times 10^{-20} \text{ s}^{-1}$. If global contraction commenced a few hundred million years after Mercury's formation, however, as the majority of thermal models predict, then values for the initial contraction rate would have been considerably greater, exceeding the average rate of contraction since the formation of thrust faults. To first order, this finding indicates that the rate of Mercury's global contraction has slowed over time.

10.9 TECTONISM AND VOLCANISM

In addition to tectonic activity, volcanism is a major planetary process that has shaped the surfaces of numerous solar system bodies, including the Moon, Mars, Venus, Io, and our own world. Mercury, too, records a detailed history of volcanic activity, albeit one largely constrained to the first ~20% of the planet's history (Chapters 6 and 11). As with those other bodies, the histories of volcanism and tectonic deformation on Mercury are intertwined – yet perhaps one is controlled by the other more so there than anywhere else in the solar system. In this section, we first review the prospect for widespread effusive volcanism on a planet undergoing global contraction (Section 10.9.1), and then appraise the utility of faults as conduits for the ascent of magma (Section 10.9.2).

10.9.1 Flood Volcanism on a Contracting Planet

Under a tectonic regime dominated by global contraction, the least compressive stresses act vertically and are governed by the overburden (the weight of the overlying rock volume: Section 10.5.1); the greatest compressive stresses act in the horizontal plane. Such a stress field is compatible with the formation of thrust faults, but also inhibits the vertical ascent of magma (e.g., Glazner, 1991; Hamilton, 1995; Watanabe et al., 1999), which is much more likely to propagate laterally. This stress state is thus not readily conducive to widespread effusive volcanism (e.g., Solomon, 1978; Marrett and Emmerman, 1992), and so volcanic flooding is not expected to occur after the onset of global contraction (Byrne et al., 2016b). An obvious inference, then, is that the volcanic smooth plains units on Mercury must have been mostly emplaced prior to the onset of global contraction.

Thrust fault activity has been found to have temporally overlapped, at least to some extent, with the emplacement of some of the relatively late flood lavas (Banks et al., 2015) (Section 10.8). Nonetheless, it has long been noted that many volcanic smooth plains deposits on Mercury are situated within older impact basins, including Caloris Planitia and those volcanic units in Beethoven, Rembrandt, and Tolstoj basins (e.g., Strom et al., 1975; Fassett et al., 2012). Many smaller deposits across the planet (Denevi et al., 2013), at least some of which are likely volcanic (Prockter et al., 2010; Marchi et al., 2011), are similarly situated in older impact craters.

This collocation of many of the youngest effusive volcanic units on Mercury with impact structures is consistent with predictions for a planet undergoing contraction from secular interior cooling (Solomon, 1978). The impact process removes overburden, resets prevailing stresses, and either entirely destroys (and thus forms anew) the pre-existing lithosphere or substantially fractures and weakens it, so that conditions amenable to magma ascent are in place locally. A large impact also converts kinetic energy to heat in the crust and mantle that may trigger or enhance the production of partial melt, even some time after the impact event (Roberts and Barnouin, 2012; Chapter 19). Impact structures are likely therefore to be prime (if not necessarily the *only*) sites for late-stage effusive volcanic eruptions under a tectonic regime otherwise generally unfavorable to extrusive activity.

10.9.2 Tectonic Structures as Magma Conduits

Despite its anticipated effects on effusive volcanism, global contraction has not prevented explosive volcanic activity on Mercury. Irregular depressions that lack raised rims, are morphologically dissimilar to impact craters, and are often surrounded by diffuse high-reflectance deposits have been interpreted as volcanic vents that have served as sites of explosive eruptions (Head et al., 2008; Kerber et al., 2009, 2011; Goudge et al., 2014; Thomas et al., 2014) (Section 11.2). Several of these vents superpose and thus postdate Caloris Planitia (Head et al., 2008), and at least one example (that which cuts the wall terraces within the 26-km-diameter Kuniyoshi crater) may be as young as ~1 Gyr (Thomas et al., 2014). Volatiles provide the primary driving force for explosive volcanic eruptions (e.g., Cashman, 2004), and volatile-rich melts are more buoyant and therefore more capable of ascent and eruption than effusive magmas of otherwise comparable composition.

The majority of pyroclastic deposits on Mercury are collocated with sites of pre-existing weakness in the lithosphere (Chapters 11 and 19) (Figure 10.21), including the heavily fractured central peaks, peak rings, and rims of impact craters and along the traces of thrust-fault-related landforms (e.g., Kerber et al., 2011; Klimczak et al., 2013a; Goudge et al., 2014; Habermann and Klimczak, 2015). Given that global contraction was at least underway in the Calorian period, explosive volcanism on Mercury has also operated under a regime of global contraction. This stress state therefore accounts for the spatial association between sites of

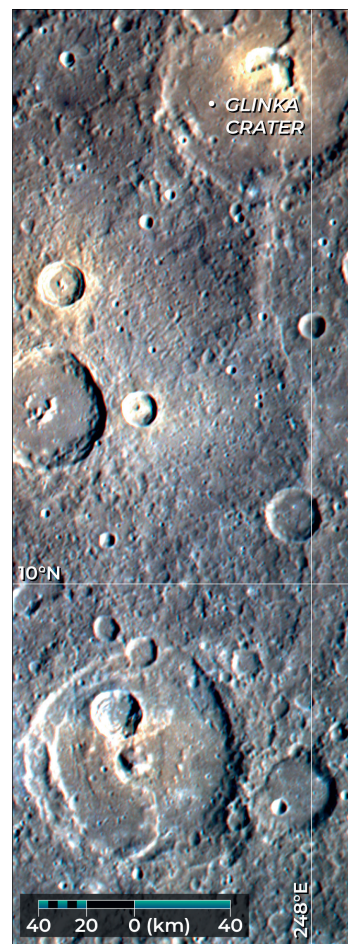


Figure 10.21. A group of north-south-trending thrust-fault-related landforms that crosscut craters, including the 89-km-diameter Glinka “pit-floor crater” in the upper part of this image. The pit inside Glinka is surrounded by a relatively bright “halo,” interpreted to be a pyroclastic deposit. The crater in the lower part of the image is that shown in Figure 10.7. The image is a three-color mosaic composed of MESSENGER images EW0242128483G, EW0242128487F, and EW0242128491I; red: 996-nm, green: 749-nm, and blue: 433-nm wavelength. Azimuthal equidistant projection, centered at 11.0°N, 248.0°E.

pyroclastic activity and faults and fractures that, especially if critically stressed, may have acted as conduits for the upward migration of volatile-rich magmas (Klimczak et al., 2013b) (Section 11.7).

Accordingly, that few to no pyroclastic vents have been observed in smooth plains units, e.g., in the NSP, suggests that there are no deep-seated faults in such locations along which volatile-rich magma can ascend. There are, however, several vents and pyroclastic deposits along the interior margin of the Caloris basin, and a few large vents are present on the margins of the smooth plains within the Tolstoj and Rembrandt basins. The presence and spatial distribution of these vents may reflect a stress state favorable to magma ascent and eruption similar to that calculated for regions at or near the rims of large mare-filled basins on the Moon (McGovern and Litherland, 2011).

10.10 FURTHER WORK

Despite providing a remarkable advance in our understanding of Mercury's tectonic character and history, the results of the MESSENGER mission challenge us to ask yet more questions about the innermost planet. Here, we discuss briefly some of those questions, and why it is important to resolve them (Section 10.10.1). We then propose a number of future observations that might enable us to answer these questions, either by missions currently planned for flight or by missions for which architectures have yet to be developed (Section 10.10.2).

10.10.1 Outstanding Tectonic Questions

With Mercury's tectonic character so dominated by global contraction, it is prudent to continue to explore this fundamental process. Interior cooling and its consequences have played controlling roles in the planet's thermal, volcanic, and tectonic evolution (Chapters 11 and 19), but a complete understanding of this control is possible only once we characterize fully the history of global contraction for Mercury.

For example, we still do not know when this process started, in part because Mercury's record of tectonic deformation may date only from the end of the LHB (Section 10.8.1), and in part because thermal evolution models can describe multiple cooling scenarios of varying onset and duration. Similarly, the history of recent global contraction is not well understood. Given that the planet's extant magnetic field (Chapter 5) requires a molten and convecting core, heat must flow from the core to the mantle (Chapter 19), and so Mercury must still be cooling and contracting. Relatively small and well-preserved landforms interpreted to represent crustal shortening (Figures 10.17 and 10.18) attest to thrust faulting, and therefore likely global contraction, having occurred within the past several hundred million years (Section 10.8.1). However, although the rate of contraction has likely decreased through time (Section 10.8.4), we do not yet know for certain if the stresses from global contraction today remain sufficient to overcome the frictional strength of Mercury's lithosphere. Accordingly, exploring how the strain rate from contraction has varied through time will improve constraints on thermal models of the planet's interior evolution (e.g., Michel et al., 2013; Tosi et al., 2013).

Understanding the contribution to tectonic deformation of Mercury's surface from processes other than global contraction remains an important task, too. As assessment of the areal strain recorded by shortening structures in the intercrater plains versus that for smooth plains structures may indicate whether stresses from vertical loading have contributed to the formation of the latter set of landforms (e.g., Melosh and McKinnon, 1988; see also Section 10.6.4). Similarly, the effects of solar tidal stresses and thermal stresses (e.g., Beuthe, 2010; Williams et al., 2011) from Mercury's spin-orbit resonance on its lithosphere and on its global fault pattern remain to be fully investigated. And, of course, determining the mechanism(s) responsible for modifying Mercury's topography at long wavelengths is important for understanding whether these enigmatic troughs and rises reflect a component of global contraction, and whether such features might exist on other worlds. Characterizing the planet-wide distribution of the long-wavelength undulations, including

establishing whether they are present in the southern hemisphere, will be key to this understanding.

The influence, if any, of changes in Mercury's spin rate on the planet's tectonics also remains to be fully characterized. For scenarios under which tidal spindown occurred early in the planet's history and spanned some hundreds of millions of years, or started during or even after the LHB but spanned a much shorter duration, or was affected by a change in Mercury's rate of rotation during or after the LHB by one or more large impacts and/or variations in orbital eccentricity, it is not difficult to imagine that despinning overlapped temporally with global contraction. If, on the other hand, the change in Mercury's spin rate was a short-lived process and/or operated only before the LHB, then for this mechanism to have influenced the tectonic pattern seen on the planet today the structures it formed must have been sufficiently deep-seated to survive resurfacing from the impact bombardment and effusive volcanism that was responsible for erasing the planet's surface features older than ~4.1 Ga (Marchi et al., 2013; Chapter 9).

Determining whether the perceived north-south fabric of Mercury's shortening structures is an artifact of solar illumination, with artificially illuminated DEMs, for example, is also an important objective, for the answer will either update existing models for the planet's tectonic and thermal evolution or call for the formulation of new ones.

Mercury's tectonic landforms themselves warrant further analysis. For example, the distinction in type of shortening structure we give here (e.g., smooth plains structure, cratered plains structure) is motivated by the observation that such landforms often share morphological characteristics that defy a straightforward classification as wrinkle ridge or lobate scarp (Section 10.2.1). The broad variety in form of these structures has not been quantified for Mercury, and so as yet there is no *systematically* robust classification scheme for the planet's inventory of thrust-fault-related landforms. Such an analysis would also provide key structural information such as fault linkage, frequency and extent of thrust duplexes at the leading edges of shortening structures, and the geometry and depth of penetration of the underlying fault surfaces. These last parameters are especially important, as the fault dip angles used in estimates of global contraction-induced radius change (i.e., $\theta = 25^\circ\text{--}35^\circ$) (Section 10.6.1) are greater than dip angles found for select thrust faults on Mercury (Galluzzi et al., 2015), as well as for deep-seated thrusts beneath the Mare Crisium basin on the Moon (Byrne et al., 2015). The use of fault dip angles as low as 7° (Galluzzi et al., 2015) would increase estimates of the amount of Mercury's radial shortening accommodated by brittle structures beyond even the highest published values to date (Byrne et al., 2014). Moreover, the structural arrangement on the Moon, whereby large thrust faults bound an elevated portion of the crust-mantle boundary beneath large impact basins (Byrne et al., 2015), may apply to Mercury but has yet to be investigated.

Finally, the initial state of global contraction is thought to be characterized geometrically by extension at the surface (e.g., Delamétherie, 1795a; Dana, 1873; Ampferer, 1923), with extensional structures propagating to some depth (de Buffon, 1788; Delamétherie, 1795b). As contraction progresses, the outermost layers would be put into compression, separated from layers

continuing to extend below by a surface of no strain that deepens with time (e.g., Wilson, 1954; Jeffreys, 1976) – much as thermally contracting lavas behave (e.g., Blair et al., 2013), albeit at a far greater scale. Moreover, some thermal evolution models for Mercury predict an early phase of global expansion as a function of mantle differentiation (e.g., Grott et al., 2011; Tosi et al., 2013). Such incipient and/or large-scale extension has not been substantially investigated for Mercury, and any resulting deformation probably preceded the emplacement of even the oldest surface now preserved on the planet (Marchi et al., 2013). Yet high-resolution gravity gradiometry data for the Moon have revealed a global system of deep-seated features with no surface manifestation that are interpreted to be ancient, giant dikes formed in an early stage of lunar expansion (Andrews-Hanna et al., 2013). The acquisition of similar high-resolution gravity field data for Mercury could establish whether such buried structures are present within the planet. The identification of such structures would provide compelling support for an early period of contraction-induced rifting or even planetary expansion, with those rifts facilitating the rapid and widespread eruption of flood basalts onto the surface of the planet (e.g., Whitten et al., 2014; Evans et al., 2015; Chapter 11).

10.10.2 Future Observations

The wealth of data sets returned by the MESSENGER spacecraft has provided a detailed and integrated insight into the character and history of the innermost planet, from which we can identify further observations needed to address the questions above, among many others. Such observations would help frame the science campaigns of future missions to Mercury, such as the joint European Space Agency–Japan Aerospace Exploration Agency BepiColombo mission (e.g., Benkhoff et al., 2010), scheduled to launch in 2018, and may even inspire later missions to the innermost planet (Chapter 20).

For example, much remains to be done in characterizing the tectonics of Mercury's southern hemisphere. High-resolution targeted images of shortening landforms there would complement similar data for northern hemisphere structures, as enabled by MESSENGER's periapsis at high northern latitudes (Chapter 1). Similarly, high-resolution measurements of the topography and gravity field and the development of crustal thickness models for the southern hemisphere would provide a geophysical context for photogeological observations of the tectonics there. Such new data would also act as a basis for comparing fault displacement-gradient fold morphology, fault penetration depth, and displacement-length scaling of the structures in both hemispheres, as well as information on the depth and degree of fracturing of the planet's lithosphere in general.

But what of yet more ambitious exploration efforts? Interferometric synthetic aperture radar (InSAR), for example, has been used to identify and characterize ongoing tectonic deformation on Earth (e.g., Bürgmann et al., 2000). InSAR measurements from orbital assets at Mercury could be used to search for evidence of active surface change on the planet, including fault slip – a crucial observation for understanding

the rate of global contraction and whether tectonic deformation is active on the innermost planet today. A seismic station, or better yet a seismic network, would yield unprecedented views of Mercury's interior. Such a mission would contribute not only to the search for active faulting, but could also yield critical information on the structure of the lithosphere and whether Mercury possesses a solid inner core (Chapter 19). Linking measurements of Mercury's present interior structure with observations of almost four billion years of tectonic deformation would considerably expand our understanding not only of that planet's thermal, tectonic, and volcanic histories, but also of silicate bodies throughout the solar system. Moreover, with the increasing number of terrestrial planets identified in extrasolar planetary systems, including ones as small as Mercury (e.g., Barclay et al., 2013), our solar system's innermost planet may come to serve as a case study with which to understand the global cooling and contractional histories of rocky, one-plate planets in general.

The objectives of future missions to Mercury, from BepiColombo forward, will reflect and build on the findings of the MESSENGER mission. Our understanding of the planet's tectonic character has never been more comprehensive, but there is much left to learn. What we can state with certainty for now, however, is that MESSENGER has given us compelling reasons to continue to investigate enigmatic Mercury, and that it is worth going back.

REFERENCES

- Ahrens, T. J. and Rubin, A. M. (1993). Impact-induced tensional failure in rock. *J. Geophys. Res.*, **98**, 1185–1203.
- Ampferer, A. (1923). Beiträge zur Auflösung der Mechanik der Alpen. *Jahrb. Geol. Bundesanst.*, **76**, 125–151.
- Anderson, E. M. (1951). *The Dynamics of Faulting and Dyke Formation with Applications to Britain*, 2nd edn. Edinburgh, UK: Oliver and Boyd.
- Andrews-Hanna, J. C., Asmar, S. W., Head, J. W., Kiefer, W. S., Konopliv, A. S., Lemoine, F. G., Matsuyama, I., Mazarico, E., McGovern P. J., Melosh, H. J., Neumann, G. A., Nimmo, F., Phillips, R. J., Smith, D. E., Solomon, S. C., Taylor, J., Wieczorek, M. A., Williams, J. G. and Zuber M. T. (2013). Ancient igneous intrusions and early expansion of the Moon revealed by GRAIL gravity gradiometry. *Science*, **339**, 675–678.
- Asphaug, E. (2014). Impact origin of the Moon? *Annu. Rev. Earth Planet. Sci.*, **42**, 551–578.
- Balcerski, J. A., Hauck, S. A., II and Sun, P. (2012). Tilted crater floors: Recording the history of Mercury's long-wavelength deformation. *Lunar Planet. Sci.*, **43**, abstract 1850.
- Balcerski, J. A., Hauck, S. A., II and Sun, P. (2013). New constraints on timing and mechanisms of regional tectonism from Mercury's tilted craters. *Lunar Planet. Sci.*, **44**, abstract 2444.
- Banks, M. E., Xiao, Z., Watters, T. R., Strom, R. G., Braden, S. E., Chapman, C. R., Solomon, S. C., Klimczak, C. and Byrne, P. K. (2015). Duration of activity on lobate-scarp thrust faults on Mercury. *J. Geophys. Res. Planets*, **120**, 1751–1762.
- Barclay, T., Rowe, J. F., Lissauer, J. J., Huber, D., Fressin, F., Howell, S. B., Bryson, S. T., Chaplin, W. J., Désert, J. M., Lopez, E. D., Marcy, G. W., Mullally, F., Ragozzine, D., Torres, G., Adams, E. R., Agol, E., Barrado, D., Basu, S., Bedding, T. R., Buchhave, L. A., Charbonneau, D., Christiansen, J. L., Christensen-Dalsgaard,

- J., Ciardi, D., Cochran, W. D., Dupree, A. K., Elsworth, Y., Everett, M., Fischer, D. A., Ford, E. B., Fortney, J. J., Geary, J. C., Haas, M. R., Handberg, R., Hekker, S., Henze, C. E., Horch, E., Howard, A. W., Hunter, R. C., Isaacson, H., Jenkins, J. M., Karoff, C., Kawaler, S. D., Kjeldsen, H., Klaus, T. C., Latham, D. W., Li, J., Lillo-Box, J., Lund, M. N., Lundkvist, M., Metcalfe, T. S., Miglio, A., Morris, R. L., Quintana, E. V., Stello, D., Smith, J. C., Still, M. and Thompson, S. E. (2013). A sub-Mercury-sized exoplanet. *Nature*, **494**, 452–454.
- Barton, N. (1976). Rock mechanics review: The shear strength of rock and rock joints. *Int. J. Rock Mech. Min. Sci.*, **13**, 255–279.
- Becker, K. J., Robinson, M. S., Becker, T. L., Weller, L. A., Edmundson, K. L., Neumann, G. A., Perry, M. E. and Solomon, S. C. (2016). First global digital elevation model of Mercury. *Lunar Planet. Sci.*, **47**, abstract 2959.
- Benkhoff, J., van Casteren, J., Hayakawa, H., Fujimoto, M., Laakso, H., Novara, M., Ferri, P., Middleton, H. R. and Ziethe, R. (2010). BepiColombo – Comprehensive exploration of Mercury: Mission overview and science goals. *Planet. Space Sci.*, **58**, 2–20.
- Benz, W., Slattery, W. L. and Cameron, A. G. W. (1988). Collisional stripping of Mercury's mantle. *Icarus*, **74**, 516–528.
- Beuthe, M. (2010). East–west faults due to planetary contraction. *Icarus*, **209**, 795–817.
- Bieniawski, Z. T. (1989). *Engineering Rock Mass Classifications*. New York: Wiley.
- Blair, D. M., Freed, A. M., Byrne, P. K., Klimczak, C., Prockter, L. M., Ernst, C. M., Solomon, S. C., Melosh, H. J. and Zuber, M. T. (2013). The origin of graben and ridges in Rachmaninoff, Raditladi, and Mozart basins, Mercury. *J. Geophys. Res. Planets*, **118**, 47–58.
- Bois, C., Cazes, M., Damotte, B., Galdeano, A., Hirn, A., Mascle, A., Matte, P., Raoult, J. F. and Torreilles, G. (1986). Deep seismic profiling of the crust in northern France: The Ecors project. In *Reflection Seismology: A Global Perspective*, eds. M. Barazangi and L. Brown, Geodynamics Series, Vol. 13. Washington, DC: American Geophysical Union, pp. 21–29.
- Brace, W. F. and Kohlstedt, D. L. (1980). Limits on lithospheric stress imposed by laboratory experiments. *J. Geophys. Res.*, **85**, 6248–6252.
- Bürgmann, R., Rosen, P. A. and Fielding, E. J. (2000). Synthetic aperture radar interferometry to measure Earth's surface topography and its deformation. *Annu. Rev. Earth Planet. Sci.*, **28**, 169–209.
- Burke, K. C., Sengör, A. M. C. and Francis, P. W. (1984.) Maxwell Montes in Ishtar: A collisional plateau on Venus? *Lunar Planet. Sci.*, **15**, 104–105.
- Burns, J. A. (1975). The angular momenta of solar system bodies: Implications for asteroid strengths. *Icarus*, **25**, 545–554.
- Burns, J. A. (1976). Consequences of the tidal slowing of Mercury. *Icarus*, **28**, 453–458.
- Butler, R. W. H. (1982). The terminology of structures in thrust belts. *J. Struct. Geol.*, **4**, 239–245.
- Byerlee, J. D. (1968). Brittle–ductile transition in rocks. *J. Geophys. Res.*, **73**, 4741–4750.
- Byerlee, J. D. (1978). Friction of rocks. *Pure Appl. Geophys.*, **116**, 615–626.
- Byrne, P. K., Klimczak, C., Blair, D. M., Ferrari, S., Solomon, S. C., Freed, A. M., Watters, T. R. and Murchie, S. L. (2013a). Tectonic complexity within volcanically infilled craters and basins on Mercury. *Lunar Planet. Sci.*, **44**, abstract 1261.
- Byrne, P. K., Klimczak, C., Williams, D. A., Hurwitz, D. M., Solomon, S. C., Head, J. W., Preusker, F. and Oberst, J. (2013b). An assemblage of lava flow features on Mercury. *J. Geophys. Res. Planets*, **118**, 1303–1322.
- Byrne, P. K., Klimczak, C., Sengör, A. M. C., Solomon, S. C., Watters, T. R. and Hauck, S. A., II (2014). Mercury's global contraction much greater than earlier estimates. *Nature Geosci.*, **7**, 301–307.
- Byrne, P. K., Klimczak, C., McGovern, P. J., Mazarico, E., James, P. B., Neumann, G. A., Zuber, M. T. and Solomon, S. C. (2015). Deep-seated thrust faults bound the Mare Crisium lunar mascon. *Earth Planet. Sci. Lett.*, **427**, 183–190.
- Byrne, P. K., Klimczak, C. and LaFond, J. K. (2016a). The East Kaibab monocline: A Terran lobate scarp? *Lunar Planet. Sci.*, **47**, abstract 1022.
- Byrne, P. K., Ostrach, L. R., Fassett, C. I., Chapman, C. R., Denevi, B. W., Evans, A. J., Klimczak, C., Banks, M. E., Head, J. W. and Solomon, S. C. (2016b). Widespread effusive volcanism on Mercury likely ended by about 3.5 Ga. *Geophys. Res. Lett.*, **43**, 7408–7416.
- Cashman, K. V. (2004). Volatile controls on magma ascent and eruption. In *The State of the Planet: Frontiers and Challenges in Geophysics*, ed. R. S. J. Sparks and C. J. Hawkesworth. Washington, DC: American Geophysical Union, pp. 109–124.
- Cavanaugh, J. F., Smith, J. C., Sun, X., Bartels, A. E., Ramos-Izquierdo, L., Krebs, D. J., McGarry, J. F., Trunzo, R., Novogradac, A. M., Britt, J. L., Karsh, J., Katz, R. B., Lukemire, A. T., Szymkiewicz, R., Berry, D. L., Swinski, J. P., Neumann, G. A., Zuber, M. T. and Smith, D. E. (2007). The Mercury Laser Altimeter instrument for the MESSENGER mission. *Space Sci. Rev.*, **131**, 451–479.
- Chabot, N. L., Denevi, B. W., Murchie, S. L., Hash, C. D., Ernst, C. M., Blewett, D. T., Nair, H., Laslo, N. R. and Solomon, S. C. (2016). Mapping Mercury: Global imaging strategy and products from the MESSENGER mission. *Lunar Planet. Sci.*, **47**, abstract 1256.
- Clark, R. M. and Cox, S. (1996). A modern regression approach to determining fault displacement–length scaling relationships. *J. Struct. Geol.*, **18**, 147–152.
- Collins, G. S., Melosh, H. J. and Ivanov, B. A. (2004). Modeling damage and deformation in impact simulations. *Meteorit. Planet. Sci.*, **39**, 217–231.
- Colton, G. W., Howard, K. A. and Moore, H. J. (1972). Mare ridges and arches in southern Oceanus Procellarum. In *Apollo 16 Preliminary Science Report*, Special Publication SP-315. Washington, DC: NASA, pp. 29–90–29–93.
- Correia, A. C. M. and Laskar, J. (2004). Mercury's capture into the 3/2 spin–orbit resonance as a result of its chaotic dynamics. *Nature*, **429**, 848–850.
- Correia, A. C. M. and Laskar, J. (2009). Mercury's capture into the 3/2 spin–orbit resonance including the effect of core–mantle friction. *Icarus*, **201**, 1–11.
- Correia, A. C. M. and Laskar, J. (2012). Impact cratering on Mercury: Consequences for the spin evolution. *Astrophys. J. Lett.*, **751**, L43, 5 pp.
- Cowie, P. A., Scholz, C. H., Edwards, M. and Malinverno, A. (1993). Fault strain and seismic coupling on mid-ocean ridges. *J. Geophys. Res.*, **98**, 17,911–17,920.
- Cowie, P. A., Scholz, C. H., Roberts, G. P., Faure Walker, J. P. and Steer, P. (2013). Viscous roots of active seismogenic faults revealed by geologic slip rate variations. *Nature Geosci.*, **6**, 1036–1040.
- Cunje, A. B. and Ghent, R. R. (2016). Caloris basin, Mercury: History of deformation from an analysis of tectonic landforms. *Icarus*, **268**, 131–144.
- Cunningham, W. D., Windley, B. F., Dorjnamjaa, D., Badamgarov, G. and Saandar, M. (1996). Late Cenozoic transpression in southwestern Mongolia and the Gobi Altai–Tien Shan connection. *Earth Planet. Sci. Lett.*, **140**, 67–82.

- Dainty, A. M., Toksöz, M. N., Anderson, K. R., Pines, P. J., Nakamura, Y. and Latham, G. (1974). Seismic scattering and shallow structure of the Moon in Oceanus Procellarum. *Moon*, **9**, 11–29.
- Dana, J. D. (1863). *Manual of Geology: Treating of the Principles of the Science with Special Reference to American Geological History, for the Use of Colleges, Academies and Schools of Science*. Philadelphia, PA: Theodore Bliss & Co., 798 pp.
- Dana, J. D. (1873). On some results of the Earth's contraction from cooling, including a discussion of the origin of mountains and the nature of the Earth's interior. *Amer. J. Sci.*, **5**, 423–443.
- Delamétherie, J.-C. (1795a). *Théorie de la Terre*, tome premier. Paris: Chez Maradan, 422 pp.
- Delamétherie, J.-C. (1795b). *Théorie de la Terre*, tome second. Paris: Chez Maradan, 456 pp.
- de Buffon, C. (1778). *Histoire Naturelle Générale et Particulière*. Paris: Imprimerie Royale, 615 pp.
- Denevi, B. W., Robinson, M. S., Solomon, S. C., Murchie, S. L., Blewett, D. T., Domingue, D. L., McCoy, T. J., Ernst, C. M., Head, J. W., III, Watters T. R. and Chabot, N. L. (2009). The evolution of Mercury's crust: A global perspective from MESSENGER. *Science*, **324**, 613–618.
- Denevi, B. W., Ernst, C. M., Meyer, H. M., Robinson, M. S., Murchie, S. L., Whitten, J. L., Head, J. W., Watters, T. R., Solomon, S. C., Ostrach, L. R., Chapman, C. R., Byrne, P. K., Klimczak, C. and Peplowski, P. N. (2013). The distribution and origin of smooth plains on Mercury. *J. Geophys. Res. Planets*, **118**, 891–907.
- Di Achille, G., Popa, C., Massironi, M., Epifani, E. M., Zusi, M., Cremonese, G. and Palumbo, P. (2012). Mercury's radius change estimates revisited using MESSENGER data. *Icarus*, **221**, 456–460.
- Dombard, A. J. and Hauck, S. A., II (2008). Despinning plus global contraction and the orientation of lobate scarps on Mercury: Predictions for MESSENGER. *Icarus*, **198**, 274–276.
- Dombard, A. J., Hauck, S. A., II, Solomon, S. C. and Phillips, R. J. (2001). Potential for long-wavelength folding on Mercury. *Lunar Planet. Sci.*, **32**, abstract 2035.
- Duncan, R. A. and Richards, M. A. (1991). Hotspots, mantle plumes, flood basalts, and true polar wander. *Rev. Geophys.*, **29**, 31–50.
- Dzurisin, D. (1978). The tectonic and volcanic history of Mercury as inferred from studies of scarps, ridges, troughs, and other lineaments. *J. Geophys. Res.*, **83**, 4883–4906.
- Egea-González, I., Ruiz, J., Fernández, C., Williams, J.-P., Márquez, Á. and Lara, L. M. (2012). Depth of faulting and ancient heat flows in the Kuiper region of Mercury from lobate scarp topography. *Planet. Space Sci.*, **60**, 193–198.
- Élie de Beaumont, L. (1829). Faits pour Servir à l'Histoire des Montagnes de l'Oisans. *Mémoires de la Société d'Histoire Naturelle de Paris*, 1–32.
- Élie de Beaumont, L. (1852). *Notice sur les Systèmes de Montagnes*, III. Paris: P. Bertrand, pp. 1069–1543.
- Emmermann, R. and Lauterjung, J. (1997). The German continental deep drilling program KTB: Overview and major results. *J. Geophys. Res.*, **102**, 18,179–18,201.
- Engelder, T. (1992). *Stress Regimes in the Lithosphere*. Princeton, NJ: Princeton University Press.
- Ernst, C. M., Murchie, S. L., Barnouin, O. S., Robinson, M. S., Denevi, B. W., Blewett, D. T., Head, J. W., Izenberg, N. R., Solomon, S. C. and Roberts, J. H. (2010). Exposure of spectrally distinct material by impact craters on Mercury: Implications for global stratigraphy. *Icarus*, **209**, 210–223.
- Evans, A. J., Brown, S. M. and Solomon, S. C. (2015). Characteristics of early mantle convection and melting on Mercury. *Lunar Planet. Sci.*, **46**, abstract 2414.
- Fassett, C. I. and Crowley, M. C. (2016). High-resolution stereo digital terrain models of Mercury: Crater degradation and morphometry. *Lunar Planet. Sci.*, **47**, abstract 1046.
- Fassett, C. I., Head, J. W., Blewett, D. T., Chapman, C. R., Dickson, J. L., Murchie, S. L., Solomon, S. C. and Watters, T. R. (2009). Caloris impact basin: Exterior geomorphology, stratigraphy, morphometry, radial sculpture, and smooth plains deposits. *Earth Planet. Sci. Lett.*, **285**, 297–308.
- Fassett, C. I., Head, J. W., Baker, D. M. H., Zuber, M. T., Smith, D. E., Neumann, G. A., Solomon, S. C., Klimczak, C., Strom, R. G., Chapman, C. R., Prockter, L. M., Phillips, R. J., Oberst, J. and Preusker, F. (2012). Large impact basins on Mercury: Global distribution, characteristics, and modification history from MESSENGER orbital data. *J. Geophys. Res.*, **117**, E00L08.
- Fegan, E. R., Rothery, D. A., Marchi, S., Massironi, M., Conway, S. J. and Anand, M. (2017). Late movement of basin-edge lobate scarps on Mercury. *Icarus*, **288**, 226–234.
- Ferrari, S., Massironi, M., Marchi, S., Byrne, P. K., Klimczak, C., Martellato, E. and Cremonese, G. (2015). Age relationships of the Rembrandt basin and Enterprise Rupes, Mercury. In *Volcanism and Tectonism Across the Solar System*, ed. T. Platz, M. Massironi, P. K. Byrne and H. Hiesinger, Special Publication 401. London: Geological Society, pp. 159–172.
- Fletcher, R. C. and Hallet B. (1983). Unstable extension of the lithosphere: A mechanical model for basin-and-range structure. *J. Geophys. Res.*, **88**, 7457–7466.
- Fodor, L., Turki, S. M., Dalub, H. and Al Gerbi, A. (2005). Fault-related folds and along-dip segmentation of breaching faults: Syn-diagenetic deformation in the south-western Sirt basin, Libya. *Terra Nova*, **17**, 121–128.
- Freed, A. M., Solomon, S. C., Watters, T. R., Phillips, R. J. and Zuber, M. T. (2009). Could Pantheon Fossae be the result of the Apollodorus crater-forming impact within the Caloris basin, Mercury? *Earth Planet. Sci. Lett.*, **285**, 320–327.
- Freed, A. M., Blair, D. M., Watters, T. R., Klimczak, C., Byrne, P. K., Solomon, S. C., Zuber, M. T. and Melosh, H. J. (2012). On the origin of graben and ridges within and near volcanically buried craters and basins in Mercury's northern plains. *J. Geophys. Res.*, **117**, E00L06, doi:10.1029/2012JE004119.
- Galluzzi, V., Di Achille, G., Ferranti, L., Popa, C. and Palumbo, P. (2015). Faulted craters as indicators for thrust motions on Mercury. In *Volcanism and Tectonism Across the Solar System*, ed. T. Platz, M. Massironi, P. K. Byrne and H. Hiesinger, Special Publication 401. London: Geological Society, pp. 313–326.
- Gettings, M. E. (1988). Variation of depth to the brittle-ductile transition due to cooling of a midcrustal intrusion. *Geophys. Res. Lett.*, **15**, 213–216.
- Giacomini, L., Massironi, M., Marchi, S., Fassett, C. I., Di Achille, G. and Cremonese, G. (2015). Age dating of an extensive thrust system on Mercury: Implications for the planet's thermal evolution. In *Volcanism and Tectonism Across the Solar System*, ed. T. Platz, M. Massironi, P. K. Byrne and H. Hiesinger, Special Publication 401. London: Geological Society, pp. 291–312.
- Glazner, A. F. (1991). Plutonism, oblique subduction, and continental growth: An example from the Mesozoic of California. *Geology*, **19**, 784–786.
- Golombek, M. P., Plescia, J. B. and Franklin, B. J. (1991). Faulting and folding in the formation of planetary wrinkle ridges. In *Proceedings of Lunar and Planetary Science*, **21**. Houston, TX: Lunar and Planetary Institute, pp. 679–693.
- Golombek, M. P., Anderson, F. S. and Zuber, M. T. (2001). Martian wrinkle ridge topography: Evidence for subsurface faults from MOLA. *J. Geophys. Res.*, **106**, 23,811–23,821.

- Goudge, T. A., Head, J. W., Kerber, L., Blewett, D. T., Denevi, B. W., Domingue, D. L., Gillis-Davis, J. J., Gwinner, K., Helbert, J., Holsclaw, G. M., Izenberg, N. R., Klima, R. L., McClintock, W. E., Murchie, S. L., Neumann, G. A., Smith, D. E., Strom, R. G., Xiao, Z., Zuber, M. T. and Solomon, S. C. (2014). Global inventory and characterization of pyroclastic deposits on Mercury: New insights into pyroclastic activity from MESSENGER orbital data. *J. Geophys. Res. Planets*, **119**, 635–658.
- Grott, M., Breuer, D. and Laneuveille, M. (2011). Thermo-chemical evolution and global contraction of Mercury. *Earth Planet. Sci. Lett.*, **307**, 135–146.
- Habermann, M. A. and Klimczak, C. (2015). Tectonic controls of pyroclastic volcanism on Mercury. Presented at 2018 Fall Meeting, American Geophysical Union, abstract P53A-2101, San Francisco, CA, 14–18 December.
- Hamilton, W. B. (1995). Subduction systems and magmatism. In *Volcanism Associated with Extension at Consuming Plate Margins*, ed. J. L. Smellie, Special Publication 81. London: Geological Society, pp. 3–28.
- Hatcher, R. D., Jr. (1989). Tectonic synthesis of the U.S. Appalachians. In *The Appalachian-Ouachita Orogen in the United States*, ed. R. D. Hatcher, Jr., W. A. Thomas and G. W. Viele. Boulder, CO: Geological Society of America, pp. 511–536.
- Hauck, S. A., II, Dombard, A. J., Phillips, R. J. and Solomon, S. C. (2004). Internal and tectonic evolution of Mercury. *Earth Planet. Sci. Lett.*, **222**, 713–728.
- Hauck, S. A., II, Margot, J.-L., Solomon, S. C., Phillips, R. J., Johnson, C. L., Lemoine, F. G., Mazarico, E., McCoy, T. J., Padovan, S., Peale, S. J., Perry, M. E., Smith, D. E. and Zuber, M. T. (2013). The curious case of Mercury's internal structure. *J. Geophys. Res. Planets*, **118**, 1204–1220.
- Hawkins, S. E., III, Boldt, J. D., Darlington, E. H., Espiritu, R., Gold, R. E., Gotwols, B., Grey, M. P., Hash, C. D., Hayes, J. R., Jaskulek, S. E., Kardian, C. J., Jr., Keller, M. R., Malaret, E. R., Murchie, S. L., Murphy, P. K., Peacock, K., Prockter, L. M., Reiter, R. A., Robinson, M. S., Schaefer, E. D., Shelton, R. G., Stern, R. E., II, Taylor, H. W., Watters, T. R. and Williams, B. D. (2007). The Mercury Dual Imaging System on the MESSENGER spacecraft. *Space Sci. Rev.*, **131**, 247–338.
- Head, J. W., Murchie, S. L., Prockter, L. M., Robinson, M. S., Solomon, S. C., Strom, R. G., Chapman, C. R., Watters, T. R., McClintock, W. E., Blewett, D. T. and Gillis-Davis, J. J. (2008). Volcanism on Mercury: Evidence from the first MESSENGER flyby. *Science*, **321**, 69–72.
- Head, J. W., Murchie, S. L., Prockter, L. M., Solomon, S. C., Strom, R. G., Chapman, C. R., Watters, T. R., Blewett, D. T., Gillis-Davis, J. J., Fassett, C. I., Dickson, J. L., Hurwitz, D. M. and Ostrach, L. R. (2009). Evidence for intrusive activity on Mercury from the first MESSENGER flyby. *Earth Planet. Sci. Lett.*, **285**, 251–262.
- Head, J. W., Chapman, C. R., Strom, R. G., Fassett, C. I., Denevi, B. W., Blewett, D. T., Ernst, C. M., Watters, T. R., Solomon, S. C., Murchie, S. L., Prockter, L. M., Chabot, N. L., Gillis-Davis, J. J., Whitten, J. L., Goudge, T. A., Baker, D. M. H., Hurwitz, D. M., Ostrach, L. R., Xiao, Z., Merline, W. J., Kerber, L., Dickson, J. L., Oberst, J., Byrne, P. K., Klimczak, C. and Nittler, L. R. (2011). Flood volcanism in the northern high latitudes of Mercury revealed by MESSENGER. *Science*, **333**, 1853–1856.
- Heap, M. J., Byrne, P. K. and Mikhail, S. (2017). Low surface gravitational acceleration of Mars results in a thick and weak lithosphere: Implications for topography, volcanism, and hydrology. *Icarus*, **281**, 103–114.
- Hoek, E. and Diederichs, M. S. (2006). Empirical estimation of rock mass modulus. *Int. J. Rock Mech. Min. Sci.*, **43**, 203–215.
- Jacobs, J. A., Russell, R. D. and Wilson, J. T. (1959). *Physics and Geology*. New York: McGraw-Hill, 424 pp.
- James, P. B., Byrne, P. K., Solomon, S. C., Zuber, M. T. and Phillips, R. J. (2014). Surface strains associated with the evolution of Mercury's domical swells. Presented at 2014 Fall Meeting, American Geophysical Union, abstract P21C-3939, San Francisco, CA, 15–19 December.
- James, P. B., Zuber, M. T., Phillips, R. J. and Solomon, S. C. (2015). Support of long-wavelength topography on Mercury inferred from MESSENGER measurements of gravity and topography. *J. Geophys. Res. Planets*, **120**, 287–310.
- Jeffreys, H. (1976). *The Earth: Its Origin, History and Physical Constitution*, 6th edn. Cambridge: Cambridge University Press, 574 pp.
- Jerram, D. A. and Widdowson, M. (2005). The anatomy of continental flood basalt provinces: Geological constraints on the processes and products of flood volcanism. *Lithos*, **79**, 385–405.
- Kachanov, M. (1992). Effective elastic properties of cracked solids: Critical review of some basic concepts. *Appl. Mech. Rev.*, **45**, 304–335.
- Karimi, M. and Dombard, A. J. (2014). A study regarding the possibility of true polar wander on the asteroid Vesta. Presented at 2014 Fall Meeting, American Geophysical Union, abstract P43C-4003, San Francisco, CA, 15–19 December.
- Kaula, W. M. (1968). *An Introduction to Planetary Physics: The Terrestrial Planets*. New York: John Wiley.
- Kennedy, P. J., Freed, A. M. and Solomon, S. C. (2008). Mechanisms of faulting in and around Caloris basin, Mercury. *J. Geophys. Res.*, **113**, E08004, doi:10.1029/2007JE002992.
- Kerber, L., Head, J. W., Solomon, S. C., Murchie, S. L., Blewett, D. T. and Wilson, L. (2009). Explosive volcanic eruptions on Mercury: Eruption conditions, magma volatile content, and implications for interior volatile abundances. *Earth Planet. Sci. Lett.*, **285**, 263–271.
- Kerber, L., Head, J. W., Blewett, D. T., Solomon, S. C., Wilson, L., Murchie, S. L., Robinson, M. S., Denevi, B. W. and Domingue, D. L. (2011). The global distribution of pyroclastic deposits on Mercury: The view from MESSENGER flybys 1–3. *Planet. Space Sci.*, **59**, 1895–1909.
- King, S. D. (2008). Pattern of lobate scarps on Mercury's surface reproduced by a model of mantle convection. *Nature Geosci.*, **1**, 229–232.
- Klimczak, C. (2014). Geomorphology of lunar grabens requires igneous dikes at depth. *Geology*, **42**, 963–966.
- Klimczak, C. (2015). Limits on the brittle strength of planetary lithospheres undergoing global contraction. *J. Geophys. Res. Planets*, **120**, 2135–2151.
- Klimczak, C., Schultz, R. A. and Nahm, A. L. (2010). Evaluation of the origin hypotheses of Pantheon Fossae, central Caloris basin, Mercury. *Icarus*, **209**, 262–270.
- Klimczak, C., Watters, T. R., Ernst, C. M., Freed, A. M., Byrne, P. K., Solomon, S. C., Blair, D. M. and Head, J. W. (2012). Deformation associated with ghost craters and basins in volcanic smooth plains on Mercury: Strain analysis and implications for plains evolution. *J. Geophys. Res.*, **117**, E00L03, doi:10.1029/2012JE004100.
- Klimczak, C., Ernst, C. M., Byrne, P. K., Solomon, S. C., Watters, T. R., Murchie, S. L., Preusker, F. and Balcerzki, J. A. (2013a). Insights into the subsurface structure of the Caloris basin, Mercury, from assessments of mechanical layering and changes in long-wavelength topography. *J. Geophys. Res. Planets*, **118**, 2030–2044.
- Klimczak, C., Byrne, P. K., Solomon, S. C., Nimmo, F., Watters, T. R., Denevi, B. W., Ernst, C. M. and Banks, M. E. (2013b). The role of

- thrust faults as conduits for volatiles on Mercury. *Lunar Planet. Sci.*, **44**, abstract 1390.
- Klimczak, C., Byrne, P. K. and Solomon, S. C. (2015). A rock-mechanical assessment of Mercury's global tectonic fabric. *Earth Planet. Sci. Lett.*, **416**, 82–90.
- Knibbe, J. S. and van Westrenen, W. (2016). Mercury's past rotation and cratering distribution. *Lunar Planet. Sci.*, **47**, abstract 1445.
- Kohlstedt, D. L. and Mackwell, S. J. (2010). Strength and deformation of planetary lithospheres. In *Planetary Tectonics*, ed. T. R. Watters and R. A. Schultz. New York: Cambridge University Press, pp. 397–456.
- Kohlstedt, D. L., Evans, B. and Mackwell, S. J. (1995). Strength of the lithosphere: Constraints imposed by laboratory experiments. *J. Geophys. Res.*, **100**, 17,587–17,602.
- Kuang, W., Jiang, W., Roberts, J. and Frey, H. V. (2014). Could giant basin-forming impacts have killed Martian dynamo? *Geophys. Res. Lett.*, **41**, 8006–8012.
- Kulhawy, F. H. (1975). Stress deformation properties of rock and rock discontinuities. *Eng. Geol.*, **9**, 327–350.
- Last, G. V., Winsor, K. and Unwin, S. G. (2012). *A Summary of Information on the Behavior of the Yakima Fold Belt as a Structural Entity*. Topical Report, Richland, WA: Pacific Northwest National Laboratory, 82 pp.
- Le Corvec, N., McGovern, P. J., Grosfils, E. B. and Galanga, G. (2015). Effects of crustal-scale mechanical layering on magma chamber failure and magma propagation within the Venusian lithosphere. *J. Geophys. Res. Planets*, **120**, 1279–1297.
- Le Feuvre, M. and Wieczorek, M. A. (2011). Nonuniform cratering of the Moon and a revised crater chronology of the inner Solar System. *Icarus*, **214**, 1–20.
- Lissauer, J. J. (1985). Can cometary bombardment disrupt synchronous rotation of planetary satellites? *J. Geophys. Res.*, **90**, 11,289–11,293.
- Liu, L., Li, S., Dai, L., Suo, Y., Liu, B., Zhang, G., Wang, Y. and Liu, E. (2012). Geometry and timing of Mesozoic deformation in the western part of the Xuefeng Tectonic Belt, South China: Implications for intra-continental deformation. *J. Asian Earth Sci.*, **49**, 330–338.
- Lopez, V., Ruiz, J. and Vázquez, A. (2015). Evidence for two stages of compressive deformation in a buried basin of Mercury. *Icarus*, **254**, 18–23.
- Lucchitta, B. K. (1976). Mare ridges and related highland scarps: Results of vertical tectonism. *Proc. Lunar Sci. Conf.*, **7**, 2761–2782.
- Mangold, N., Allemand, P. and Thomas, P. G. (1998). Wrinkle ridges of Mars: Structural analysis and evidence for shallow deformation controlled by ice-rich décollements. *Planet. Space. Sci.*, **46**, 345–356.
- Marchi, S., Massironi, M., Cremonese, G., Martellato, E., Giacomini, L. and Prockter, L. M. (2011). The effects of the target material properties and layering on the crater chronology: The case of Raditladi and Rachmaninoff basins on Mercury. *Planet. Space Sci.*, **59**, 1968–1980.
- Marchi, S., Chapman, C. R., Fassett, C. I., Head, J. W., Bottke, W. F. and Strom, R. G. (2013). Global resurfacing of Mercury 4.0–4.1 billion years ago by heavy bombardment and volcanism. *Nature*, **499**, 59–61.
- Marrett, R. and Emerman, S. H. (1992). The relations between faulting and mafic magmatism in the Altiplano-Puna plateau (central Andes). *Earth Planet. Sci. Lett.*, **112**, 53–59.
- Marti, J., Ablay, G. J., Redshaw, L. T. and Sparks, R. S. J. (1994). Experimental studies of collapse calderas. *J. Geol. Soc. London*, **151**, 919–929.
- Massironi, M., Di Achille, G., Rothery, D. A., Galluzzi, V., Giacomini, L., Ferrari, S., Zusi, M., Cremonese, G. and Palumbo P. (2015). Lateral ramps and strike-slip kinematics on Mercury. In *Volcanism and Tectonism Across the Solar System*, ed. T. Platz, M. Massironi, P. K. Byrne and H. Heisinger, Special Publication 401. London: Geological Society, pp. 269–290.
- Masursky, H., Colton, G. W. and El-Baz, F. (1978). *Apollo over the Moon: A View from Orbit*, Special Publication SP-362. Washington, DC: NASA.
- Matsuyama, I. and Nimmo, F. (2009). Gravity and tectonic patterns of Mercury: Effect of tidal deformation, spin-orbit resonance, non-zero eccentricity, despinning, and reorientation. *J. Geophys. Res.*, **114**, E01010, doi:10.1029/2008JE003252.
- Matsuyama, I., Nimmo, F. and Mitrovica, J. X. (2014). Planetary reorientation. *Annu. Rev. Earth Planet. Sci.*, **42**, 605–634.
- McAdoo, D. C. and Sandwell, D. T. (1985). Folding of oceanic lithosphere. *J. Geophys. Res.*, **90**, 8563–8569.
- McClay, K. R. (1992). *Thrust Tectonics*. London: Chapman and Hall.
- McDougall, J. W., Hussain, A. and Yeats, R. S. (1993). The Main Boundary Thrust and propagation of deformation into the foreland fold-and-thrust belt in northern Pakistan near the Indus River. In *Himalayan Tectonics*, ed. P. J. Treloar and M. P. Searle, Special Publication 74. London: Geological Society, pp. 581–588.
- McGovern, P. J. and Litherland, M. M. (2011). Lithospheric stress and basaltic magma ascent on the Moon, with implications for large volcanic provinces and edifices. *Lunar Planet. Sci.*, **42**, abstract 2587.
- Melosh, H. J. (1975). Large impact craters and the Moon's orientation. *Earth. Planet. Sci. Lett.*, **26**, 353–360.
- Melosh, H. J. (1977). Global tectonics of a despun planet. *Icarus*, **31**, 221–243.
- Melosh, H. J. (1980). Tectonic patterns on a tidally distorted planet. *Icarus*, **43**, 334–337.
- Melosh, H. J. (1984). Impact ejection, spallation, and the origin of meteorites. *Icarus*, **59**, 234–260.
- Melosh, H. J. and Dzurisin, D. (1978). Mercurian global tectonics: A consequence of tidal despinning? *Icarus*, **35**, 227–236.
- Melosh, H. J. and McKinnon, W. B., (1988). The tectonics of Mercury. In *Mercury*, ed. F. Vilas, C. R. Chapman and M. S. Matthews. Tucson, AZ: University of Arizona Press, pp. 374–400.
- Michel, N. C., Hauck, S. A., II, Solomon, S. C., Phillips, R. J., Roberts, J. H. and Zuber, M. T. (2013). Thermal evolution of Mercury as constrained by MESSENGER observations. *J. Geophys. Res. Planets*, **118**, 1033–1044.
- Montésí, L. G. J. and Zuber, M. T. (2003). Clues to the lithospheric structure of Mars from wrinkle ridge sets and localization instability. *J. Geophys. Res.*, **108**, E65048, doi:10.1029/2002JE001974.
- Moore, H. J., Boyce, J. M. and Hahn, D. A. (1980). Small impact craters in the lunar regolith: Their morphologies, relative ages, and rates of formation. *Moon Planets*, **23**, 231–252.
- Morbidielli, A., Tsiganis, K., Batygin, K., Cruda, A. and Gomes, R. (2012). Explaining why the uranian satellites have equatorial prograde orbits despite the large planetary obliquity. *Icarus*, **219**, 737–740.
- Mueller, K. and Golombok, M. (2004). Compressional structures on Mars. *Annu. Rev. Earth Planet. Sci.*, **32**, 435–464.
- Murchie, S. L., Watters, T. R., Robinson, M. S., Head, J. W., Strom, R. G., Chapman, C. R., Solomon, S. C., McClintock, W. E., Prockter, L. M., Domingue, D. L. and Blewett, D. T. (2008). Geology of the Caloris basin, Mercury: A view from MESSENGER. *Science*, **321**, 73–76.
- Murray, B. C., Belton, M. J. S., Danielson, G. E., Davies, M. E., Gault, D. E., Hapke, B., O'Leary, B., Strom, R. G., Suomi, V. and Trask, N. (1974). Mercury's surface: Preliminary description and interpretation from Mariner 10 pictures. *Science*, **185**, 169–179.
- Neil, E. A. and Houseman, G. A. (1999). Rayleigh–Taylor instability of the upper mantle and its role in intraplate orogeny. *Geophys. J. Int.*, **138**, 89–107.

- Nimmo, F. and Watters, T. R. (2004). Depth of faulting on Mercury: Implications for heat flux and crustal and effective elastic thickness. *Geophys. Res. Lett.*, **31**, L02701, doi:10.1029/2003GL018847.
- Nimmo, F. and Matsuyama, I. (2007). Reorientation of icy satellites by impact basins. *Geophys. Res. Lett.*, **34**, L19203, doi:10.1029/2007GL030798.
- Nimmo, F. and Pappalardo, R. T. (2006). Diapir-induced reorientation of Saturn's moon Enceladus. *Nature*, **441**, 614–616.
- Norris, R. J. and Cooper, A. F. (1997). Erosional control on the structural evolution of a transpressional thrust complex on the Alpine fault, New Zealand. *J. Struct. Geol.*, **19**, 1323–1342.
- Noyelles, B., Frouard, J., Makarov, V. V. and Efroimsky, M. (2014). Spin-orbit evolution of Mercury revisited. *Icarus*, **241**, 26–44.
- Oberst, J., Preusker, F., Phillips, R. J., Watters, T. R., Head, J. W., Zuber, M. T. and Solomon, S. C. (2010). The morphology of Mercury's Caloris basin as seen in MESSENGER stereo topographic models. *Icarus*, **209**, 230–238.
- Ostrach, L. R., Robinson, M. S., Whitten, J. L., Fassett, C. I., Strom, R. G., Head, J. W. and Solomon, S. C. (2015). Extent, age, and resurfacing history of the northern smooth plains on Mercury from MESSENGER observations. *Icarus*, **250**, 602–622.
- Padovan, S., Wieczorek, M. A., Margot, J.-L., Tosi, N. and Solomon, S. C. (2015). Thickness of the crust of Mercury from geoid-to-topography ratios. *Geophys. Res. Lett.*, **42**, 1029–1038.
- Passchier, C. W. and Trouw, R. A. J. (2006). *Microtectonics*. New York: Springer Verlag.
- Peale, S. J. (1988). The rotational dynamics of Mercury and the state of its core. In *Mercury*, ed. F. Vilas, C. R. Chapman and M. S. Matthews. Tucson, AZ: University of Arizona Press, pp. 461–493.
- Pechmann, J. B. and Melosh, H. J. (1979). Global fracture patterns of a despun planet: Application to Mercury. *Icarus*, **38**, 243–250.
- Peplowski, P. N., Evans, L. G., Hauck, S. A., II, McCoy, T. J., Boynton, W. V., Gillis-Davis, J. J., Ebel, D. S., Golsten, J. O., Hamara, D. K., Lawrence, D. J., McNutt, R. L., Nittler, L. R., Solomon, S. C., Rhodes, E. A., Sprague, A. L., Starr, R. D. and Stockstill-Cahill, K. R. (2011). Radioactive elements on Mercury's surface from MESSENGER: Implications for the planet's formation and evolution. *Science*, **333**, 1850–1852.
- Petterson, M. G., Neal, C. R., Mahoney, J. J., Kroenke, L. W., Saunders, A. D., Babbs, T. L., Duncan, R. A., Tolia, D. and McGrail, B. (1997). Structure and deformation of north and central Malaita, Solomon Islands: Tectonic implications for the Ontong Java Plateau–Solomon arc collision, and for the fate of oceanic plateaus. *Tectonophysics*, **283**, 1–33.
- Plescia, J. B. (1991). Wrinkle ridges in Lunae Planum Mars: Implications for shortening and strain. *Geophys. Res. Lett.*, **18**, 913–916.
- Plescia, J. B. (1993). Wrinkle ridges of Arcadia Planitia, Mars. *J. Geophys. Res.*, **98**, 15,049–15,059.
- Plescia, J. B. and Golombek, M. P. (1986). Origin of planetary wrinkle ridges based on the study of terrestrial analogs. *Geol. Soc. Amer. Bull.*, **97**, 1289–1299.
- Poblet, J. and Lisle, R. J. (2011). Kinematic evolution and structural styles of fold-and-thrust belts. In *Kinematic Evolution and Structural Styles of Fold-and-Thrust Belts*, ed. J. Poblet and R. J. Lisle, Special Publication 349. London: Geological Society, pp. 1–24.
- Pohn, H. A. and Offield, T. W. (1970). Lunar crater morphology and relative age determination of lunar geologic units. Part 1: Classification. Part 2: Applications. In *Geological Survey Research 1970*, Professional Paper 69–209. Denver, CO: U.S. Geological Survey, 35 pp.
- Preusker, F., Oberst, J., Head, J. W., Watters, T. R., Robinson, M. S., Zuber, M. T. and Solomon, S. C. (2011). Stereo topographic models of Mercury after three MESSENGER flybys. *Planet. Space Sci.*, **59**, 1910–1917.
- Prockter, L. M., Watters, T. R., Chapman, C. R., Denevi, B. W., Head, J. W., Solomon, S. C., Murchie, S. L., Barnouin, O. S., Robinson, M. S., Blewett, D. T., Gillis-Davis, J. J. and Gaskell, R. W. (2009). The curious case of Raditladi basin. *Lunar Planet. Sci.*, **40**, abstract 1758.
- Prockter, L. M., Ernst, C. M., Denevi, B. W., Chapman, C. R., Head, J. W., Fassett, C. I., Merline, W. J., Solomon, S. C., Watters, T. R., Strom, R. G., Cremonese, G., Marchi, S. and Massironi, M. (2010). Evidence for young volcanism on Mercury from the third MESSENGER flyby. *Science*, **329**, 668–671.
- Prockter, L. M., Baker, D. M. H., Head, J. W., Murchie, S. L., Ernst, C. M., Chapman, C. R., Denevi, B. W., Solomon, S. C., Watters, T. R. and Massironi, M. (2011). The geology of medium-sized impact basins on Mercury. *Abstracts with Programs*, **43**, paper 142–11. Boulder, CO: Geological Society of America.
- Ritter, J. A., Hauck, S. A., II and Barnouin, O. S. (2010). Mechanical structure of Mercury's lithosphere from MESSENGER observations of lobate scarps. *Lunar Planet. Sci.*, **41**, abstract 2122.
- Roberts, J. H. and Barnouin, O. S. (2012). The effect of the Caloris impact on the mantle dynamics and volcanism of Mercury. *J. Geophys. Res.*, **117**, E02007.
- Roberts, J. H. and Nimmo, F. (2008). Near-surface heating on Enceladus and the south polar thermal anomaly. *Geophys. Res. Lett.*, **35**, L09201, doi:10.1029/2011JE003876.
- Roeder, D. (1988). Andean-age structure of Eastern Cordillera (Province of La Paz, Bolivia). *Tectonics*, **7**, 23–39.
- Roeder, D. (2009). *American and Tethyan Fold-Thrust Belts*. Berlin: Gebrüder Borntraeger, 168 pp.
- Rothery, D. A. and Massironi, M. (2010). Beagle Rupes: Evidence for a basal decollement of regional extent in Mercury's lithosphere. *Icarus*, **209**, 256–261.
- Scholz, C. H. and Cowie, P. A. (1990). Determination of total strain from faulting using slip measurements. *Nature*, **346**, 837–839.
- Schubert, G., Ross, M. N., Stevenson, D. J. and Spohn, T. (1988). Mercury's thermal history and the generation of its magnetic field. In *Mercury*, ed. F. Vilas, C. R. Chapman and M. S. Matthews. Tucson, AZ: University of Arizona Press, pp. 429–460.
- Schlitz, R. A. (1985). Assessment of global and regional tectonic models for faulting in the ancient terrains of Mars. *J. Geophys. Res.*, **90**, 7849–7860.
- Schlitz, R. A. (1993). Brittle strength of basaltic rock masses with applications to Venus. *J. Geophys. Res.*, **98**, 10,883–10,895.
- Schlitz, R. A. (1995). Limits on strength and deformation properties of jointed basaltic rock masses. *Rock. Mech. Rock. Eng.*, **28**, 1–15.
- Schlitz, R. A. (1996). Relative scale and the strength and deformability of rock masses. *J. Struct. Geol.*, **18**, 1139–1149.
- Schlitz, R. A. (2000). Localization of bedding plane slip and backthrust faults above blind thrust faults: Keys to wrinkle ridge structure. *J. Geophys. Res.*, **105**, 12,035–12,052.
- Schlitz, R. A. and Fossen, H. (2008). Terminology for structural discontinuities. *Amer. Assoc. Petrol. Geol. Bull.*, **92**, 853–867.
- Schlitz, R. A. and Tanaka, K. L. (1994). Lithospheric-scale buckling and thrust structures on Mars: The Coprates rise and south Tharsis ridge belt. *J. Geophys. Res.*, **99**, 8371–8385.
- Segall, P. (1984). Formation and growth of extensional fracture sets, *Geol. Soc. Amer. Bull.*, **95**, 454–462.
- Sengör, A. M. C. and Saking, M. (2001). Structural rocks: Stratigraphic implications. In *Paradoxes in Geology*, ed. U. Briegel and W. J. Xiao. Amsterdam: Elsevier.
- Sengör, A. M. C., Natal'in, B. A. and Burtman, V. S. (1993). Evolution of the Altai tectonic collage and Palaeozoic crustal growth in Eurasia. *Nature*, **364**, 299–307.

- Smith, D. E., Zuber, M. T., Phillips, R. J., Solomon, S. C., Hauck, S. A., Lemoine, F. G., Mazarico, E., Neumann, G. A., Peale, S. J., Margot, J. L., Johnson, C. L., Torrence, M. H., Perry, M. E., Rowlands, D. D., Goossens, S., Head, J. W. and Taylor, A. H. (2012). Gravity field and internal structure of Mercury from MESSENGER. *Science*, **336**, 214–217.
- Solomatov, V. S. and Moresi, L. N. (2000). Scaling of time-dependent stagnant lid convection: Application to small-scale convection on Earth and other terrestrial planets. *J. Geophys. Res.*, **105**, 21,795–21,817.
- Solomon, S. C. (1977). The relationship between crustal tectonics and internal evolution in the Moon and Mercury. *Phys. Earth Planet. Inter.*, **15**, 135–145.
- Solomon, S. C. (1978). On volcanism and thermal tectonics on one-plate planets. *Geophys. Res. Lett.*, **5**, 461–464.
- Solomon, S. C. and Chaiken, J. (1976). Thermal expansion and thermal stress in the Moon and terrestrial planets: Clues to early thermal history. *Proc. Lunar Sci. Conf.*, **7**, 3229–3243.
- Solomon, S. C., McNutt, R. L., Jr., Watters, T. R., Lawrence, D. J., Feldman, W. C., Head, J. W., Krimigis, S. M., Murchie, S. L., Phillips, R. J., Slavin, J. A. and Zuber, M. T. (2008). Return to Mercury: A global perspective on MESSENGER's first Mercury flyby. *Science*, **321**, 59–62.
- Solomon, S. C., Klimczak, C., Byrne, P. K., Hauck, S. A., II, Balcerski, J. A., Dombard, A. J., Zuber, M. T., Smith, D. E., Phillips, R. J., Head, J. W. and Watters, T. R. (2012). Long-wavelength topographic change on Mercury: Evidence and mechanisms. *Lunar Planet. Sci.*, **43**, abstract 1578.
- Spudis, P. D. and Guest, J. E. (1988). Stratigraphy and geologic history of Mercury. In *Mercury*, ed. F. Vilas, C. R. Chapman and M. S. Matthews. Tucson, AZ: University of Arizona Press, pp. 118–164.
- Stille, H. (1920). Über Alter und Art der Phasen variszischer Gebirgsbildung. *Nachr. Ges. Wiss. Göttingen*, 1–7.
- Stille, H. (1940). Einführung in den Bau Amerikas. In *Einführung in den Bau Amerikas*. Berlin: Gebrüder Borntraeger.
- Strom, R. G., Trask, N. J. and Guest, J. E. (1975). Tectonism and volcanism on Mercury. *J. Geophys. Res.*, **80**, 2478–2507.
- Strom, R. G., Chapman, C. R., Merline, W. J., Solomon, S. C. and Head, J. W. (2008). Mercury cratering record viewed from MESSENGER's first flyby. *Science*, **321**, 79–81.
- Strom, R. G., Banks, M. E., Chapman, C. R., Fassett, C. I., Forde, J. A., Head, J. W., Merline, W. J., Prockter, L. M. and Solomon, S. C. (2011). Mercury crater statistics from MESSENGER flybys: Implications for stratigraphy and resurfacing history. *Planet. Space Sci.*, **59**, 1960–1967.
- Suess, E. (1883). In *Das Antlitz der Erde*, Vol. I, ed. E. Suess. Leipzig: F. Tempsky.
- Suess, E. (1909). In *Das Antlitz der Erde*, Vol. III.2, ed. E. Suess. Leipzig: F. Tempsky.
- Thomas, P. G., Masson, P. and Fleitout, L. (1988). Tectonic history of Mercury. In *Mercury*, ed. F. Vilas, C. R. Chapman and M. S. Matthews. Tucson, AZ: University of Arizona Press, pp. 401–428.
- Thomas, R. J., Rothery, D. A., Conway, S. J. and Anand, M. (2014). Long-lived explosive volcanism on Mercury. *Geophys. Res. Lett.*, **41**, 6084–6092.
- Toksöz, M. N., Dainty, A. M., Solomon, S. C. and Anderson, K. R. (1974). Structure of the Moon. *Rev. Geophys. Space Phys.*, **12**, 539–567.
- Tosi, N., Grott, M., Plesa, A. C. and Breuer, D. (2013). Thermochemical evolution of Mercury's interior. *J. Geophys. Res. Planets*, **118**, 2474–2487.
- Tosi, N., Čadek, O., Běhouková, M., Káňová, M., Plesa, A. C., Grott, M., Breuer, D., Padovan, S. and Wieczorek, M. A. (2015). Mercury's low-degree geoid and topography controlled by insolation-driven elastic deformation. *Geophys. Res. Lett.*, **42**, 7327–7335.
- Trask, N. J. (1971). Geologic comparison of mare materials in the lunar equatorial belt, including Apollo 11 and Apollo 12 landing sites. In *Geophysical Survey Research 1971*, Professional Paper 750-D. Denver, CO: U.S. Geological Survey, pp. 138–144.
- Trask, N. J. (1975). Cratering history of the heavily cratered terrain on Mercury. *Proc. Int. Colloq. Planet. Geol., Geol. Rom.*, **15**, 471–476.
- Trask, N. J. and Guest, J. E. (1975). Preliminary geologic terrain map of Mercury. *J. Geophys. Res.*, **80**, 2461–2477.
- Trümpp, R. (1980). *Geology of Switzerland, A Guide-book: An Outline of the Geology of Switzerland*, ed. R. Trümpp. Bern: Schweizerische Geologische Kommission, 334 pp.
- Turcotte, D. L. (1983). Thermal stresses in planetary elastic lithospheres. *J. Geophys. Res.*, **88**, A585–A587.
- Tweto, O. (1975). Laramide (Late Cretaceous–Early Tertiary) Orogeny in the Southern Rocky Mountains. In *Cenozoic History of the Southern Rocky Mountains*, ed. B. F. Curtis. Memoirs, Vol. 144. Boulder, CO: Geological Society of America, pp. 1–44.
- Vasavada, A. R., Paige, D. A. and Wood, S. E. (1999). Near-surface temperatures on Mercury and the Moon and the stability of polar ice deposits. *Icarus*, **141**, 179–193.
- Walsh, J. B. (1965). The effect of cracks on the uniaxial compression of rocks. *J. Geophys. Res.*, **70**, 399–411.
- Walter, T. R. and Troll, V. R. (2001). Formation of caldera periphery faults: An experimental study. *Bull. Volcanol.*, **63**, 191–203.
- Watanabe, T., Koyaguchi, T. and Seno, T. (1999). Tectonic stress controls on ascent and emplacement of magmas. *J. Volcanol. Geotherm. Res.*, **91**, 65–78.
- Watters, T. R. (1991). Origin of periodically spaced wrinkle ridges on the Tharsis Plateau of Mars. *J. Geophys. Res.*, **96**, 15,599–15,616.
- Watters, T. R. (2004). Elastic dislocation modeling of wrinkle ridges on Mars. *Icarus*, **171**, 284–294.
- Watters, T. R. and Nimmo, F. (2010). The tectonics of Mercury. In *Planetary Tectonics*, ed. T. R. Watters and R. A. Schultz. New York: Cambridge University Press, pp. 15–80.
- Watters, T. R., Robinson, M. S. and Cook, A. C. (1998). Topography of lobate scarps on Mercury: New constraints on the planet's contraction. *Geology*, **26**, 991–994.
- Watters, T. R., Cook, A. C. and Robinson, M. S. (2001). Large-scale lobate scarps in the southern hemisphere of Mercury. *Planet. Space Sci.*, **49**, 1523–1530.
- Watters, T. R., Schultz, R. A., Robinson, M. S. and Cook, A. C. (2002). The mechanical and thermal structure of Mercury's early lithosphere. *Geophys. Res. Lett.*, **29**, 1542, doi:10.1029/2001GL014308.
- Watters, T. R., Robinson, M. S., Bina, C. R. and Spudis, P. D. (2004). Thrust faults and the global contraction of Mercury. *Geophys. Res. Lett.*, **31**, L04701, doi:10.1029/2003GL019171.
- Watters, T. R., Nimmo, F. and Robinson, M. S. (2005). Extensional troughs in the Caloris basin of Mercury: Evidence of lateral crustal flow. *Geology*, **33**, 669–672.
- Watters, T. R., Solomon, S. C., Robinson, M. S., Head, J. W., André, S. L., Hauck, S. A., II and Murchie, S. L. (2009a). The tectonics of Mercury: The view after MESSENGER's first flyby. *Earth Planet. Sci. Lett.*, **285**, 283–296.
- Watters, T. R., Head, J. W., Solomon, S. C., Robinson, M. S., Chapman, C. R., Denevi, B. W., Fassett, C. I., Murchie, S. L. and Strom, R. G. (2009b). Evolution of the Rembrandt impact basin on Mercury. *Science*, **324**, 618–621.
- Watters, T. R., Murchie, S. L., Robinson, M. S., Solomon, S. C., Denevi, B. W., André, S. L. and Head, J. W. (2009c).

- Emplacement and tectonic deformation of smooth plains in the Caloris basin, Mercury. *Earth Planet. Sci. Lett.*, **285**, 309–319.
- Watters, T. R., Solomon, S. C., Klimczak, C., Freed, A. M., Head, J. W., Ernst, C. M., Blair, D. M., Goudge, T. A. and Byrne, P. K. (2012). Extension and contraction within volcanically buried impact craters and basins on Mercury. *Geology*, **40**, 1123–1126.
- Watters, T. R., Selvans, M. M., Banks, M. E., Hauck, S. A., II, Becker, K. J. and Robinson, M. S. (2015). Distribution of large-scale contractional tectonic landforms on Mercury: Implications for the origin of global stresses. *Geophys. Res. Lett.*, **42**, 3755–3763.
- Watters, T. R., Daud, K., Banks, M. E., Selvans, M. M., Chapman, C. R. and Ernst, C. M. (2016). Recent tectonic activity on Mercury revealed by small thrust fault scarps. *Nature Geosci.*, **9**, 743–747.
- Weider, S. Z., Nittler, L. R., Starr, R. D., McCoy, T. J., Stockstill-Cahill, K. R., Byrne, P. K., Denevi, B. W., Head, J. W. and Solomon, S. C. (2012). Chemical heterogeneity on Mercury's surface revealed by the MESSENGER X-Ray Spectrometer. *J. Geophys. Res.*, **117**, E00L05.
- Whitten, J. L., Head, J. W., Denevi, B. W. and Solomon, S. C. (2014). Intercrater plains on Mercury: Insights into unit definition, characterization, and origin from MESSENGER datasets. *Icarus*, **241**, 97–113.
- Wickham, J. (1995). Fault displacement-gradient folds and the structure at Lost Hills, California (U.S.A.). *J. Struct. Geol.*, **17**, 1293–1302.
- Wieczorek, M. A. and Le Feuvre, M. (2009). Did a large impact reorient the Moon? *Icarus*, **200**, 358–366.
- Wieczorek, M. A. and Zuber, M. T. (2001). A Serenitatis origin for the Imbrium grooves and South Pole–Aitken thorium anomaly. *J. Geophys. Res.*, **106**, 27,856–27,864.
- Wieczorek, M. A., Correia, A. C. M., Le Feuvre, M., Laskar, J. and Rambaux, N. (2012). Mercury's spin–orbit resonance explained by initial retrograde and subsequent synchronous rotation. *Nature Geosci.*, **5**, 18–21.
- Wieczorek, M. A., Neumann, G. A., Nimmo, F., Kiefer, W. S., Taylor, G. J., Melosh, H. J., Phillips, R. J., Solomon, S. C., Andrews-Hanna, J. C., Asmar, S. W., Konopliv, A. S., Lemoine, F. G., Smith, D. E., Watkins, M. M., Williams, J. G. and Zuber, M. T. (2013). The crust of the Moon as seen by GRAIL. *Science*, **339**, 671–675.
- Williams, J.-P., Ruiz, J., Rosenburg, M. A., Aharonson, O. and Phillips, R. J. (2011). Insolation driven variations of Mercury's lithospheric strength. *J. Geophys. Res.*, **116**, E01008, doi:10.1029/2010JE003655.
- Wilson, J. T. (1954). The development and structure of the crust. In *The Earth as a Planet: The Solar System II*, ed. G. P. Kuiper. Chicago, IL: University of Chicago Press, pp. 138–214.
- Woodcock, N. H. and Soper, N. J. (2006). The Acadian Orogeny: The mid-Devonian phase of deformation that formed slate belts in England and Wales. In *The Geology of England and Wales*, ed. P. J. Brenchley and P. F. Rawson. London: Geological Society, pp. 131–146.
- Xia, K. and Ahrens, T. J. (2001). Impact induced damage beneath craters. *Geophys. Res. Lett.*, **28**, 3525–3527.
- Zhong, S. (2009). Migration of Tharsis volcanism on Mars caused by differential rotation of the lithosphere. *Nature Geosci.*, **2**, 19–23.
- Zuber, M. T. (1995). Wrinkle ridges, reverse faulting, and the depth penetration of lithospheric strain in Lunae Planum, Mars. *Icarus*, **114**, 80–92.
- Zuber, M. T. and Mouginis-Mark, P. J. (1992). Caldera subsidence and magma chamber depth of the Olympus Mons volcano, Mars. *J. Geophys. Res.*, **97**, 18,295–18,307.
- Zuber, M. T. and Smith, D. E. (1997). Mars without Tharsis. *J. Geophys. Res.*, **102**, 28,673–28,685.
- Zuber, M. T., Montésí, L. G. J., Farmer, G. T., Hauck, S. A., II, Ritter, J. A., Phillips, R. J., Solomon, S. C., Smith, D. E., Talpe, M. J., Head, J. W., III, Neumann, G. A., Watters, T. R. and Johnson, C. L. (2010). Accommodation of lithospheric shortening on Mercury from altimetric profiles of ridges and lobate scarps measured during MESSENGER flybys 1 and 2. *Icarus*, **209**, 247–255.
- Zuber, M. T., Smith, D. E., Phillips, R. J., Solomon, S. C., Neumann, G. A., Hauck, S. A., II, Peale, S. J., Barnouin, O. S., Head, J. W., Johnson, C. L., Lemoine, F. G., Mazarico, E., Sun, X., Torrence, M. H., Freed, A. M., Margot, J. L., Oberst, J., Perry, M. E., McNutt, R. L., Jr., Balcerski, J. A., Michel, N., Talpe, M. J. and Yang, D. (2012). Topography of the northern hemisphere of Mercury from MESSENGER laser altimetry. *Science*, **336**, 217–220.